Development of a beam position monitor based on Cherenkov diffraction radiation for the AWAKE experiment at CERN

Collette Pakuza

Oriel College

University of Oxford

A thesis presented for the degree of

Doctor of Philosophy

Trinity Term 2023

Abstract

The Plasma Wakefield Experiment (AWAKE) at CERN utilises $400\,\mathrm{GeV}$ proton bunches from the Super Proton Synchrotron (SPS) to generate plasma wakefields in a $10\,\mathrm{m}$-long rubidium vapour cell for high-gradient acceleration of $16\,\mathrm{MeV}$ electron bunches. The proton and electron bunches propagate closely in time and space within the common beam-line before the entrance of the plasma cell. The proton bunches possess a bunch charge of $48\,\mathrm{nC}$ and a RMS bunch length of $200 - 400\,\mathrm{ps}$, while the electron bunches carry a much lower bunch charge of $\sim 600\,\mathrm{pC}$ and have a few ps bunch length. The independent position monitoring of both beam bunches is mission critical to ensure a perfect overlap of their trajectories in the plasma cell. Unfortunately, the current electron beam position monitoring (BPM) system operates at $404\,\mathrm{MHz}$, in a spectral region where the electron signal is completely overshadowed by the proton signal. In order to exclusively measure the electron bunches in the presence of the more-intense proton bunches, a BPM operating at a sufficiently high frequency is required, still within the electron bunch spectrum, but well outside the proton bunch spectrum.

The work detailed in this thesis on the development of a novel type of BPM based on Cherenkov diffraction radiation (ChDR) aims at addressing this problem. ChDR is generated by the surface of a dielectric medium, commonly referred to as a radiator, when a charged particle passes in close proximity under the Cherenkov condition. The thesis provides an overview of the currently employed analytical model describing ChDR, comparing it with numerical simulations. It presents the design process of the ChDR BPM for AWAKE, aided by numerical simulations. Furthermore, it details the design and execution of an RF test-bench characterisation of the ChDR radiator for AWAKE, aiming to bridge the gap between numerical simulations and experimental beam tests.

Finally, the thesis reports on the systematic beam studies of the physical ChDR BPM devices, performed at AWAKE and at the CERN Linear Electron Accelerator for Research (CLEAR) test facility, involving both proton and electron beams.

I dedicate this thesis to my parents.

Acknowledgements

First and foremost, I would like to express my deepest gratitude to my university supervisor, Prof. Philip Burrows for his commitment, exceptional mentorship and encouragement throughout my DPhil with the John Adams Institute. I am extremely fortunate to have had the privilege to work under his supervision and at one of the most renowned institutes in the world.

I am equally grateful to my CERN supervisor, Dr. Stefano Mazzoni, for all of his help, patience, and support during my time at CERN, and for his positive outlook on research which I strongly admire.

I would also like to express my heartfelt appreciation to my CERN co-supervisor, Mr. Manfred Wendt, who has played a significant role in my academic journey, for guiding and supporting me all the way through my DPhil. He went above and beyond, dedicating a lot of his time and effort to help me navigate challenging aspects of my research. I have learnt a great deal from him, not only on the technical subjects of RF engineering and beam position monitors, but also professionally.

In addition, I would like to thank Dr. Thibaut Lefèvre for sharing his expertise and insights on the subject matter, and for bringing together the research group to study and develop technology based on Cherenkov diffraction radiation.

Furthermore, I extend my gratitude to my colleagues and peers from the John Adams Institute, the Beam Instrumentation group at CERN, the CLEAR test facility and the AWAKE experiment, for making it such a warm and welcoming environment for me to conduct my research, and for sharing their technical and professional experiences with me.

Last but not least, I would like to express my deepest appreciation to my parents, family and friends for their continued love, encouragement, and support. I could not have done it without them.

Contents

List of Figures

List of Tables

List of Abbreviations

ATLAS	A Toroidal LHC Apparatus
AWAKE	Advanced Proton Driven Plasma Wakefield Experiment
BPM	Beam Position Monitor
BPF	Band-Pass Filter
BTV	Beam Television
BW	Bandwidth
CCD	Charge-Coupled Device
CERN	European Organisation for Nuclear Research
ChDR	Cherenkov Diffraction Radiation
ChR	Cherenkov Radiation
CLEAR	CERN Linear Electron Acceleration for Research
CLIC	Compact Linear Collider
CM	Centre-of-Mass
CMS	Compact Muon Solenoid
CPA	Chirped-Pulse Amplification
CST	Computer Simulation Technology
CTF3	CERN Compact Linear Collider Test Facility

CTR	Coherent Transition Radiation
CW	Continuous Wave
SM	Standard Model
DC	Direct Current
DR	Diffraction Radiation
EM	Electromagnetic
FCC	Future Circular Collider
FD	Frequency-Domain
HEP	High-Energy Physics
HL-LHC	High Luminosity LHC
HOM	Higher Order Mode
ICT	Integrated Current Transformer
iFFT	Inverse Fast Fourier Transform
ILC	International Linear Collider
IP	Interaction Point
LHC	Large Hadron Collider
LWFA	Laser Wakefield Acceleration
MME	Mechanical and Materials Engineering
OTR	Optical Transition Radiation
PCA	Polarisatoin Current Approach
PEC	Perfect Electrical Conductor

PHIN	Photo-Injector
PIC	Particle-in-Cell
PR	Polarisation Radiation
PU	Pick-Up
PWFA	Plasma Wakefield Acceleration
Qucs	Quite Universal Circuit Simulation
RF	Radio Frequency
RFD	RF Deflector
SC	Super-Conducting
SMI	Self-Modulation Instability
SMM	Seeded Self-Modulation
SPR	Smith-Purcell radiation
SPS	Super Proton Synchrotron
TD	Time-Domain
TDR	Time-Domain Reflectometry
TEM	Transverse Electromagnetic
TR	Transition Radiation
VNA	Vector Network Analyser
WG	Waveguide

1 Introduction

1.1 The Standard Model

The Standard Model (SM) of Particle Physics [1] is a successful theory in describing the properties of the fundamental constituents of matter and their interactions. This model is tested and verified with observations and measurements carried out in accelerator-based high-energy physics (HEP) experiments.

The fundamental particles can be organised into two types. These are two half-integer spin families of fermions called quarks and leptons (Table 1.1). Quarks have a charge of + 2/3 e or -1/3 e, where e is the unit of elementary charge, and leptons have a charge of -1 e for charged leptons and 0 e for neutrinos. These are further grouped into three generations with increasing mass.

Table 1.1: Particles that make up the family of fermions in the SM.

Generation	I	II	III
Quarks	Up Down	Charm Strange	Top Bottom
Leptons	Electron Electron neutrino	Muon Muon neutrino	Tau Tau neutrino

The particles that mediate the fundamental forces that govern interactions between particles are spin-1 bosons known as gauge bosons (Table 1.2). These are: the photon (γ), a massless particle that mediates the electromagnetic force which, for example, confines nuclei and electrons to form atoms; the gluon (g), also a

Table 1.2: Bosons and the interactions they mediate.

Boson	Interaction mediated
Photon	Electromagnetism
$W^{\pm}$ and Z^0	Weak interaction
Gluon	Strong interaction

massless particle that mediates the strong force which binds quarks into hadrons; and the $W^{\pm}$ and Z^0 bosons that mediate the weak force which is, for example, responsible for the radioactive decay of atoms.

Finally, there is a fundamental particle described by the SM which has a spin of zero. This is called the Higgs boson [2] produced by the quantum excitation of the Higgs field which gives mass to the particles of the SM. The Higgs boson was discovered in 2012 at the Large Hadron Collider (LHC) [3] at the European Organization for Nuclear Research (CERN), located in Geneva, Switzerland by both the Compact Muon Solenoid (CMS) and A Toroidal LHC Apparatus (ATLAS) detectors [4], [5].

1.2 Particle accelerators

Accelerators are primarily composed of a particle source, an arrangement of magnets and accelerating structures [6]. Different types of particle accelerators exist. For HEP purposes, synchrotron storage rings and linear accelerators are popular, but as the desired beam energy cannot be achieved with a single accelerator, typically a chain of several particle accelerators is needed to reach the required beam properties.

The process of particle beam production in the source depends on the type of particles required. Hadrons i.e. protons or ions can be generated using glow discharge columns, and electrons can be produced via a heated cathode, also called a thermionic gun, and are initially accelerated in a high DC electric field. Electrons can be more efficiently generated by aiming a short laser pulse onto a photocathode, housed in a radio frequency resonator (RF cavity) for initial acceleration.

For particle beam guidance, accelerators use bending magnets, called dipoles. Dipoles are used to produce magnetic fields that are perpendicular to the direction of particle motion. An example of a dipole magnet is shown in Fig. 1.1 where the magnetic fields are indicated by the black and pink dotted lines. The particle deflection inside these magnets is governed by

$$\frac{\gamma_r m v^2}{\rho} = qvB, \tag{1.1}$$

where γ_r is the relativistic Lorentz factor, m is the particle mass, v is the particle velocity, ρ is the bending radius, q is the particle charge and B is the magnetic field strength. A term called the beam rigidity [8] which is a measure of the momentum

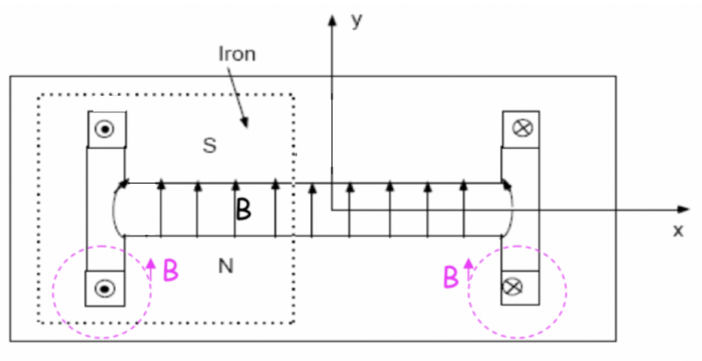

Figure 1.1: Schematic of a dipole magnet used for particle bending. The magnetic fields are indicated by the black and pink dotted lines. The direction of the current in the current-carrying coils that surround the iron is shown by the black circular dots and crosses. The x and y axes represent the transverse plane where the particle beam motion would be perpendicular to this plane [7].

p of a charged particle can be derived from the previous expression to be

$$B\rho = \frac{p}{q}. \tag{1.2}$$

Higher order magnets such as quadrupoles are used to focus the beam. These consist of poles of alternating magnetisation where the magnetic field at the centre is zero and only particles that diverge from the centre feel a force. An example of a quadrupole magnet is shown in Fig. 1.2. Whilst each quadrupole only focuses in either the vertical or horizontal transverse direction, a combination of quadrupoles can be used to perform focusing in both planes.

The acceleration of charged particles can be achieved via resonant structures, RF cavities, where oscillating electromagnetic fields are excited by an external, high-power RF source. This produces a strong electric field in the longitudinal

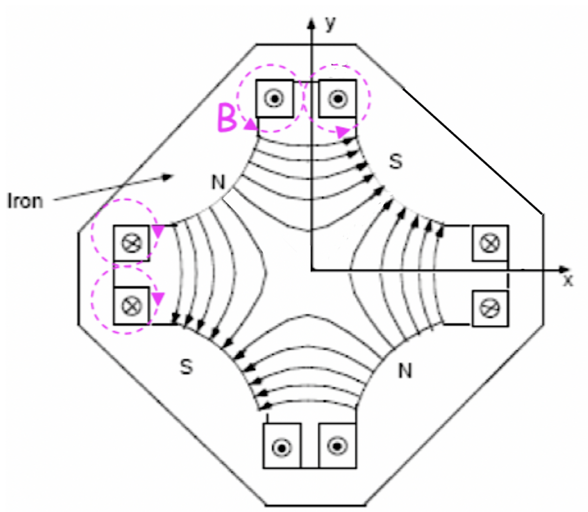

Figure 1.2: Schematic of a quadrupole magnet used for particle beam focusing. The magnetic fields are indicated by the black and pink dotted lines. The direction of the current in the current-carrying coils that surround the iron is shown by the black circular dots and crosses. The x and y axes represent the transverse plane where the particle beam motion would be perpendicular to this plane [7].

direction. The particles must arrive at specific times in order to be accelerated in the time-varying field of the RF resonators. In circular accelerators, the particle beams are stored for long times and perform multiple turns gaining energy each time they pass the RF cavities. As the particle energy increases, the beam rigidity increases. In order to keep the particles at a constant radius, the field strength of the dipole magnets must increase in synchronism. This type of circular accelerator is called a synchrotron. In contrast, linear accelerators direct particles on a linear, single pass, accelerated via a sequence of standing or travelling-wave accelerating structures.

1.3 Particle colliders

Particle colliders are an arrangement of particle accelerators used to accelerate beams of subatomic particles to high energies, used for head-on collisions between counter-propagating beams to probe the fundamental building blocks of the universe in large-scale HEP experiments.

The capability of an accelerator to produce the necessary number of interactions is measured by the luminosity $\mathcal{L}$ which has units of inverse picobarns per second $\mathrm{pb}^{-1}\mathrm{s}^{-1}$, where $1\,\mathrm{pb} = 10^{-36}\mathrm{cm}^2$. This relates the rate of an event of a specific type R occurring to its production cross-section σ_p at a given centre-of-mass (CM) energy E_{CM} shown by

$$R = \mathcal{L}\sigma_p(E_{CM}). \tag{1.3}$$

The cross-section is the probability of the event of interest occurring in units of pb. The luminosity depends on the particle beam properties. For colliders, the luminosity is defined by

$$\mathcal{L} = \frac{1}{4\pi}\frac{N_1 N_2 f n_b}{\sigma_x \sigma_y}\mathcal{F}, \tag{1.4}$$

where N_1 and N_2 are the number of particles of the head-on colliding bunches, f is the collision frequency, n_b is the number of colliding bunches per cycle, σ_x and σ_y are the transverse bunch sizes in the horizontal and vertical axes respectively, and $\mathcal{F}$ is a geometric factor that includes various effects such as crossing angle, collision offset and the hourglass effect [9].

In circular colliders, the fraction of the counter-rotating particle beams that don't collide can continue to circulate and be used in future collisions. Whereas in linear colliders, the remaining particles are dumped. The repetition frequency of linear colliders is usually lower compared to the revolution frequency of a circular collider. Therefore, linear colliders must focus the beams at the interaction point (IP) to much smaller sizes to reach similar luminosities.

The goal of increasing the CM energy and luminosity presents a number of technical challenges. Existing accelerators implement a range of sophisticated accelerator technologies in order to maximise these two figures of merit. As the need for higher CM energies and luminosities increases, there will be more challenges that will need to be addressed. The following summarises the accelerators that are at the forefront of modern-day particle physics studies and the limitations for future colliders.

- **Circular hadron colliders:** The maximum energy reach of a circular hadron collider is restricted by the strength of the bending magnets, which defines the circumference of the ring. As shown in Equation 1.2, the higher the energy, the larger the bending radius is for a given dipole field strength. This provides technical and economic limitations on the maximum energy that can be achieved in a circular hadron collider. The largest existing circular hadron collider is the LHC at CERN. This is a $27\,\mathrm{km}$ circumference proton-proton collider with a CM energy of around $13.6\,\mathrm{TeV}$. The LHC uses superconducting (SC) dipoles that generate magnetic field strengths up to $8.33\,\mathrm{T}$. The LHC has a luminosity of $(1-2)\times 10^{34}\ \mathrm{cm}^{-2}\mathrm{s}^{-1}$. Major upgrades of the machine are foreseen to prepare the collider for the High Luminosity LHC (HL-LHC) project [10] which is expected to operate from 2029. This will include the upgrade of the focusing magnets that surround the ATLAS and CMS experiments from their current strength of $8\,\mathrm{T}$ to $12\,\mathrm{T}$. The luminosity of HL-LHC is expected to be 5 times higher than the LHC nominal value. The proposed $\sim\ 100\,\mathrm{km}$ Future Circular Collider (FCC) [11] (see Fig. 1.3), which would expand the research currently being carried out at the LHC, will use $16\,\mathrm{T}$ SC dipole magnets and could offer proton

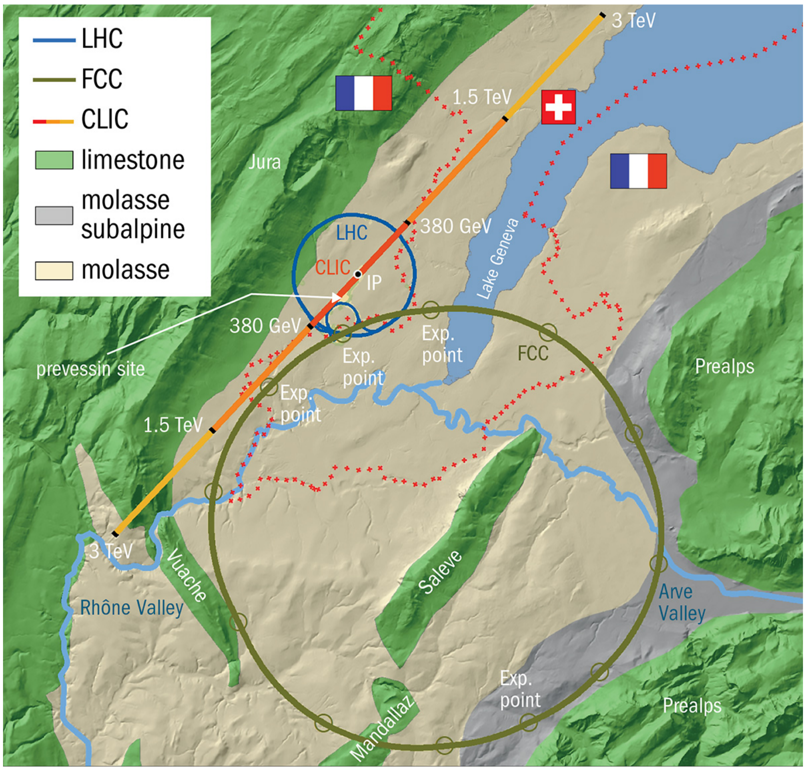

Figure 1.3: The footprint of the proposed FCC project and CLIC [12].

collisions with CM energies up to $100\,\mathrm{TeV}$ [13].

- **Circular lepton colliders:** The maximum achievable collision energy of circular lepton colliders is also restricted by the parameters expressed in Equation 1.2. However, the energy loss due to the emission of synchrotron radiation as the particles are directed on a circular trajectory also plays a significant role in circular lepton colliders. Since leptons are much lighter than hadrons, and the instantaneous synchrotron radiation power is given by [6]

$$P \propto \frac{1}{\rho^2}\frac{E^4}{m_0^4}, \tag{1.5}$$

where E is the particle energy and m_0 is the particle rest mass, leptons lose much more energy in the form of synchrotron radiation than hadrons for a given energy and radius. For electrons with the same energy and radius, the energy loss due to the emission of synchrotron radiation is $\sim 10^{13}$ more than it is for protons. Therefore, this poses a further limitation on the energy reach of a circular lepton collider.

- **Linear lepton colliders:** By design, linear lepton colliders avoid significant energy loss due to synchrotron radiation. For linear colliders, the energy reach is determined by

$$p \propto LG_{acc}, \tag{1.6}$$

where p is the particle momentum, L is the acceleration length and G_{acc} is the accelerating gradient. Therefore, in order to reach higher particle energies, the accelerating gradient needs to be maximized, whilst the length, and, therefore, the cost of the collider, needs to be kept reasonable. Two designs for large-scale linear electron-positron colliders exist. These are the normal-conducting Compact Linear Collider (CLIC) [14], [15], [16] (see Fig. 1.4) and the SC International Linear Collider (ILC) [17] (see Fig. 1.5).

Both colliders comprise three stages with increasing collision energy. The CM energy and footprint of the stages for both colliders are summarised in Table 1.3. CLIC involves a two-beam acceleration scheme and ILC would use $1.3\,\mathrm{GHz}$ SC RF cavities with $31.5\,\mathrm{MV/m}$ gradient [18]. The main limitation, besides the practicality and cost of building ever-expanding accelerators, is the surface electrical breakdown of conventional metallic accelerating structures [19]. To overcome these limitations, novel acceleration technologies are being developed involving plasmas.

Table 1.3: The CM energy and footprint of the CLIC and ILC.

Collider	Stage	CM energy	Footprint
CLIC	1	380 GeV	11.4 km
	2	1.5 TeV	29.0 km
	3	3 TeV	50.1 km
ILC	1	250 GeV	20.5 km
	2	500 GeV	31 km
	3	1 TeV	50 km

1.4 Plasma wakefield acceleration

A plasma is an electrically neutral group of ions and free electrons that experience collective effects. They can generate large electric fields where the maximum sustainable field is defined by the wave-breaking field [22]

$$E_{wb} = \frac{m_e c \omega_p}{e} = 96\sqrt{n_e[cm^{-3}]}(V/m), \tag{1.7}$$

where $\omega_p = \sqrt{e^2 n_e/\epsilon_0 m_e}$ is the plasma electron frequency, n_e is the plasma electron density, m_e is the electron mass, c is the speed of light and ϵ_0 is the permittivity of free space. The wave-breaking field can reach up to $100\,\mathrm{GV/m}$ for

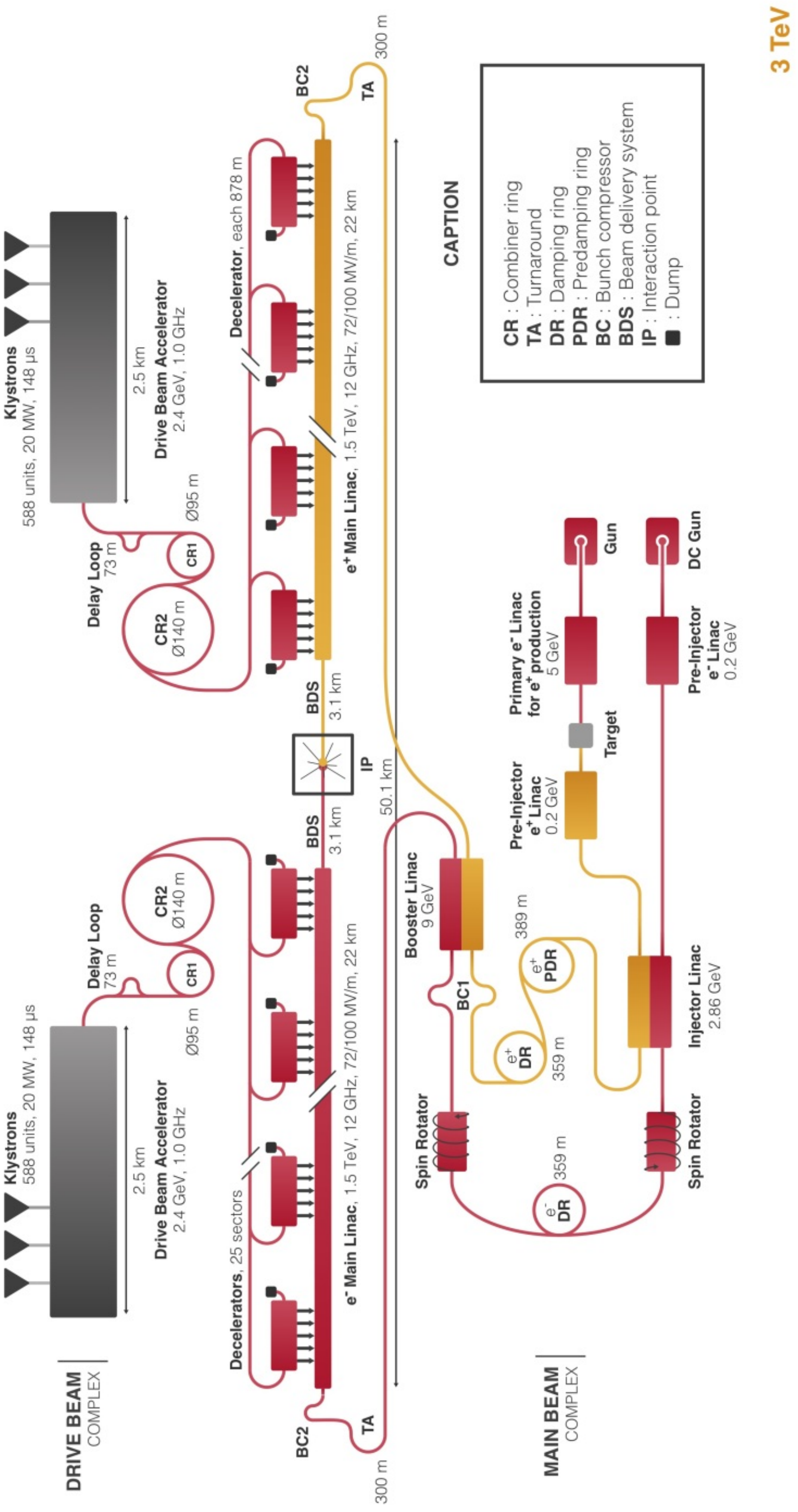

Figure 1.4: Schematic of the proposed design of CLIC at 3 TeV CM energy [20].

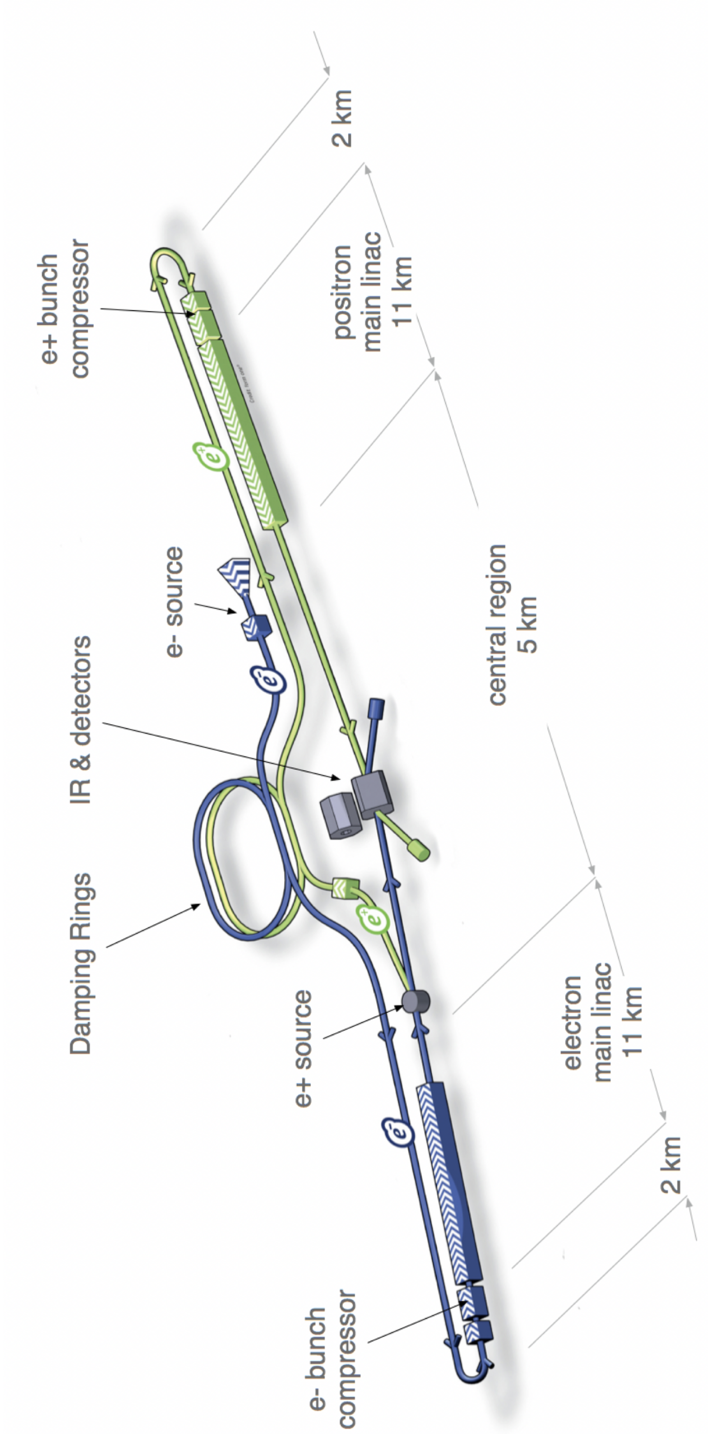

Figure 1.5: Schematic of the proposed design of the ILC at 500 GeV CM energy [21].

a plasma electron density of $10^{18}\ \mathrm{cm}^{-3}$, several orders of magnitude higher than conventional accelerating structures that are limited to gradients of the order of $100\,\mathrm{MV/m}$. Therefore, acceleration using plasma has the potential to reduce the size and cost of future particle accelerators.

1.4.1 Laser-driven wakefield acceleration

The concept of plasma wakefield acceleration of charged particles using a laser pulse was first introduced by Taijma and Dawson in 1979 [23], [24]. This is now known as laser wakefield acceleration (LWFA) [25] and involves using a laser pulse travelling at a velocity close to c to drive a wave in the plasma via its ponderomotive force. The ponderomotive force arising from the inhomogeneous oscillating electromagnetic field of the laser pulse expels plasma electrons from the axis. Since the ions are regarded as stationary due to their large inertia in the short time scales, strong fields can be created. This allows a witness particle bunch with the correct phase with respect to the drive bunch to be accelerated. As an example, Fig. 1.6 illustrates the plasma wave created by a $30\,\mathrm{fs}$ duration laser pulse with an intensity of $3 \times 10^{17}\ \mathrm{W/cm^2}$ in the so-called linear regime. In this regime the longitudinal electric field behind the laser pulse is sinusoidal and is shown in the bottom inset of Fig. 1.6.

As a result of the development of chirped-pulse amplification (CPA) [27] in the late 1980s, the laser intensities that could be achieved increased by five orders of magnitude [28]. When a laser pulse has sufficient intensity to expel plasma electrons in a large volume, the so-called bubble regime is formed which consists of an almost spherical sheath defining an ion cavity. An example of the plasma density perturbation and corresponding longitudinal electric field in the bubble regime is shown in Fig. 1.7. This arrangement produces the ideal conditions for efficient particle acceleration in three ways. First, the longitudinal electric fields

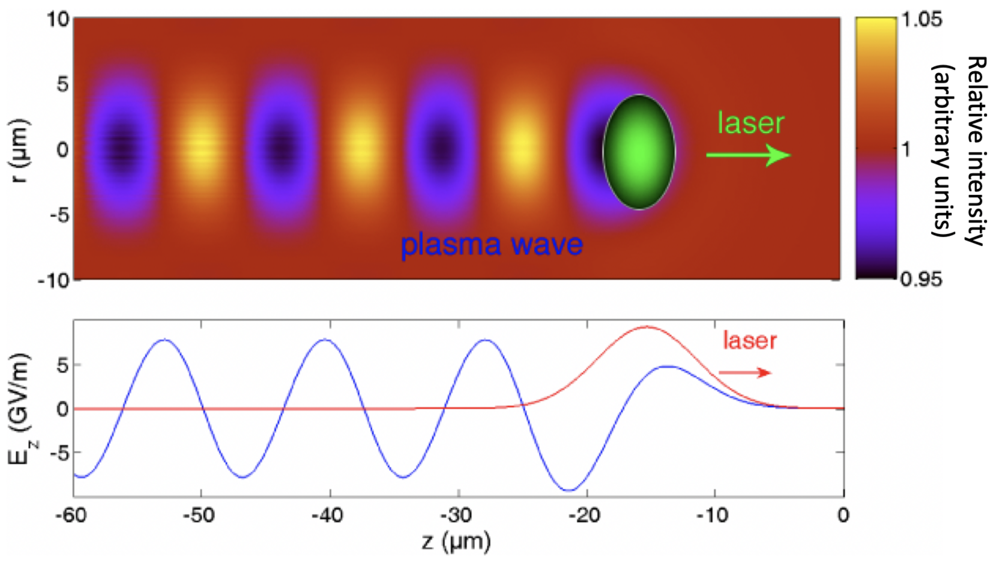

Figure 1.6: Plasma density perturbation (top) and longitudinal electric field in the linear regime (bottom) [26].

experienced by the witness beam doesn't depend on the radial position. This is advantageous in reducing the energy spread. Secondly, the magnitude of the transverse electric fields produced by the homogeneous distribution of background ions increases linearly with the radial distance. This creates a focusing lens which is beneficial for maintaining the transverse particle emittance. Lastly, the accelerated particles are separated in space from the drive beam. This is useful for maintaining the stability of the laser and preserving the witness beam quality. LWFA in the bubble regime was demonstrated for the first time in 2004 [29], [30], [31] where near-monoenergetic beams were produced.

The main limitations on the achievable energy gain of a witness beam through LWFA include laser diffraction and dephasing, or phase slippage, of the witness beam with respect to the drive beam. The plasma refractive index results in the laser drive beam having a group velocity less than c. The witness bunch can easily travel ahead of the drive bunch once the witness bunch reaches ultrarelativistic

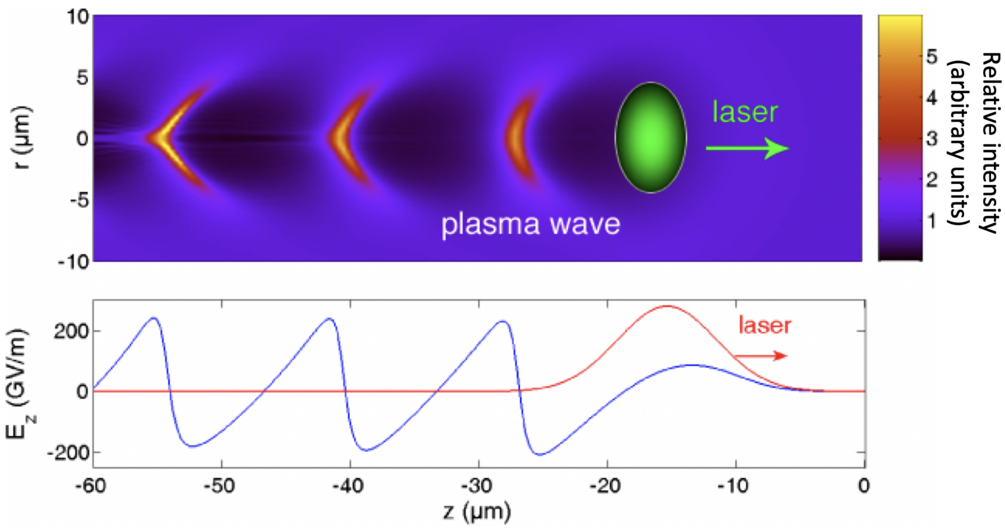

Figure 1.7: Plasma density perturbation (top) and longitudinal electric field in the bubble regime (bottom) [26].

energies causing it to enter a decelerating region [32]. Another limitation is the energy depletion of the drive beam as it transfers energy to the plasma waves.

Proposals for multi-stage LWFAs [33], [34] aim to address the limitations associated with phase slippage and energy depletion. However, the stringent requirements on the alignment of the beams and the timing between the stages provide technical challenges that still need to be overcome in order to move towards an operational multi-stage LWFA.

1.4.2 Particle-driven wakefield acceleration

Particle-driven wakefield acceleration (PWFA) that uses a particle bunch as a drive beam provides a few advantages over LWFA. In PWFA, the velocity of the particle drive bunch remains close to c so the acceleration is not limited by phase slippage. Plasma wakefield acceleration using an electron drive bunch was first proposed in 1985 by Chen et al. [35]. In electron-driven PWFA, the plasma electrons are expelled due to the space charge force of the drive bunch. The acceleration regime depends on the drive bunch density n_b. If $n_b \ll n_e$, then the density perturbation is small and the wakefield is sinusoidal at the plasma frequency. This is the linear regime. If $n_b > n_e$, then, just like the bubble regime in LWFA, plasma electrons are expelled from the bunch volume to form an electron free region. This non-linear regime is known as the blowout regime. An example of a PWFA experiment using an electron drive bunch is the E-157 experiment at SLAC National Accelerator Laboratory in 2007 [36]. A $42\,\mathrm{GeV}$, $50\,\mathrm{fs}$-long electron bunch with 1.8×10^{10} particles was used to generate wakefields in a $85\,\mathrm{cm}$-long lithium vapour cell with $n_e = 2.7 \times 10^{17}\ \mathrm{cm}^{-3}$. A promising peak accelerating gradient of $\sim 52\,\mathrm{GeV/m}$ was achieved for some electrons in the tail of the injected witness bunch.

One limitation of LWFA and electron plasma wakefield acceleration is the requirement for multiple stages to accelerate particles to high energies. This is due to the low energy of laser pulses and electron bunches which is limited to the order of $10\,\mathrm{J}$ [37]. On the other hand, proton accelerators like the Super Proton Synchrotron (SPS) at CERN can produce high population, high energy proton bunches that can store tens of kJ per bunch [38]. As a result, particle acceleration to high energies using a proton drive beam can be carried out in a single stage.

1.5 The AWAKE experiment

1.5.1 Experimental layout

The Advanced Proton Driven Plasma Wakefield Experiment (AWAKE) at CERN is a proof-of-principle experiment which focuses on electron-beam acceleration using the plasma wakefields generated by a proton drive bunch [39]. The experiment is located at the end of a $\sim 1\,\mathrm{km}$ line from SPS extraction shown in Fig. 1.8.

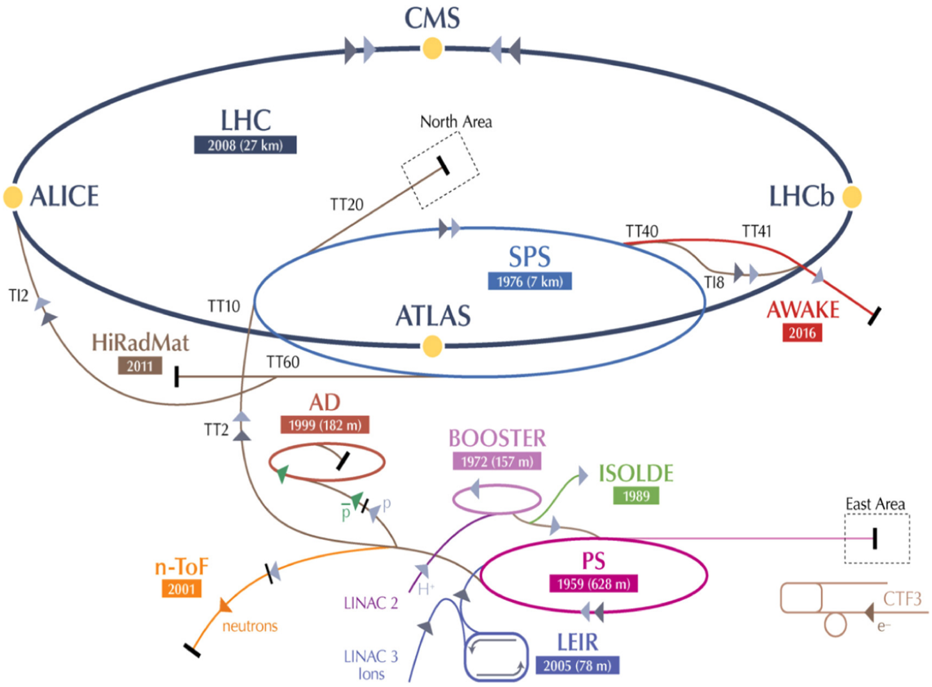

Figure 1.8: Schematic of the CERN accelerator complex [40]. The AWAKE experiment (in red) is located at the end of a ~ 1 km line from SPS extraction.

The experimental layout of AWAKE is shown in Fig. 1.9. The main components of the experiment include a proton beam, a plasma cell, a laser and an electron beam. The proton bunch, shown in red, is extracted every $15-30$ s from the SPS. The proton bunches have energies of $400\,\mathrm{GeV}$, a RMS bunch length of $6-8$ cm and bunch population typically between 2.5 and 3.1×10^{11} protons per bunch. Before entering the plasma cell, the bunch is focused to $200\,\mu\mathrm{m}$ transverse size. It then propagates through a $10\,\mathrm{m}$-long plasma cell that is comprised of rubidium (Rb) vapour with densities in the range $1-10\times10^{14}\,\mathrm{cm}^{-3}$ [41]. By heating the flasks located at either end of the cell, the density of the Rb vapour can be adjusted.

A very short laser pulse with a central wavelength of $780\,\mathrm{nm}$ and $450\,\mathrm{mJ}$

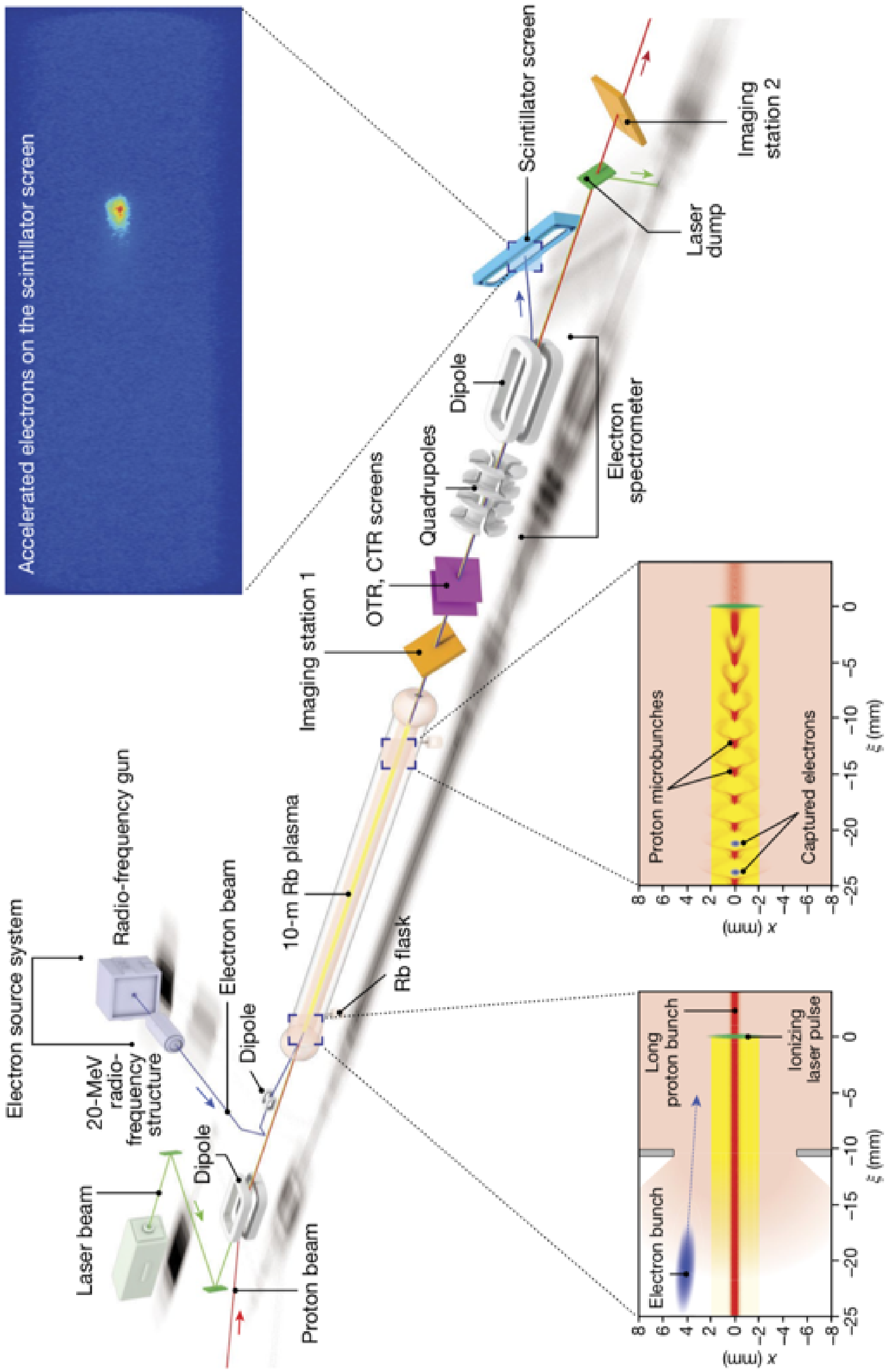

Figure 1.9: Schematic of the AWAKE set-up [38].

energy is used to ionize the vapour to form a plasma channel [41]. To effectively drive large amplitude wakefields of the order of $1\,\mathrm{GV/m}$, n_e should be of the order of $10^{14}\,\mathrm{cm}^{-3}$ and the drive beam should have a RMS longitudinal bunch size close to the plasma wavelength λ_p. For $n_e = 10^{14}\,\mathrm{cm}^{-3}$, this corresponds to sizes of $\sim 1\,\mathrm{mm}$. Since the proton bunch arriving at the plasma cell entrance has a length of approximately $6-8\,\mathrm{cm}$, the generation of large amplitude wakefields relies on a process called self-modulation where the long proton bunch forms micro-bunches with longitudinal sizes less than λ_p at a period of λ_p [42]. When the proton bunch enters the plasma cell, its space charge force creates an initial perturbation of the plasma electron density which creates the initial wakefields. This then generates a density modulation of the proton bunch which further enhances the electron density modulation. This feedback loop continues until saturation. Whilst the self-modulation instability (SMI) is initiated from the statistical particle distribution in the bunch and plasma, seeded self-modulation (SSM) is initiated by the abrupt start of the plasma/bunch interaction that is created by the laser pulse propagating with and within the proton bunch as shown in the second inset of Fig. 1.9. This reduces the length required for self-modulation to saturate. It also allows for a reference phase for the start of the SSM process to be determined so that electrons can be injected at the correct phase in order to be focused and accelerated.

The electrons, shown in blue in Fig. 1.9, are produced at a rate of $10\,\mathrm{Hz}$ by the Photo-Injector (PHIN) electron gun, previously used at the CERN Compact Linear Collider Test Facility (CTF3), with electron energies of $5\,\mathrm{MeV}$ [43]. The electrons are then accelerated to energies between $10-20\,\mathrm{MeV}$ by a linac booster [44]. The bunch population can range from 0.6 to 6.2×10^9 electrons per bunch, the bunch length is typically $4\,\mathrm{ps}$ $(1.2\,\mathrm{mm})$ and the normalised RMS emittance is $2\,\mathrm{mm\ mrad}$ [45].

AWAKE Run 1 (2016 - 2018) successfully demonstrated the self-modulation of a proton bunch into a train of over 20 micro-bunches [46]. The experiment was also successful in accelerating electrons from $19\,\mathrm{MeV}$ to $2\,\mathrm{GeV}$ in $10\,\mathrm{m}$ of Rb vapour [38]. Plans for Run 2 a and b (2021 - 2024) include the study of proton bunch SSM with electron bunch seeding and the effect of a plasma density step for maintaining wakefield amplitudes near saturation over longer distances [47].

1.5.2 Particle beam instrumentation

Instruments to measure the SSM process and the electron bunch properties post acceleration are vital for demonstrating the experimental outcomes of AWAKE. Furthermore, diagnostic systems for transverse profile measurements, temporal synchronisation and beam position monitoring are crucial for the operation of the experiment.

The SSM process can be measured directly with an optical transition radiation (OTR) screen, which is composed of a silver-coated silicon wafer, and a streak camera which provides the bunch profile in space and time. The coherent part of the spectrum, called coherent transition radiation (CTR), can be measured and analysed with a second metallic foil, and detection based on high-pass filtering and Schottky diodes, and heterodyne mixing systems [48]. Coherent transition radiation is particularly useful for measuring higher harmonics of the modulation frequency [40], [49]. The OTR and CTR screens are shown in purple in Fig. 1.9.

To measure the energy of the electrons, a magnetic spectrometer is used (Fig. 1.9, right). Two quadrupoles located downstream of the plasma cell focus the electron beam horizontally and vertically before deflection via a C-shaped dipole with magnetic field strength adjustable in the range $0.1 - 1.4\ \mathrm{T}$ [38]. Electrons within a certain energy range are incident on a gadolinium oxysulfide (Gd_2O_2S:Tb) scintillator screen (Fig. 1.9, top right inset). The light is transported $17\,\mathrm{m}$ to a charge-couple device (CCD) camera. The energies of the electrons are obtained from their horizontal position on the screen.

For transverse profile measurements, a total of six beam television screens (BTVs) are used [50]. These are installed in both the electron line, and the common line before and after the plasma cell. The two BTVs installed after the plasma cell are shown as imaging stations 1 and 2 in Fig. 1.9. All the BTVs are comprised of either a scintillating Chromox (Al_2O_3:Cr_2O_3) screen or OTR screen linked to a camera imaging system [49]. Whilst the scintillation screen has a higher light yield, the emission tails are a few hundred ms long. As a result, the first BTV in the common line uses an OTR screen coupled to a $200\,\mathrm{fs}$ resolution streak camera to synchronise the beams in time [51].

The proton beam position monitoring system is made up of 21 dual plane button-style beam position monitors (BPMs) distributed between the SPS proton beam extraction and the end of the AWAKE beam-line [50]. In addition, a total of seven $40\,\mathrm{mm}$ inner diameter and five $60\,\mathrm{mm}$ inner diameter shorted stripline BPMs developed by TRIUMF [52], Canada's national particle accelerator centre, are used for electron beam position measurements in the electron and common line before the plasma cell, and operate at $404\,\mathrm{MHz}$. Measurements have demonstrated a position resolution of $10\,\mathrm{\mu m}$ in both planes [51].

1.6 Motivation and thesis outline

The electron stripline BPMs located in the common beam-line at AWAKE operate at a frequency where the proton signal dominates. Therefore, they cannot measure the electrons in the presence of the more-intense proton bunches. By taking advantage of the different bunch lengths of the two particle beams, and designing a BPM to operate at a frequency within the electron bunch spectrum, but well outside of the proton bunch spectrum, the electrons can be discriminated from the protons.

A BPM based on Cherenkov diffraction radiation (ChDR) is an attractive solution to address this problem due to the various advantages that ChDR offers. These include its none-invasive nature, its accessibility due to its well-defined emission angle, and its high photon-yield.

Previous experiments included studies of both the incoherent and coherent parts of the emission spectrum of ChDR produced by various dielectric target shapes and materials when a charged particle beam passes in close proximity. The angular and spectral properties of incoherent ChDR generated from a fused silica target in-air were studied extensively at the Cornell Electron Storage Ring (CESR) [53] and transverse beam profile measurements were performed whilst varying the impact parameter, i.e. the distance of the beam with respect to the entrance face of the dielectric target [54] [55]. Further studies of incoherent ChDR and its use for a BPM were conducted at the Diamond Light Source [56] [57]. In terms of a BPM operating in the coherent ChDR regime, initial studies were performed in-air at the CERN Linear Electron Accelerator for Research (CLEAR) test facility [58] using 18 mm diameter cylindrical PTFE targets, and detection based on waveguide networks and Schottky diodes, and are detailed in [59].

This thesis builds upon previous work demonstrating the proof of principle of the BPM based on coherent ChDR but with a specific focus on its application at the AWAKE common beam-line. It begins with a general background of particle beam position monitoring using the electrostatic button BPM as an example in Chapter 2. This chapter ends with a more detailed discussion of the motivation for a BPM operating at high frequencies for the AWAKE common beam-line to address the problem of electron beam detection in the presence of a more-intense proton bunch.

Chapter 3 provides the theoretical model that describes ChDR emitted from simple geometries and compares it to numerical simulations.

Chapter 4 describes the design process of the ChDR BPM for AWAKE using numerical analyses. It also includes the theoretical background, design and experimental results of an RF-test bench characterisation of the pick-up (PU) which aimed at bridging the gap between numerical simulations and beam studies.

Chapter 5 goes through the details of the beam tests at AWAKE and the experimental campaign at CLEAR.

The final part, Chapter 6, concludes the thesis, and includes a description of the main findings of the numerical and practical work, and proposals for future studies.

2 Particle beam monitoring

Measuring and monitoring the charged particle beams travelling in the beam pipe of an accelerator allows one to observe the beam and to characterize its properties. Amongst the various observation methods, the detection of the electromagnetic field of the beam particles enables an almost non-invasive beam measurement, which can be utilized, for example, to quantify the beam intensity, or the beam trajectory (in circular accelerators called the beam orbit), as well as many other beam properties. The measurement of the beam trajectory is based on BPMs, i.e. a series of electromagnetic detectors located along the beam-line, sensing the transverse position of the beam w.r.t. the centre of the beam pipe, or in other words, the transverse beam displacement.

2.1 Relativistic charged particles

The electromagnetic (EM) field pattern generated by a stationary charged particle differs from the field pattern generated by a particle moving with constant velocity. The proton and electron beams in the AWAKE beam-line are travelling with relativistic velocity, $\beta = v/c \approx 1$. Therefore, the EM-field of a relativistic beam interacting with the detection electrodes of a BPM needs to be analyzed.

The electric field of a point charge or point-like particle q at rest at a distance $\vec{r}$ from the particle is given by [60]

$$\vec{E} = \frac{q}{4\pi\epsilon_0}\frac{\vec{r}}{r^3}, \tag{2.1}$$

where q is the particle charge and $r = \sqrt{x^2 + y^2 + z^2}$, and x, y and z are the Cartesian coordinates. The distribution of the electric field of a charged particle at rest is illustrated in a 2-dimensional plane in Fig. 2.1a [61]. The electric field is isotropic.

If the charged particle is moving with a constant velocity $v = \beta c$ in the z direction and has a location of $(0, 0, vt)$ at time t, then the electric field components as viewed by an observer located at (x, y, z) are

$$E_x = \frac{\gamma q}{4\pi\epsilon_0} \frac{x}{[x^2 + y^2 + \gamma^2(z - vt)^2]^{3/2}}, \tag{2.2}$$

$$E_y = \frac{\gamma q}{4\pi\epsilon_0} \frac{y}{[x^2 + y^2 + \gamma^2(z - vt)^2]^{3/2}}, \tag{2.3}$$

$$E_z = \frac{\gamma q}{4\pi\epsilon_0} \frac{z - vt}{[x^2 + y^2 + \gamma^2(z - vt)^2]^{3/2}}, \tag{2.4}$$

where γ is the Lorentz factor given by

$$\gamma = \frac{1}{\sqrt{1 - \beta^2}}. \tag{2.5}$$

If we consider the case where $(z - vt) = 0$, i.e. at right angles to the direction of motion, then the total field strength at a distance $\sqrt{x^2 + y^2}$ is $\sqrt{E_x^2 + E_y^2}$ which can be written as

$$E = \frac{\gamma q}{4\pi\epsilon_0} \frac{1}{x^2 + y^2}. \tag{2.6}$$

From Equation 2.6, the electric field strength is increased by a factor γ relative to the static case. The Lorentz factor γ can also be defined as the ratio of the particle energy to its rest mass. Therefore, the EM field of a charged particle moving at constant velocity not only has charge and position dependence but is also dependent on the particle energy. For the case where x and y are zero, i.e. in

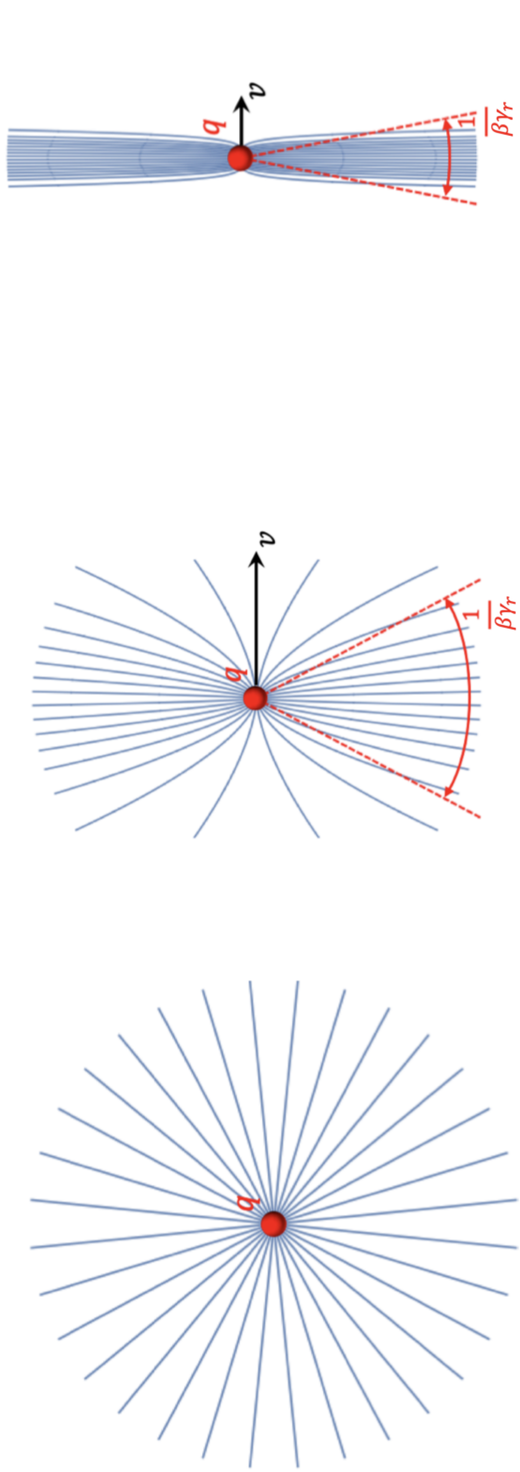

(a) Stationary.

(b) $\beta = 0.6$.

(c) $\beta = 0.9$.

Figure 2.1: Distributions of the electric field of a point charge travelling at different constant velocities [61].

the longitudinal direction, the electric field strength is

$$E = E_z = \frac{q}{4\pi\epsilon_0\gamma^2}\frac{1}{(z-vt)^2}. \tag{2.7}$$

The field is reduced by $1/\gamma^2$ relative to the static case. This is indicated in Fig. 2.1b. As the particle velocity approaches c, the electric field distribution can be estimated as purely transverse, as shown in Fig. 2.1c. In the limit where $\beta \to 0$, Equations 2.6 and 2.7 reduce to Equation 2.1.

The magnetic field of a relativistic charged particle can also be calculated via

$$\vec{B} = \frac{\vec{v}\times\vec{E}}{c^2}. \tag{2.8}$$

When the velocity is crossed with a radially extending electric field, the resulting magnetic field is azimuthal around the direction of motion as shown in Fig. 2.2 [62].

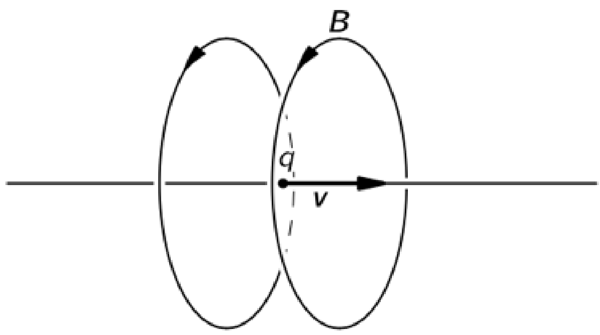

Figure 2.2: Magnetic field of a charged particle travelling at v [62].

2.2 Image current model and beam position measurement

In accelerators, particles travel through metallic vacuum chambers, the already mentioned beam pipes. Each charged particle q of the beam is associated with an image charge $-q$ in the conductive wall of the beam pipe, and both are linked by the beam's EM field. As a result, the beam current I_{beam} is compensated by an image or wall current I_{wall} of same quantity

$$I_{beam} = -I_{wall}. \tag{2.9}$$

For relativistic beams, $\beta = v/c \approx 1$, moving in the z direction, the z component of the beam field vanishes and their EM fields can be approximated as transverse electromagnetic (TEM) as was shown in Section 2.1. As with the TEM field, the problem of image charge distribution in the cross-section of the beam pipe can be simplified as a 2-dimensional electrostatic problem. If the beam is on the axis of a cylindrical beam pipe of circular cross-section, the image charges, and therefore the wall current density J_{wall} i.e. the current per unit length of surface, has a uniform distribution, as illustrated in Fig. 2.3a.

$$J_{wall} = -\frac{I_{beam}}{2\pi R}, \tag{2.10}$$

where R is the beam pipe radius.

When the beam is off-centre, the wall current density is associated with the beam position, i.e. higher on the side of the wall that is closer to the beam and lower on the side of the wall that is further away from the beam. This is illustrated in Fig. 2.3b where the beam is offset to a position $(x = r\cos\varphi, y = r\sin\varphi)$. The

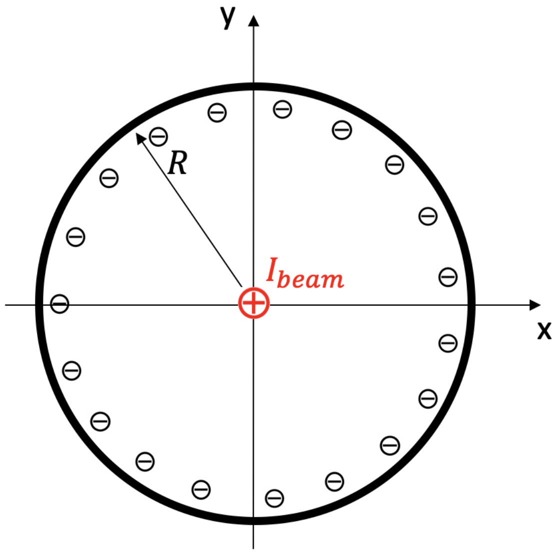

(a) Centred beam.

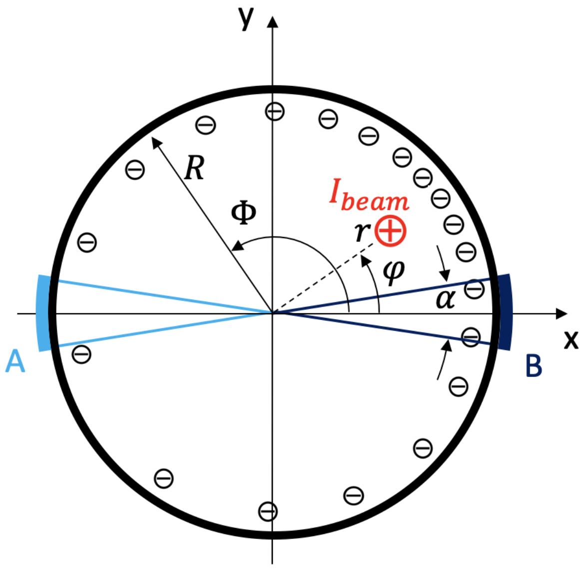

(b) Off-centred beam.

Figure 2.3: Image charge distribution of a cylindrical beam pipe represented as a 2D cross-section. Image adapted from [61].

image current density induced on the wall is [61]

$$J_{wall}(R, \Phi, r, \varphi) = -\frac{I_{beam}}{2\pi R}\frac{R^2 - r^2}{R^2 + r^2 - 2Rr\cos(\Phi - \varphi)}. \tag{2.11}$$

If we now consider two identical, symmetrically arranged electrodes, left (A) and right (B) as shown in Fig. 2.3b, on opposite sides of the beam pipe in the horizontal plane, each covering an angle α, then the portion of the total wall current induced on each electrode is

$$I_{A,B} = R\int_{\mp\alpha/2}^{\pm\alpha/2} J_{wall}(R, \Phi, r, \varphi)\, d\Phi. \tag{2.12}$$

The image currents induced on these electrodes can be used to determine, in this case, the horizontal position of the beam, e.g. approximated by the Δ/Σ normalization

$$\text{hor. position} = \frac{\Delta}{\Sigma} = \frac{I_A - I_B}{I_A + I_B} \simeq \frac{4\sin\alpha/2}{\alpha}\frac{x}{R} + \mathcal{O}\left(\frac{x^2}{R^2}\right) \tag{2.13}$$

for a beam-intensity-independent beam position measurement. If the beam displacement is small, $x^2 + y^2 \ll R^2$, and α is small, $\sin\alpha/2 \approx \alpha/2$, then the horizontal beam position can be estimated from

$$\text{hor. position} = \frac{I_A - I_B}{I_A + I_B} \approx \frac{2}{R}x, \tag{2.14}$$

where $2/R = k_{BPM}$ is often referred to as the monitor constant of the BPM pick-up. A similar formalism can be followed for a second pair of electrodes in the vertical plane in order to determine the vertical beam position.

2.3 Response of an electrostatic button BPM

We classify the different types of BPMs in resonant and broadband pick-up monitors. Cavity BPMs are passive resonant pick-up monitors where the beam-induced TM010 monopole mode couples to the intensity of the particle beam and the TM110 dipole mode couples to the particle beam position. The position characteristic of the broadband BPMs follow the image charge model discussed in the previous section, with stripline and button type BPMs being the most popular. While the position characteristic of a broadband BPM is independent of the bunched beam longitudinal particle distribution, i.e. the time domain bunch waveform, or spectral contents of the beam, the transfer response of the BPM in time or frequency domain is given by the type and shape of the pick-up electrodes.

As an example, the electrostatic button BPM will be discussed. This comprises four symmetric, insulated, round, metallic electrodes (buttons) that are usually distributed evenly across the perimeter of a circular beam pipe. They are usually organised with two electrodes in the horizontal plane and two in the vertical plane except in synchrotron light sources where they are positioned to avoid the horizontal plane. This is done to reduce the interference of synchrotron radiation on the measured signals. An example of a button pick-up is shown in Fig. 2.4.

The electrostatic button BPM operates on the principle of image currents, as described in Section 2.2, in order to perform a beam position measurement. The beam consists of many charged particles, typically between 10^9 and 10^{11}, spread in the xy transverse plane by sizes between 10 and $100\,\mu\mathrm{m}$. As the BPM is a linear system, the superposition principle applies and assuming a linear position characteristic, Eq. 2.14, the BPM detects the displacement of the centre-of-charge of a particle bunch. The response of the BPM pick-up electrodes is an electrical signal, which is then processed by the front-end electronics. Therefore, it is essential to understand the transfer response and the signal output of the PUs.

Fig. 2.5a shows a schematic of a capacitive button BPM where two electrodes are shown. The electrodes are round, coin-like buttons and each have a diameter

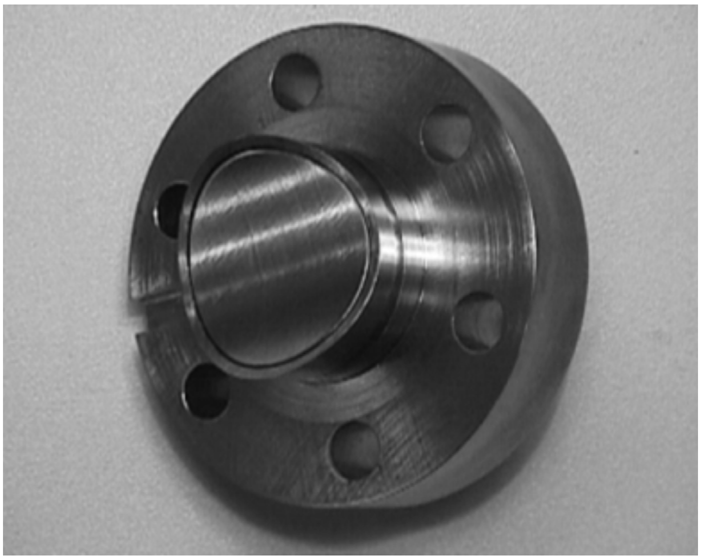

Figure 2.4: Example of a button electrode [61].

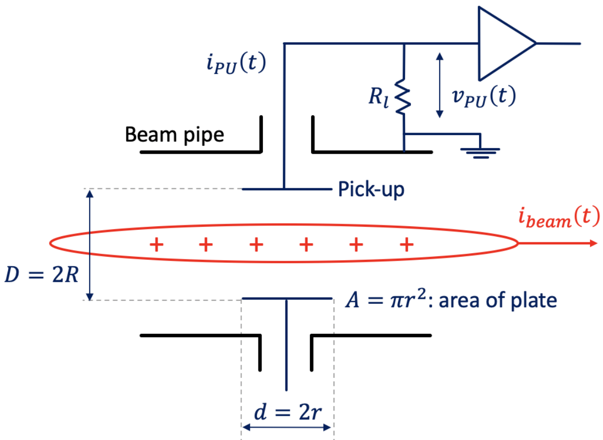

(a) The interaction of the beam with the buttons.

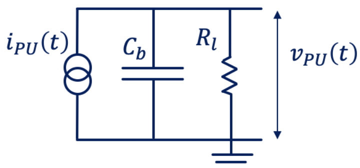

(b) Equivalent circuit.

Figure 2.5: Schematic of a capacitive BPM. Image adapted from [63].

$d = 2r$, covering an area $A = \pi r^2$ of the beam pipe. The distance between the electrodes is the beam pipe diameter $D = 2R$. The image current intercepted by the button electrode i_{PU} is given by a geometric coverage factor ϕ, i.e. the ratio of the button area A to the total surface area of the beam pipe spanning the button [63]:

$$i_{PU}(t) = -\phi \frac{dq_{beam}(t)}{dt} = -\frac{\pi r^2}{2\pi R \cdot 2r} \frac{dq_{beam}(t)}{dt} = -\frac{r}{2D} \frac{dq_{beam}(t)}{dt}, \tag{2.15}$$

where the derivative of the beam charge can be written as

$$\frac{dq_{beam}(t)}{dt} = \Delta t \frac{di_{beam}(t)}{dt} = \frac{2r}{\beta c} \frac{di_{beam}(t)}{dt}. \tag{2.16}$$

In Eq. 2.16, Δt is the transit time it takes a particle to pass the button electrode. Combining Equations 2.15 and 2.16 gives the induced current of a button pick-up electrode in the time domain

$$i_{PU}(t) = -\frac{r^2}{D} \frac{1}{\beta c} \frac{di_{beam}(t)}{dt}. \tag{2.17}$$

However, in the following it is more convenient to express this term in the frequency domain

$$I_{PU}(\omega) = i\omega \frac{r^2}{D} \frac{1}{\beta c} I_{beam}(\omega), \tag{2.18}$$

with ω being the angular frequency. To compute the voltage V_{PU} observed at a load resistor R_l, we have to include the button capacitance C_b, which is determined by the distance between the insulated button electrode and grounded beam pipe, see also the equivalent circuit in Fig. 2.5b. Applying Ohm's law gives

$$V_{PU}(\omega) = Z(\omega) I_{PU}(\omega) \tag{2.19}$$

with

$$\frac{1}{Z(\omega)} = \frac{1}{R_l} + i\omega C_b \Longleftrightarrow Z(\omega) = \frac{R_l}{1 + i\omega R_l C_b} \tag{2.20}$$

being the frequency dependent impedance of the equivalent circuit.

Combining Equations 2.18, 2.19 and 2.20, the output voltage of the button electrode can then be expressed as

$$V_{PU}(\omega) = \frac{R_l}{1 + i\omega R_l C_b} I_{PU}(\omega) = \frac{i\omega R_l C_b}{1 + i\omega R_l C_b} \frac{1}{C_b} \frac{r^2}{D} \frac{1}{\beta c} I_{beam}(\omega) \equiv Z_t(\omega) I_{beam}(\omega), \tag{2.21}$$

The transfer impedance $Z_t(\omega)$ of a button pick-up electrode, which depends on the geometric dimensions of the button and the beam pipe, the load resistance R_l and the velocity of the passing beam βc, describes a high-pass filter of 1st-order. The 3 dB cut-off frequency of the high-pass filter is given by $f_{3dBbutton} = \omega_{3dBbutton}/2\pi = (2\pi R_l C_b)^{-1}$.

In practice, the load resistor R_l, representing the input impedance of the read-out electronics, is connected through a coaxial cable of $Z_0 = 50\,\Omega$ characteristic impedance to the button electrode, and therefore $R_l = Z_0 = 50\,\Omega$ to avoid unwanted signal reflections. However, the button source impedance $Z_s = Z(\omega) \neq 50\,\Omega$ given in Equation 2.20 is frequency dependent and is not $50\,\Omega$. Therefore, any impedance mismatch or reflections on the load side will be reflected at the button as its source is not matched to $50\,\Omega$. This often causes "ghost" bunch signals following the bunch signal that is $2\times$ the cable delay. Furthermore, the RC equivalent circuit Fig. 2.5b is a simplification. In practice, the internals of the button feedthrough contains a series of discontinuities and cavities with high eigen-frequencies, and, if beam-excited, cause unwanted signal ringing effects. The button capacitance typically ranges between $C_b = 3\,\mathrm{pF}$ and $10\,\mathrm{pF}$, which leads to $f_{3dBbutton} = 300\,\mathrm{MHz}$ and $1000\,\mathrm{MHz}$ for the typical high-pass cut-off frequency of a button.

In most cases, the beam signal $i_{beam}(t)$ or $I_{beam}(\omega)$ can be approximated by a Gaussian distribution function, following the longitudinal density distribution of the particles in a beam bunch. Both the time domain beam signal

$$i_{beam}(t) = \frac{eN}{\sqrt{2\pi}\sigma_t} \exp\left\{ \left(-\frac{1}{2}\frac{t^2}{\sigma_t^2} \right) \right\}, \tag{2.22}$$

and the frequency domain equivalent

$$I_{beam}(\omega) = eN \exp\left\{ \left(-\frac{1}{2}\omega^2 \sigma_t^2 \right) \right\} \tag{2.23}$$

are Gaussian functions, where N is the number of charged particles in the beam bunch, and $\sigma_t = \sigma/\beta c$ is the bunch length in time.

Equation 2.23 has a low-pass filter characteristic and the 3 dB cut-off frequency is linked to the one-sigma bunch length by

$$f_{3dBGauss} = \frac{\sqrt{\frac{\ln \sqrt{2}}{2}}}{\pi} \frac{1}{\sigma_t} \approx \frac{0.1325}{\sigma_t}. \tag{2.24}$$

Combining Equations 2.21 and 2.23 gives the PU output voltage drop at the load resistor for a Gaussian beam bunch

$$\begin{aligned} V_{PU}(\omega) &= \frac{i\omega R_l C_b}{1 + i\omega R_l C_b} \frac{1}{C_b} \frac{r^2}{D} \frac{eN}{\beta c} \exp\left\{ \left(-\frac{1}{2}\omega^2 \sigma_t^2 \right) \right\} \\ &\approx \frac{i\omega/\omega_{3dBbutton}}{1 + i\omega/\omega_{3dBbutton}} \frac{1}{C_b} \frac{r^2}{D} \frac{eN}{\beta c} \exp\left\{ \left(-0.3465\, \omega^2/\omega_{3dBGauss}^2 \right) \right\}. \end{aligned} \tag{2.25}$$

There is no closed-form solution to transform Eq. 2.25 into the time domain. However, a brief discussion reveals some basic properties. If $f_{3dBGauss} \gg f_{3dBbutton}$, which means the bunch length is small compared to the button size, $\sigma \ll 2r$, then

$$Z_t \propto \frac{i\omega/\omega_{3dBbutton}}{1 + i\omega/\omega_{3dBbutton}} \to 1 \tag{2.26}$$

and the output voltage

$$v_{PU}(t) \approx \frac{1}{C_b}\frac{r^2}{D}\frac{1}{\beta c} \cdot i_{beam}(t) \tag{2.27}$$

is almost a direct replica of the particle-beam time structure with no phase shift. For typical button electrodes, the transfer impedance factor is $r^2/C_b D\beta c \approx 0.5\,\Omega$ to $1\,\Omega$.

If $f_{3dBGauss} \ll f_{3dBbutton}$, i.e. the beam bunch is much longer than the button diameter, $\sigma \gg 2r$, then

$$Z_t \propto \frac{i\omega/\omega_{3dBbutton}}{1 + i\omega/\omega_{3dBbutton}} \to i\frac{\omega}{\omega_{3dBbutton}}, \tag{2.28}$$

and the output voltage approximates to

$$\begin{aligned} v_{PU}(t) &\approx \frac{r^2}{D}\frac{R_l}{\beta c}\frac{di_{beam}(t)}{dt} \\ &\approx \frac{r^2}{D}\frac{R_l}{\beta c}\frac{eN}{\sqrt{2\pi}\sigma_t^3} t \exp\left\{\left(-\frac{1}{2}\frac{t^2}{2\sigma_t^2}\right)\right\} \end{aligned} \tag{2.29}$$

This shows that the output voltage is proportional to the derivative of the beam current.

Since the output voltage $V_{PU}(\omega)$ (Equation 2.25) of each button electrode still depends on the bunch charge, a difference-over-sum of the voltage signals of a pair of symmetrically arranged electrodes can be used to remove the beam charge dependence, enabling a beam intensity-independent position measurement. For example, assuming small horizontal beam displacements x, the beam intensity-independent horizontal position can then be calculated via [61] [63]

$$\text{hor. pos.} \quad x \approxeq S_x \frac{V_L - V_R}{V_L + V_R} \equiv S_x \frac{\Delta V_x}{\Sigma V_x}, \tag{2.30}$$

where V_L and V_R are the voltage signals of the left and right electrodes in the horizontal direction respectively, and $S_x = 1/k_{BPM} \approx R/2$ is the position sensitivity of the BPM pick-up.

Expanding the measured signals V_R and V_L of Equation 2.30 in correlated, true $BPMx$ signal parts and uncorrelated, statistical $noise$ signal parts:

$$x \approxeq S_x \frac{\Delta V_x}{\Sigma V_x} = S_x \frac{\Delta_{BPMx} + \Delta_{noise}}{\Sigma_{BPMx} + \Sigma_{noise}} \approx S_x \frac{\Delta_{BPMx}}{\Sigma_{BPMx}} + \underbrace{S_x \frac{\Delta_{noise}}{\Sigma_{BPMx}}}_{\text{resolution}} \tag{2.31}$$

allows one to estimate the theoretical achievable resolution of the BPM

$$\begin{aligned} S_x \frac{\Delta_{noise}}{\Sigma_{BPMx}} = \text{resolution} &= S_x \frac{V_{Rnoise} - V_{Lnoise}}{V_{R_{BPM}} + V_{L_{BPM}}} \\ &\approxeq S_x \frac{\sqrt{2}\, N}{2\, S} = \frac{S_x}{\sqrt{2}} \left(\frac{S}{N} \right)^{-1} \end{aligned} \tag{2.32}$$

based on the signal-to-noise ratio S/N, with $S = V_R \approx V_L$ and $N = V_{noise} = V_{Rnoise} \approxeq V_{Lnoise}$ being the thermal noise voltage of the load resistor R_l of the signal processing input

$$V_{noise} = \sqrt{4 k_B T R_l \cdot \Delta f}. \tag{2.33}$$

The Boltzmann constant is k_B, T is the temperature of load R_l and Δf is the overall bandwidth of the signal processing system. The same equations follow for the vertical displacement y.

2.4 Two-beam detection

When two beams are present e.g. an electron and proton beam, the detection of the position of the individual beams becomes more complex as the fields on the pick-up electrodes is a superposition of all beam fields. For two counter-propagating beams, the stripline BPM is a solution, and is often applied for the beam position measurement of the beams near the interaction point in the common beam-line of a collider. Unlike button BPMs, stripline BPMs have 4+4 output signal ports (Fig. 2.6) which distinguish the beam direction, i.e. directivity, separating the beam position of the two beams at their upstream signal ports. Moreover, often the bunch signals of the two beams are not exactly aligned in time, which allows a time discrimination of their signals.

For two co-propagating beams, with their beam bunches aligned in time, the situation for the detection of the position of the individual beam bunches is a much more challenging task. This is the situation in the common line before the plasma cell at AWAKE where both, the electron and the proton beams co-propagate. Typ-

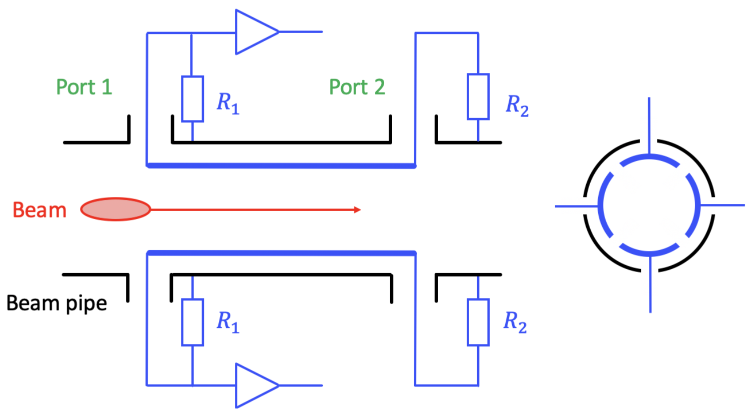

Figure 2.6: Schematic of a stripline BPM with longitudinal view (left) and transverse view (right). Image adapted from [64].

ical parameters for these beams are presented in Table 2.1. Their beam distributions, assuming perfect Gaussian beams, in the time and frequency domain are shown in Fig. 2.7. At $1.88\,\mathrm{GHz}$, the two beams have equal spectral powers. Below this frequency, the proton signal dominates with 38 dB more power at DC than the electron signal and above this, the electron signal dominates. Measurements of the electron beam position with the existing stripline BPMs operating at $404\,\mathrm{MHz}$ are dominated by the proton signal when both beams are present. In order to measure only the electron signal in the presence of the longer and more-intense proton bunch, we consider frequency discrimination as the way to separate the proton error signal from the electron bunch signal. Therefore, a BPM system needs to be designed to operate at frequencies higher than a few GHz.

Table 2.1: Proton and electron beam parameters at AWAKE [45].

Particle beam	Charge/nC	σ_t/ps
Proton	48	250
Electron	0.6	4

Although from this simplistic model where Gaussian bunched beams are assumed and a BPM operating frequency of more than a few GHz seems sufficient in isolating the electron signal, in reality, the proton longitudinal bunch profile is not a perfect Gaussian distribution and the frequency spectrum extends higher. This was shown at AWAKE via streak camera measurements of the OTR from the screen $3.5\,\mathrm{m}$ downstream of the plasma cell where the proton bunch profile in some shots extended up to $200\,\mathrm{GHz}$ [59]. It was also seen that there was a high shot-to-shot variability. Although the measurement noise was also included in the proton spectrum above $5\,\mathrm{GHz}$, limiting the precision of the bunch profile past this frequency, the study provided a preliminary indication of the desired operating frequency of a BPM. The frequency range in which the signal from a $300\,\mathrm{pC}$,

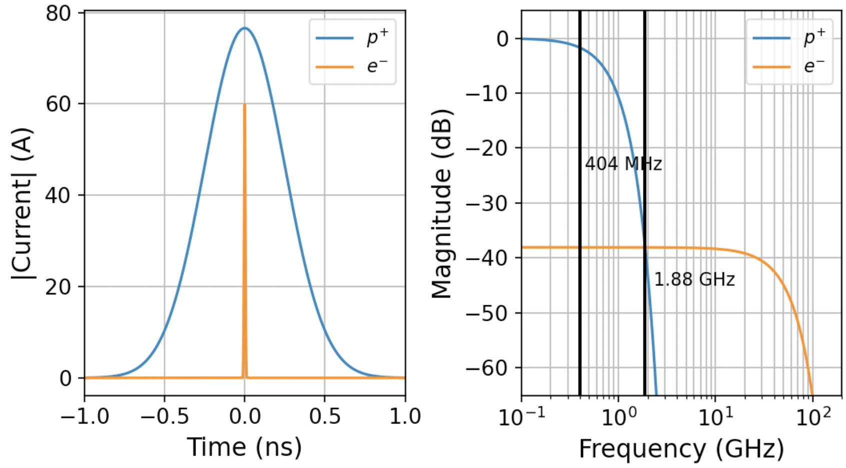

Figure 2.7: Proton and electron beam distributions in the time and frequency domain for typical AWAKE parameters shown in Table 2.1.

$\sigma_t = 4\,\mathrm{ps}$ Gaussian electron bunch is higher than the average spectrum of a $48\,\mathrm{nC}$, $\sigma_t = 250\,\mathrm{ps}$ proton bunch, as measured by the streak camera, was estimated to be between 15 and $40\,\mathrm{GHz}$.

Based on this design consideration, a BPM is required to operate in this high frequency range in order to discriminate the electrons from the protons at AWAKE. Since manufacturing an electrostatic button BPM to operate at these high frequencies is mechanically challenging, and as shown the button BPM also transfers bunch signals at low frequencies, a new design for a BPM based on Cherenkov diffraction radiation was proposed and will be discussed in the following chapters.

3 Theory of Cherenkov diffraction radiation

3.1 Polarisation radiation

When a charged particle travels uniformly through a dielectric medium, or in close proximity to it, radiation is produced. The underlying mechanism for the creation of this radiation is the polarisation of the atoms in the medium due to the Coulomb field of the moving charge [65]. This creates dipoles where the atomic electrons are displaced and oscillate around the nucleus. As they do so, they produce currents called polarisation currents that produce radiation, known as polarisation radiation (PR). Depending on the geometry of the medium, and whether the charged particle travels through or in close proximity to it, different types of PR are produced. These include Smith-Purcell radiation (SPR), transition radiation (TR), diffraction radiation (DR), Cherenkov radiation (ChR) and Cherenkov diffraction radiation (ChDR).

Smith-Purcell radiation is produced when a charge particle passes above a diffraction grating. It is commonly used for non-destructive beam measurements such as measurements of the bunch length. Transition radiation occurs when a charged particle crosses the boundary between two media, each with different homogeneous permittivity [66]. In accelerators, this type of radiation is exploited for measurements of the particle beam properties such as the longitudinal, and, more commonly, the transverse bunch profiles by placing a screen in the vacuum chamber. A disadvantage of this is that it involves a direct interaction between the particle beam and the screen. Therefore, it is a destructive measurement. Diffraction radiation, which can be viewed as a non-invasive form of TR, is generated when a charged particle passes near a medium [67]. In contrast to these two types of radiation, where the medium is spatially inhomogeneous, ChR is generated when a relativistic charged particle travels inside a homogeneous medium with a velocity greater than the phase velocity of light in that medium [68]. Cherenkov diffraction radiation exhibits similar properties to ChR. However, in the case of ChDR, the particle does not need to travel through the medium but only in close proximity to it [69], [70]. As a result of the non-invasive nature of ChDR, as well as the other advantages that ChDR offers such as its well-defined emission angle and high photon yield, it has attracted attention for possible applications in particle beam diagnostics which has led to the development and testing of proof-of-principle devices in recent years [71], [72]. The various types of PR can be further divided into the coherent and incoherent regimes, where coherent emission occurs at wavelengths equal to or longer than the longitudinal bunch length. In this regime, the intensity of the emitted radiation scales with the bunch charge squared. At wavelengths much shorter than the longitudinal bunch length, the radiation is emitted incoherently.

The formalism describing all types of polarisation radiation through polarisation currents is called the Polarisation Current Approach (PCA). The theory of the PCA for ChDR will be discussed in the following sections for a particular dielectric geometry and a comparison will be made to numerical simulations.

3.2 Cherenkov radiation

The theory of Cherenkov radiation was developed by Frank and Tamm in 1937 [73]. It describes the generation of radiation by a charged particle as it travels through a medium where its velocity is greater than the phase velocity of light in that medium. This is the Cherenkov condition

$$v_p > \frac{c}{n}, \tag{3.1}$$

where v_p is the velocity of the charged particle and n is the refractive index of the medium. Under this condition, the spherical wavefronts generated by the polarised atoms along the path of travel of the charged particle interfere constructively to produce a coherent wavefront with an angle given by the Cherenkov angle

$$\cos\theta_{Ch} = \frac{1}{\beta n}. \tag{3.2}$$

This is shown in Fig. 3.1 [74].

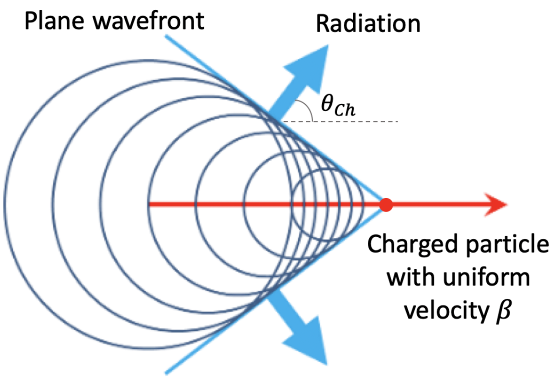

Figure 3.1: Schematic of the generation of Cherenkov radiation from a charged particle moving uniformly with velocity β [74].

3.3 Cherenkov diffraction radiation and the polarisation current approach

The generation of Cherenkov diffraction radiation differs from ChR because the charged particle does not need to propagate through the dielectric medium but only in close proximity to it. For illustration, Fig. 3.2 shows an electron moving with constant velocity β and with energy γ parallel to a triangular dielectric target, also known as a radiator, with refractive index n and with the exit face angled at ϕ with respect to the direction of particle travel. The distance between the direction of travel of the electron and the target is called the impact parameter b. As the particle passes near to the medium, the atoms on the surface are polarised. The polarization radiation field emitted by this interaction, called Cherenkov diffraction radiation, propagates through the medium at the Cherenkov angle θ_{Ch}, Eq. 3.2.

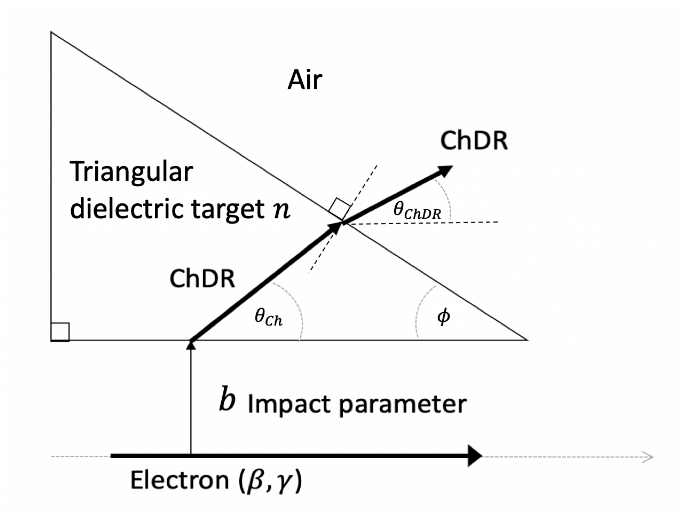

Figure 3.2: Schematic of the generation of Cherenkov diffraction radiation from a charged particle moving uniformly with velocity β and with energy γ parallel to the bottom face of a triangular dielectric target with refractive index n. The ChDR is generated and propagates inside the target at θ_{Ch} and exits the target at θ_{ChDR}.

The ChDR exits the target at an angle θ_{ChDR} given by Snell's law. The amount of radiated power from the dielectric depends on the magnitude of the intercepted EM field. Hence, the radiated power depends on the intensity and energy of the charged particle, and the distance between the charged particle and the surface of the dielectric that is exposed to the particle field. From Section 2.2, by taking a 2+2 symmetric arrangement of targets and measuring the power of ChDR exiting the targets, a transverse beam position measurement can be realised. A simple evaluation of the feasibility of the use of ChDR for application as a BPM at AWAKE can be shown by the effective electric field radius r_E in the so-called pre-wave zone of a charged particle moving with relativistic velocity where the impact parameter should fulfil the condition [65] [75]

$$b \leq r_E = \gamma\lambda/2\pi, \tag{3.3}$$

where γ is the relativistic Lorentz factor and λ is the wavelength. By taking $\gamma = 37$, which corresponds to a particle energy of $19\,\mathrm{MeV}$, and $\lambda = 10\,\mathrm{mm}$, for a detection frequency of $30\,\mathrm{GHz}$ as an example, $r_E = 60\,\mathrm{mm}$ which is greater than $h = 30\,\mathrm{mm}$ for a centred beam in the AWAKE vacuum beam-pipe. Therefore, the condition, Eq. 3.3, is satisfied.

Several theoretical models exist [65] [69] for describing the characteristics of the ChDR emitted from dielectric targets, and was studied and compared to experimental data in detail in [76]. One of the models predicts an exponential dependence of the emitted ChDR on the impact parameter in the form of [65] [77]

$$\sim \exp(-4\pi h/\beta\gamma\lambda). \tag{3.4}$$

This dependence was shown experimentally for measurements of the incoherent region of the ChDR spectrum [78] but the parameters in the exponent did not agree with measurements of the coherent part of the ChDR spectrum in both [59] and [76].

An alternative theory based on the polarisation current model of the generation of PR from a charged particle passing close to a number of different target geometries was developed in [69], [79], [80], and analytically described by the PCA. As an example, the theory of ChDR based on the PCA for a charged particle passing close to a triangular dielectric prism target which was formalised by Shevelev and Konkov (2014) [69] will be analyzed in the following.

As previously mentioned, ChDR is a type of polarization radiation that is generated by atoms in a medium through the interaction of the field of a charged particle of energy γ that is moving with constant velocity $v = \beta c$ in close proximity to the surface of the medium. The polarisation current density is defined as [69]

$$\boldsymbol{j}_{pol} = \sigma(\omega) \left[\boldsymbol{E}^0 + \boldsymbol{E}^{pol}(\boldsymbol{j}_{pol})\right], \tag{3.5}$$

where $\boldsymbol{E}^0 \equiv \boldsymbol{E}^0(\boldsymbol{r}, \omega)$ and $\boldsymbol{E}^{pol} \equiv \boldsymbol{E}^{pol}(\boldsymbol{r}, \omega)$ are the Fourier transforms of the particle beam field in vacuum and the field of the polarisation currents in the medium respectively, and ω is the angular frequency. The conductivity of the dielectric medium $\sigma(\omega)$ is given by

$$\underbrace{\sigma(\omega) = i\omega\left[\varepsilon_0 - \varepsilon(\omega)\right]}_{\text{SI units (mks)}} \quad \equiv \quad \underbrace{\sigma(\omega) = \frac{i\omega}{4\pi}\left[1 - \varepsilon(\omega)\right],}_{\text{Gaussian units (cgs)}} \tag{3.6}$$

where $\varepsilon \equiv \varepsilon(\omega)$ is the permittivity of the dielectric material and ε_0 is the permittivity of free space. The right-hand-side of Eq. 3.6, and all other equations in this paragraph are in Gaussian (cgs) units[1], as developed in [69]. The magnetic field

[1]Please note: $\varepsilon\ (Gauss) \equiv \varepsilon/\varepsilon_0 \simeq \varepsilon_r$ (SI)

of PR in the medium $\boldsymbol{H}^{pol}$ can be obtained from Maxwell's equations

$$\left(\nabla^2 + \varepsilon(\omega)\frac{\omega^2}{c^2}\right)\boldsymbol{H}^{pol}(\boldsymbol{r},\omega) = -\frac{4\pi}{c}\sigma(\omega)\nabla\times\boldsymbol{E}^0(\boldsymbol{r},\omega). \tag{3.7}$$

A solution for $\boldsymbol{H}^{pol}$ in Eq. 3.7 is found by integrating the induced currents in the finite volume V_T

$$\boldsymbol{H}^{pol}(\boldsymbol{r},\omega) = \nabla\times\frac{1}{c}\int_{V_T}\sigma(\omega)\boldsymbol{E}^0(\boldsymbol{r'},\omega)\times\frac{\exp\left\{i\sqrt{\varepsilon(\omega)}|\boldsymbol{r'}-\boldsymbol{r}|\omega/c\right\}}{|\boldsymbol{r'}-\boldsymbol{r}|}d^3r'. \tag{3.8}$$

This describes all PR generated in a finite target with arbitrary shape. The spectral-angular distribution of PR can then be calculated by

$$\frac{d^2W}{d\omega d\Omega} = \frac{cr^2}{|\varepsilon|^2}|\boldsymbol{H}^{pol}|^2, \tag{3.9}$$

where W is the radiated power and Ω is the solid angle.

A triangular prism target of finite size in y and z, and infinite size in x is now considered. A schematic of the target is shown in Fig. 3.3 where the vertices ABC represent a so-called single target and ABD forms a double target. An electron is travelling with uniform velocity $\boldsymbol{v}$ parallel to and at a distance b from AB. The dielectric target has dimensions defined by a and ϕ, where a is the triangle height i.e. the distance between B and C. The z-axis is perpendicular to the exit face of the target which is AC or AD for a single or double target respectively. The angle of flight of the particle, which is the angle between the z-axis and the direction of particle beam travel, is α. The polar and azimuthal angles are θ and φ respectively. By integrating Eq. 3.8 over the volume shown in Fig. 3.3 and substituting into Eq. 3.9, the spectral-angular distribution of PR for a single and double triangular

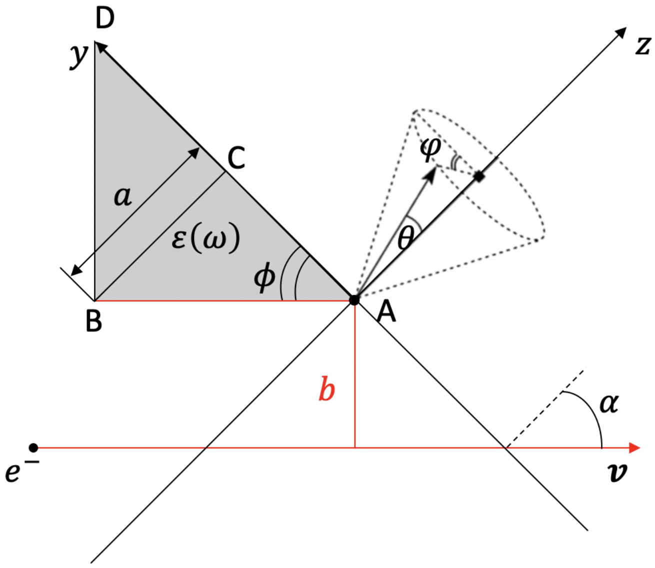

Figure 3.3: Schematic of an electron moving with uniform velocity $\boldsymbol{v}$ parallel to and at a distance b from the bottom face of a triangular prism target. The triangle ABC represents a single target and ABD represents a double target. The permittivity of the dielectric target is ε and the angle of flight of the particle, which is the angle between the z-axis (perpendicular to the exit face of the target) and the direction of particle beam travel, is α. The x-axis is going into the page. Image adapted from [69].

target can be obtained. For a single target, this is given by [69]

$$\frac{d^2W}{d\omega d\Omega} = \frac{e^2\beta^2}{4\pi^2 c}\frac{\cos^2(\theta'-\alpha)}{|P|^2}\left|\frac{\varepsilon-1}{\varepsilon}\right|^2$$
$$\times\left|1-\frac{P\exp\left\{i\frac{\omega}{\beta c}\Sigma a\cot\phi\right\}+\Sigma\cot\phi\exp\left\{-ia\frac{\omega}{\beta c}P\right\}}{P+\Sigma\cot\phi}\right|^2$$
$$\times\left[\left|\frac{\varepsilon}{\varepsilon\cos(\theta'-\alpha)+U}\right|^2|\cos\alpha(\gamma^{-1}\sin(\theta'-\alpha)-iK\cos\varphi U)\right.$$
$$+\sin\alpha(iK\sin(\theta'-\alpha)+\gamma^{-1}U\cos\varphi)-\gamma\beta\sin(\theta'-\alpha)U\sin^2\varphi|^2$$
$$+\left|\frac{\sqrt{\varepsilon}}{\cos(\theta'-\alpha)+U}\right|^2(\gamma\sin\varphi)^2(\sin^2(\theta'-\alpha)+|U|^2)\times$$
$$\left.[1-\beta^2\cos^2(\theta'-\alpha)+2\beta\gamma^{-2}\sin\alpha\sin(\theta'-\alpha)\cos\varphi-\gamma^{-2}\sin^2\alpha(K^2-\gamma^{-2})]\right]$$
$$\times\left[\exp\left\{-2\frac{\omega}{\gamma\beta c}(h+a\cot\phi)K\cos\alpha\right\}\right/$$
$$(K^2(1-\beta^2\cos^2(\theta'-\alpha)+\beta^2\sin^2\alpha[1-\sin^2(\theta'-\alpha)\sin^2\varphi]$$
$$\left.+2\beta\sin\alpha\cos\varphi\sin(\theta'-\alpha)))\right], \quad (3.10)$$

where

$$P = \cos\alpha - \beta\sqrt{\varepsilon-\sin^2(\theta'-\alpha)}, \quad (3.11)$$

$$\Sigma = \sin\alpha + \beta\cos\varphi\sin(\theta'-\alpha) - i\gamma^{-1}K\cos\alpha, \quad (3.12)$$

$$K = \sqrt{1+(\gamma\beta\sin(\theta'-\alpha)\sin\varphi)^2}, \quad (3.13)$$

$$U = \sqrt{\varepsilon-\sin^2(\theta'-\alpha)}. \quad (3.14)$$

The relation $\theta = \theta' - \alpha$ has been used to transform to the system of observation of the path of travel of the electron and $h = b/\cos\alpha$. For a double target, the spectral-angular distribution of PR is given by

$$
\begin{aligned}
\frac{d^2W}{d\omega d\Omega} &= \frac{e^2\beta^2}{4\pi^2 c}\frac{\cos^2(\theta'-\alpha)}{|P|^2}\left|\frac{\varepsilon-1}{\varepsilon}\right|^2 \\
&\times\Bigg|1-\exp\Big\{-ia\frac{\omega}{\beta c}(P+\Sigma\cot\phi)\Big\}-\frac{P\exp\Big\{ia\frac{\omega}{\beta c}\Sigma\cot\phi\Big\}}{P+\Sigma\cot\phi} \\
&+\frac{P^2+\Sigma^2\cot^2\phi}{P^2-\Sigma^2\cot^2\phi}\exp\Big\{-ia\frac{\omega}{\beta c}P\Big\}-\frac{\Sigma\cot\phi\exp\Big\{-ia\frac{\omega}{\beta c}\Sigma\cot\phi\Big\}}{P-\Sigma\cot\phi}\Bigg|^2 \\
&\times\Bigg[\left|\frac{\varepsilon}{\varepsilon\cos(\theta'-\alpha)+U}\right|^2 |\cos\alpha(\gamma^{-1}\sin(\theta'-\alpha)-iK\cos\varphi U) \\
&+\sin\alpha(iK\sin(\theta'-\alpha)+\gamma^{-1}U\cos\varphi)-\gamma\beta\sin(\theta'-\alpha)U\sin^2\varphi|^2 \\
&+\left|\frac{\sqrt{\varepsilon}}{\cos(\theta'-\alpha)+U}\right|^2(\gamma\sin\varphi)^2(\sin^2(\theta'-\alpha)+|U|^2)\times \\
&[1-\beta^2\cos^2(\theta'-\alpha)+2\beta\gamma^{-2}\sin\alpha\sin(\theta'-\alpha)\cos\varphi-\gamma^{-2}\sin^2\alpha(K^2-\gamma^{-2})]\Bigg] \\
&\times\Bigg[\exp\Big\{-2\frac{\omega}{\gamma\beta c}(h+a\cot\phi)K\cos\alpha\Big\}\Big/ \\
&(K^2(1-\beta^2\cos^2(\theta'-\alpha)+\beta^2\sin^2\alpha[1-\sin^2(\theta'-\alpha)\sin^2\varphi] \\
&+2\beta\sin\alpha\cos\varphi\sin(\theta'-\alpha)))\Bigg]. \quad (3.15)
\end{aligned}
$$

To illustrate the differences between the PR produced by a single and double target for a charged particle moving in close proximity to the target, Equations 3.10 and 3.15 were plotted for $\gamma = 12$, $\sqrt{\varepsilon} = 1.41$, $b = 15$ mm, $\phi = \pi/4$, $a = 45$ mm and $\lambda = 4$ mm, where $n = \sqrt{\varepsilon}$ is the target material refractive index. These values allow a direct comparison of the results obtained from plotting Equations 3.10 and 3.15 using Mathematica [81] to the results published in [69]. Figures 3.4a and 3.4b visualize Equations 3.10 and 3.15 for the two targets, shown as parametric plots $d^2W/d\omega d\Omega = f(\varphi, \theta)$. To better understand the differ-

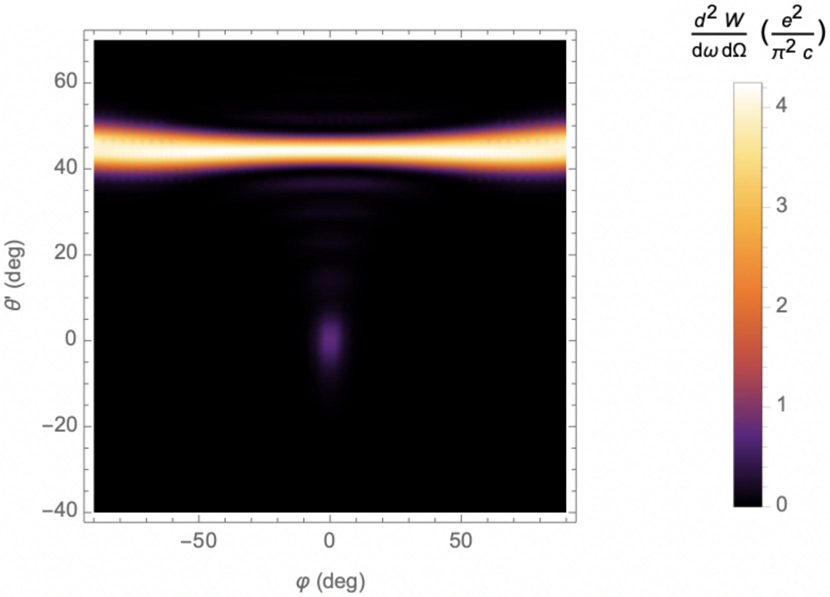

(a)

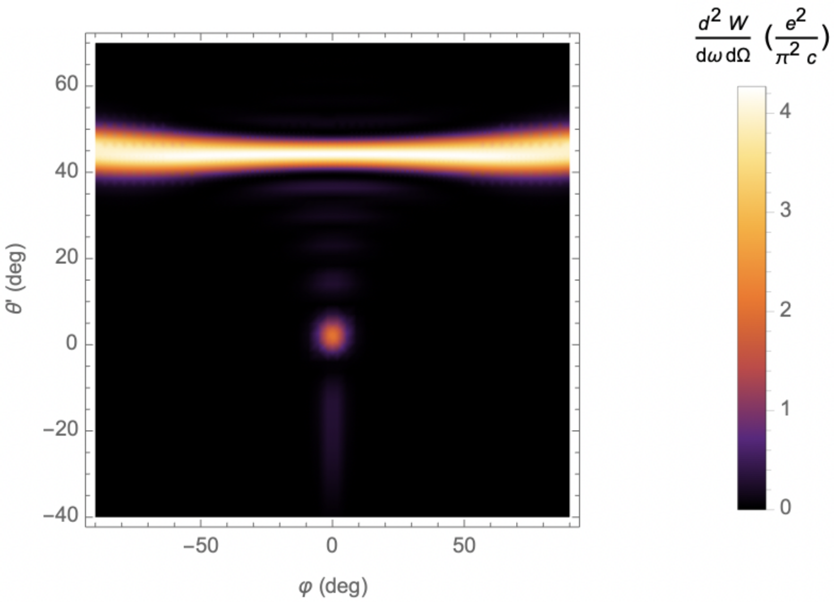

(b)

Figure 3.4: Contour plot of the spectral-angular distribution of PR exiting a (a) single and (b) double triangular prism target from Equations 3.10 and 3.15 respectively, plotted as a function of φ and $\theta' = \theta + \alpha$. The azimuthal angle is φ, θ is the polar angle and α is the angle between the z-axis and direction of particle beam travel shown in Fig. 3.3.

ent types of PR generated by the targets, a slice of the contour plots was taken at $\varphi = 0°$ and is shown in Fig. 3.5. The angle of the ChDR peak θ_{ChDR} is $44.2°$. The radiation peaks at smaller angles are due to DR generated along the face BD and BC for a double and single triangular prism target respectively. As can be seen from Fig. 3.5, the ChDR peak remains the same in magnitude and shape for both cases but more DR is generated in the case of the double triangular prism target. This explains that ChDR depends only on the face area of the target parallel to the direction of travel of the charged particle and not on the volume of the target for

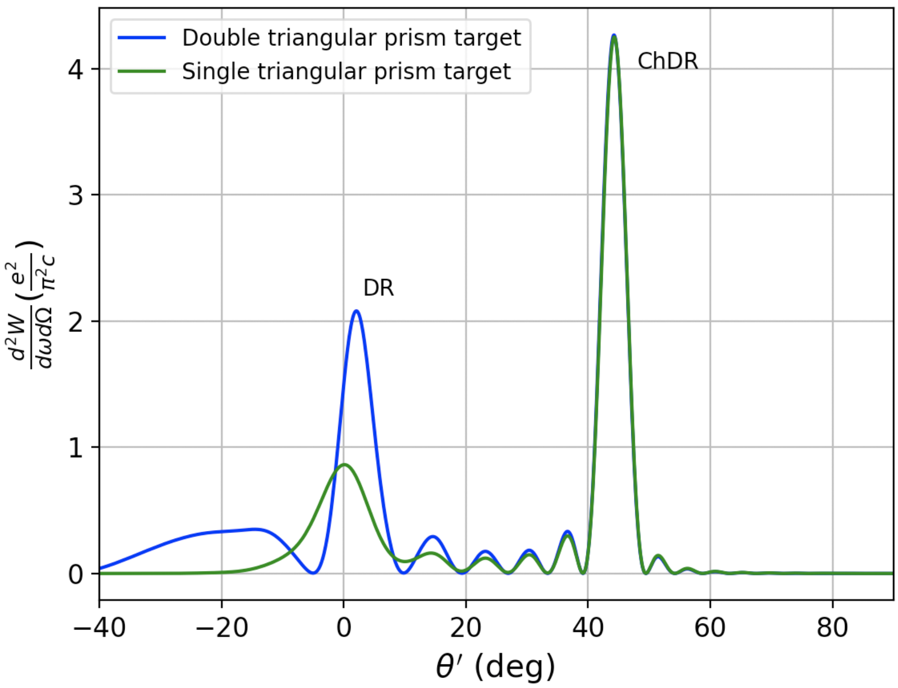

Figure 3.5: Plot of the spectral-angular distribution of PR for a point charge of energy $\gamma = 12$ from a single and double triangular prism target as a function of $\theta' = \theta + \alpha$ for $\varphi = 0°$ from Equations 3.10 and 3.15 respectively [69]. The polar angle is θ and α is the angle between the z-axis and direction of particle beam travel shown in Fig. 3.3. The parameters used for this plot are $\sqrt{\varepsilon} = 1.41$, $b = 15\,\mathrm{mm}$, $\phi = \pi/4$, $a = 45\,\mathrm{mm}$ and wavelength $\lambda = 4\,\mathrm{mm}$. The ChDR peak exits both targets at $\theta' = \theta_{ChDR} = 44.2°$. DR peaks can be observed for both the double and single triangular prism targets at smaller θ' values.

the same ε and ϕ. Fig. 3.5 agrees with the findings in [69]. Therefore, it verifies the PCA script developed in Mathematica for investigating the generation of PR from a triangular prism target.

Although the theory is useful for understanding how the PR changes with different target parameters, it becomes more challenging to solve the equations of the PCA model for more complex geometries. Since the target design needs to be tailored to its application, it is more efficient to use a numerical solver to investigate different target geometries. This will be discussed in detail in the following sections.

3.4 Numerical analysis of Cherenkov diffraction radiation

3.4.1 Comparison between the Wakefield and Particle in Cell solver

In order to benchmark the theory as described by the PCA with numerical simulations in view of analysing more complex geometries, a model was set up using the Computer Simulation Technology (CST) Studio Suite software [82]. This software allows the numerical analysis of Maxwell's equations for arbitrary geometries using a variety of solvers. Since charged particles needed to be included in the numerical analysis, the two solvers of interest were the Wakefield and the particle-in-cell (PIC) solver, both operating in discrete, equidistant time steps.

In the Wakefield solver, the excitation signal is introduced into the calculation domain via a transmission line as a line charge density distribution. The EM field of the signal is equal to that of a charged particle bunch with given charge and longitudinal particle distribution, usually Gaussian, defined by the user. There are no particle/field interactions in the case of the Wakefield solver.

In the PIC solver, a particle bunch is modelled as a set of macroparticles each with a charge, position and momentum, and is produced by a user-defined source located in the calculation domain. It is a self-consistent method for particle tracking and the scheme by which the EM fields, and particle positions and momenta are updated for each time step Δt is shown in Fig. 3.6. Since the PIC solver involves particle/field interactions, it is a useful solver for when the dynamics of the particle beam need to be studied.

For both solvers, a calculation domain has to be defined by boundary conditions, which then is divided into smaller elements, known as mesh cells, and solved numerically using the discretised integral form of Maxwell's equations.

In the case of the Wakefield solver, the beam field distribution follows that of an indefinite long line charge, and beam bunches of e.g. $\beta = v/c \approx 1$ produces a TEM field for the entire calculation domain. On the other hand, the PIC solver calculates the beam field distribution exactly as given by the geometric structure of the emitting source, and the EM field of a macro-particle, even with relativistic

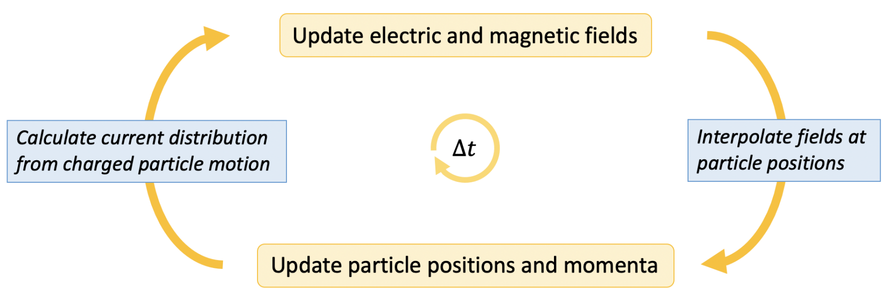

Figure 3.6: Flow-diagram of how the PIC solver in CST updates the EM fields, and particle positions and momenta per time step Δt [82].

velocity ($\beta \approx 1$), is non-TEM in close proximity to the emitting surface, but becomes more TEM-like as it travels further away. This can be seen by the electric field distribution from a Gaussian beam bunch with $1\,\mathrm{ps}$ (1σ) length and $10\,\mathrm{nC}$ charge travelling in the positive z direction in Fig. 3.7. The fields are shown by their absolute values:

$$E_{abs} = \sqrt{E_x^2 + E_y^2 + E_z^2}, \tag{3.16}$$

where the Cartesian components of the field are $E_{x,y,z}$. The calculation region for both solvers is indicated by the blue background, which is vacuum. Both calculation domains have the same "thickness" in the x-direction of $5\,\mathrm{mm}$. For the Wakefield solver, all boundaries are open space, apart from x_{max} and x_{min} which have electric boundaries i.e. the transverse component of the electric field $E_t = 0$. All boundaries in the PIC solver are open space. In the Wakefield solver, the beam field enters the simulation domain with a TEM-like field. Whereas in the PIC solver, the EM-field of the particle bunch starts as non-TEM field, given by

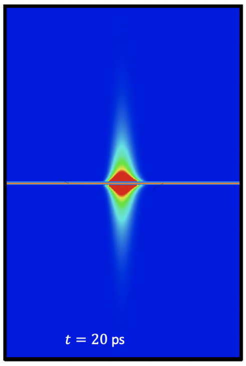

(a) Wakefield solver.

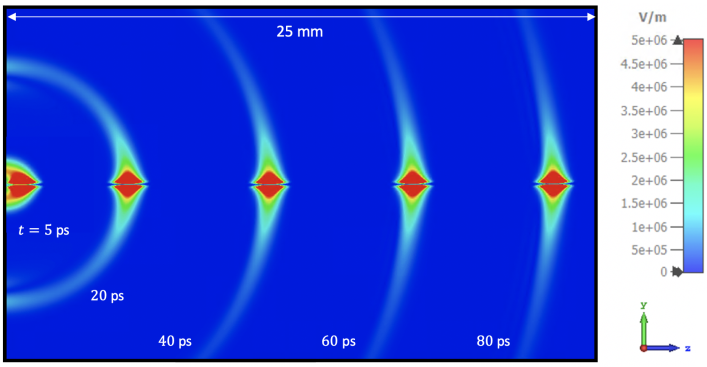

(b) PIC solver.

Figure 3.7: Time evolution of the absolute electric field shown as a contour plot in the Wakefield and PIC solver for a particle bunch with $1\,\mathrm{ps}$ one-sigma longitudinal bunch length and $10\,\mathrm{nC}$ bunch charge. The particle bunch is travelling in the positive z direction. The simulation domain in both solvers is indicated by the bounding black box and the blue background represents vacuum.

the conditions of the moving bunch charges emitted by the particle source located in the xy-plane which in this case is a point source. Therefore, one has to include some extra distance between the particle source and the area of interest in order for the beam field to develop into a TEM-like field, which increases the computation time. A disadvantage of the Wakefield solver is that at least one electric boundary has to be defined or a Perfect Electrical Conducting (PEC) area has to be included across at least one plane. Electric boundaries can create misleading results for the farfield monitors, which are used, e.g. to provide the time-averaged magnitude of the Poynting vector. If open boundaries are required in all directions, then the PIC solver is the better option.

3.4.2 Comparison between theoretical and numerical analysis

To benchmark the theoretical model of PR as described by the PCA and the numerical simulations in CST Studio, the triangular prism target detailed in Section 3.3 was modelled in both the PIC and the Wakefield solver. The modelled geometry in the PIC solver is shown in Fig. 3.8, with the beam source and direction indicated by the red arrow. The beam is simulated with a perfect Gaussian longitudinal and transverse particle distribution with $4\,\mathrm{ps}$ RMS bunch length, $600\,\mathrm{pC}$ bunch charge and $0.3\,\mathrm{mm}$ transverse size. The far-field monitor is shown by the blue box at the exit face of the dielectric. To better isolate the pure ChDR and reduce the relative amount of DR generated, a metal shielding was included in the y and z directions as shown by the grey structures. The grey structures are modelled as PEC. The PEC sheet in the y direction was placed perpendicular to the trajectory of the charged particle beam in order to reduce the reflections of the non-TEM field of the particle beam before the triangular target in order to improve the accuracy of the simulation for comparison with the analytical model. All boundaries are open space. The bandwidth of the simulation is $100\,\mathrm{GHz}$ and the mesh size

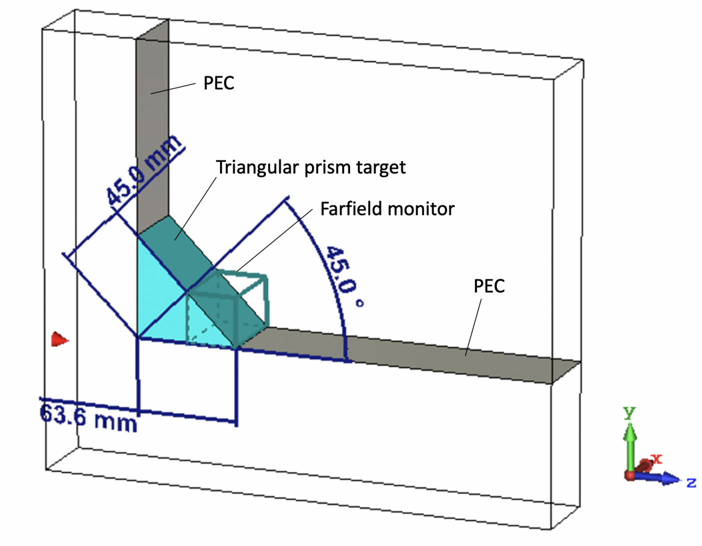

Figure 3.8: Modelled geometry of a double triangular prism target in CST Studio PIC solver.

is determined by setting the number of mesh cells per wavelength to 10. This is the recommended mesh cell size as a trade-off between simulation accuracy and computation time. With these settings, there are approximately 280 million mesh cells for this simulation. The same model was created in the Wakefield solver, Fig. 3.9, with the only difference being the placement of the first PEC sheet parallel to the beam direction and the boundary condition at y_{min} being electrical. The particle beam is represented by a line charge, indicated by the blue arrows, and therefore has no user-definable transverse beam dimensions. The orange arrows indicate an integration path in case the wakefield needs to be calculated, here left at the default to the same trajectory as the beam. The number of mesh cells for this simulation is 91 million due to the reduced simulation domain compared to the case of the PIC solver.

The normalised far-field results for the azimuthal angle $\varphi = 0°$ are shown by the red and black traces in Fig. 3.10 along with the analytical result from the PCA

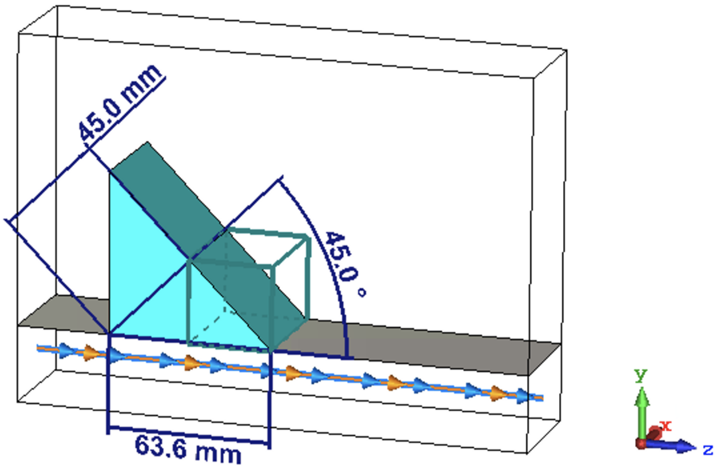

Figure 3.9: Modelled geometry of a double triangular prism target in CST Studio Wakefield solver.

model for comparison of the angles of the radiation peaks. The key features of the ChDR as predicted by theory, such as the peak angle and width, are also present in the spectral-angular distribution result of CST. For the result from the PIC solver (red trace), the ChDR peak is $\theta_{ChDR} = 45.7°$ and for the Wakefield solver (black trace), $\theta_{ChDR} = 44.2°$ which is the same as theory. Fig. 3.11 shows the time evolution of the beam field and the PR from the PIC and Wakefield solver. At $t = 0\,\mathrm{ns}$, the beam field is not an exact TEM field in the PIC solver and subtends some angle with the vertical. This angle reduces as the beam travels further away from the source. A larger distance between the source and the structure of interest in the PIC solver would allow for a more TEM-like beam field to develop and reduce the discrepancy between the analytical and numerical θ_{ChDR} values as shown in Fig. 3.10. However, this would increase the simulation volume and computation time. On the other hand, in the Wakefield solver, the beam field is TEM for the entire distance before reaching the target and so θ_{ChDR} between simulation and theory are in agreement. At $t = 0.1\,\mathrm{ns}$ in Fig. 3.11, a circular DR

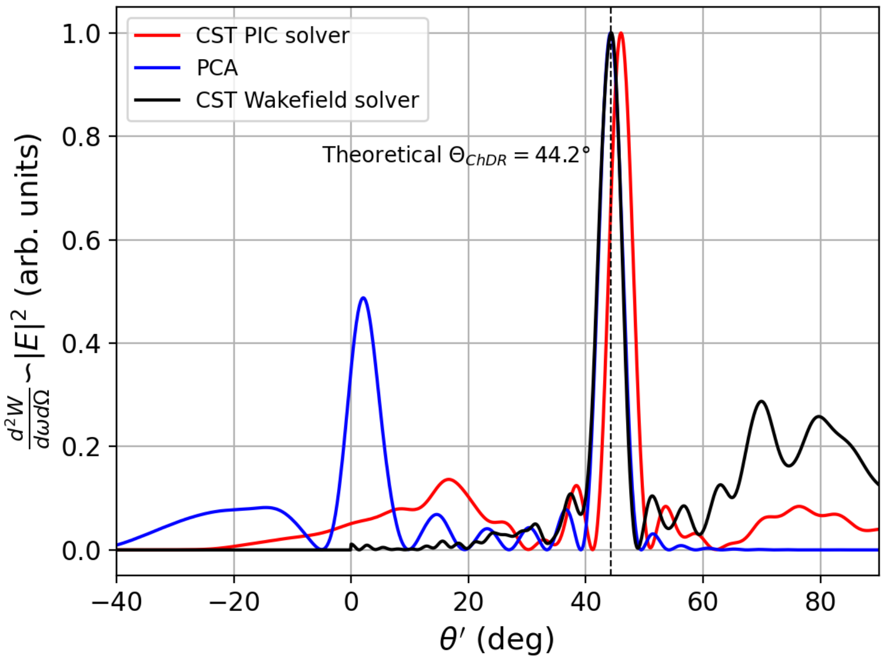

Figure 3.10: Plot of the spectral-angular distribution of PR for an electron beam with energy $\gamma = 12$ as a function of the polar angle θ' for azimuthal angle $\varphi = 0°$ from the analytical PCA and numerical simulations in CST. The parameters used for this plot are $\sqrt{\varepsilon} = 1.41$, $b = 15\,\mathrm{mm}$, $\phi = \pi/4$, $a = 45\,\mathrm{mm}$ and wavelength $\lambda = 4\,\mathrm{mm}$.

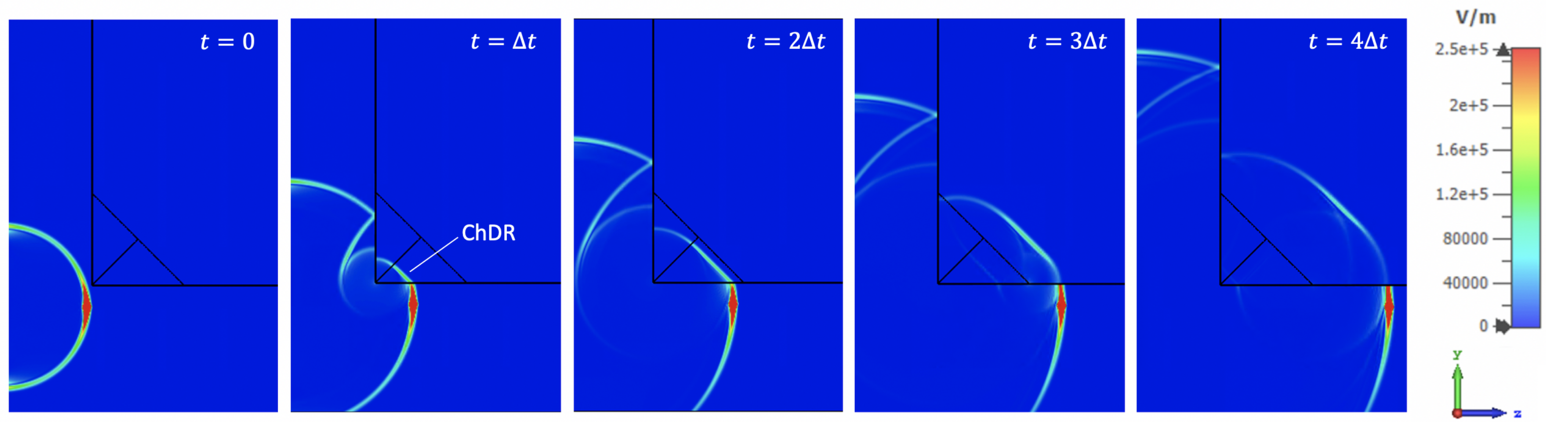

(a)

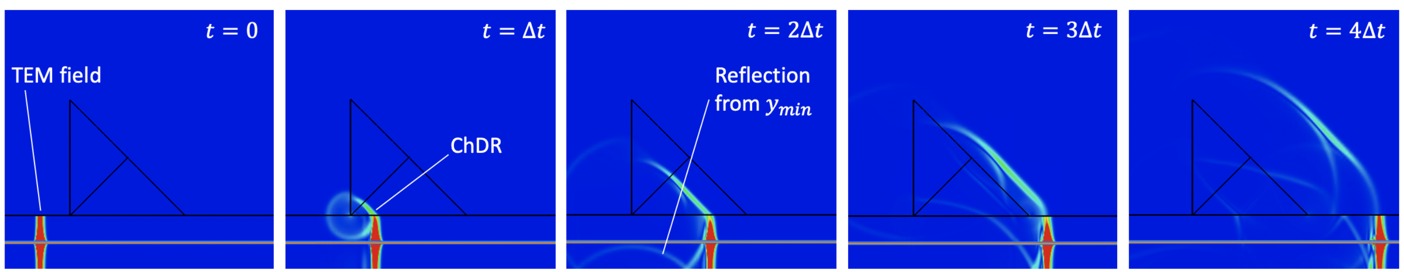

(b)

Figure 3.11: Contour plot of the modulus of the E-field at different times t in the (a) PIC solver and (b) Wakefield solver in CST using the models of the triangular targets in Figures 3.8 and 3.9 respectively. The parameters used are $\sqrt{\varepsilon} = 1.41$, $\phi = \pi/4$, $a = 45\,\mathrm{mm}$, where a particle beam with $\gamma = 12$ is travelling in the positive z direction at a distance $b = 15\,\mathrm{mm}$ from the bottom face of the target. At $t = \Delta t$, where $\Delta t = 0.1\,\mathrm{ns}$, ChDR is generated inside the target as the particle beam passes. The ChDR propagates through the target at the Cherenkov angle.

wavefront is produced from the first edge of the triangular prism in both solvers. As the beam passes the second edge at $t = 0.3\,\mathrm{ns}$, a second circular DR front is produced. Both of these "edge" radiation fronts contribute to the DR appearing on either side of the ChDR peak in Fig. 3.10. However, due to the metal shielding, the DR at around $\theta' = 0°$ is lower than in the analytical PCA result, which does not account for metal shielding. There is also a larger contribution of radiation at larger θ' values in the Wakefield solver compared to the PIC solver due to the field reflections at y_{min} which is an electrical boundary in the case of the Wakefield solver but open space in the PIC solver. Therefore, the PIC solver produces more accurate results in terms of the radiation produced either side of the ChDR peak for the particular geometry studied in the PCA and the Wakefield solver produces a more accurate result of the ChDR peak. When comparing both solvers with the PCA result, two additional reasons for the discrepancy between the spectral-angular distributions of PR are that in the simulations, the geometry is finite in x and the beam has a longitudinal length and bunch charge. Whereas, in theory, the target is modelled as infinite in x and there is only one point charge passing the target.

3.5 Conclusions

This chapter began with a general description of PR. An analytical description of ChDR via the PCA was then presented in Section 3.3. The equations for the spectral-angular distribution of PR were shown for a single and a double triangular prism target, having the same surface area exposed to the beam field in the longitudinal plane. It was shown that, whilst the amount and direction of ChDR emitted by the target remained the same, the amount of DR increased for the double triangular prism target. Hence, this demonstrated one of the key features of

ChDR that it is generated by the surface area exposed to the beam field in the longitudinal direction and not by the target face perpendicular to the direction of particle motion.

A numerical analysis of the targets was then performed with two solvers in CST and described in Section 3.4. The goal was to compare the numerical simulations to the analytical model for ChDR to give confidence that more complex geometries, which in many cases cannot be solved analytically, can be studied with numerical simulations. The two solvers that were used to model the targets were the Wakefield and the PIC solver, since they are the only solvers that can simulate particle-beam fields. It was found that the particle-beam field was modelled more accurately with the Wakefield solver as the beam travelled across the entire simulation domain with a more-TEM like field than in the PIC solver. This was also evident in the angle of ChDR emitted by the target where the angle and shape agreed well with the PCA for the Wakefield solver. Therefore, the Wakefield solver was used to study the ChDR emitted by more complex target geometries and will be presented in detail in the next chapter.

4 A beam position monitor based on Cherenkov diffraction radiation

4.1 Design of the ChDR BPM using numerical modelling

4.1.1 Target shape

Since complex geometries are almost impossible to be analysed using the PCA model, and the key features of ChDR generated in simple target geometries show a good agreement between numerical simulation and analytical theory as demonstrated with the triangular prism target in Section 3.4.2, more complex geometries were studied further using the CST Studio software for the design of a ChDR BPM.

First, to understand whether the ChDR peak changes with different target geometries having a similar surface area exposed to the beam field, two additional simulations were carried out in CST PIC solver. These are shown in Fig. 4.1 with the original double triangular prism target in the top inset for comparison. All targets have $\sqrt{\varepsilon_r} = 1.41$. The beam parameters are the same as those used in the simulation described in Section 3.4.2. Fig. 4.2 shows the corresponding spectral-angular distributions for $\varphi = 0°$. The ChDR peak around $\theta' = 44°$ remains similar in magnitude and shape for all three geometries. This is in accordance with the

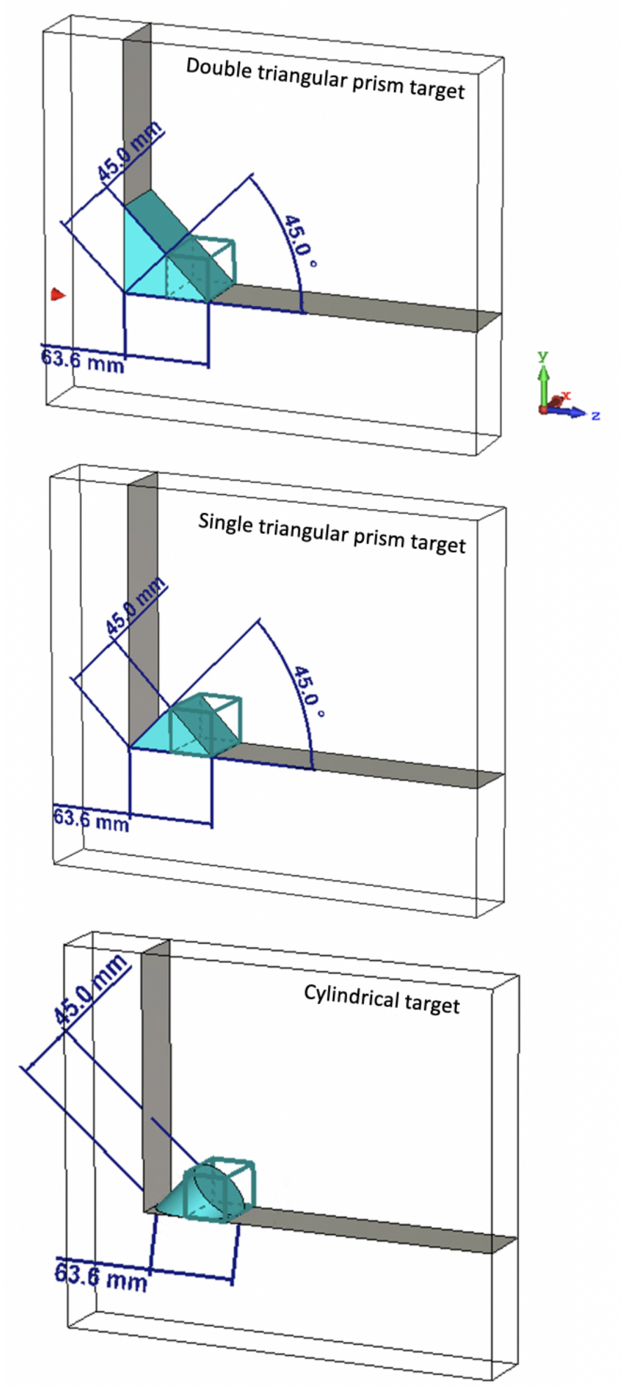

Figure 4.1: Models in CST Studio of different target geometries with $\sqrt{\varepsilon_r} = 1.41$, $b = 15\,\mathrm{mm}$, $\phi = \pi/4$ and $a = 45\,\mathrm{mm}$.

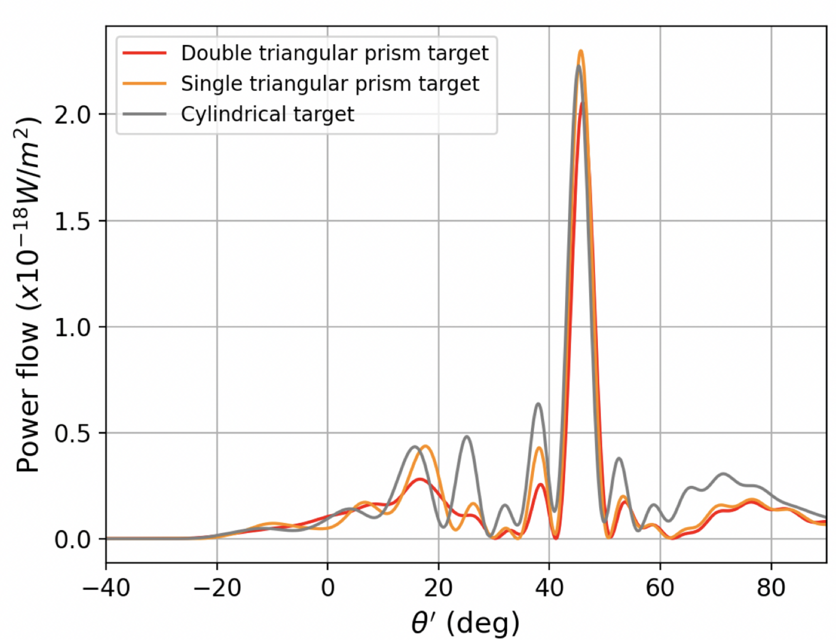

Figure 4.2: Plot of the power flow of PR exiting a single and double triangular prism target, and a cylindrical target versus the polar angle θ' for azimuthal angle $\varphi = 0°$ using the CST models in Fig. 4.1. The parameters used for this plot are $\sqrt{\varepsilon_r} = 1.41$, $b = 15\,\text{mm}$, $\phi = \pi/4$, $a = 45\,\text{mm}$ and wavelength $\lambda = 4\,\text{mm}$.

PCA as the ChDR is only generated by the face that is exposed to the beam field [69]. The main difference is the amount of DR generated, which increases for the cylindrical target seen at θ' values above and below the ChDR peak. Since the ChDR that is generated does not change significantly between the different target geometries, a cylindrical target design was chosen to be further studied as this geometry was the easiest to be manufactured, including the metallization of the sheath, with a view to being realized as a vacuum-compatible BPM pick-up.

4.1.2 Design requirements

The design of the ChDR targets needed to take several practical requirements and boundaries at AWAKE into consideration. First, it was foreseen that two BPMs based on ChDR would be installed in the common beam line before the plasma cell [59]. Fig. 4.3 shows the proposed beam line modifications and the relative distances of the ChDR BPMs from the plasma cell entrance. Given the limited space available and the reduced manufacturing time, it was proposed to "convert" two proton BPMs (pBPM), one of which was already installed in the common beam line, located approximately $0.96\,\mathrm{m}$ from the entrance of the plasma cell, and another spare, into ChDR BPMs. The spare pBPM body was proposed to be installed in a drift section at around $3.60\,\mathrm{m}$ upstream of the plasma cell entrance. These modifications had to have as little impact as possible on the other existing elements in the beam line.

The use of existing pBPM bodies meant that the design of the targets had to respect the geometry of the pBPM bodies. From previous numerical computations [59], the angle of the target with respect to the direction of propagation of the beam was studied. The two angles that were simulated were the Cherenkov angle θ_{Ch} and $90°$. Whilst the second case is less challenging to manufacture and suffers less spatial constraints imposed by the pBPM body, it was observed from simulations that the PR propagating through the target experienced more internal reflections than when the target was angled at θ_{Ch}. Therefore, a more complex development of the PR inside the target was observed. Furthermore, when the target is at $90°$, the PR, upon exiting the target, travels mainly parallel to the beam direction. Whereas, when the target is angled at θ_{Ch}, the majority of the PR power exiting the target is at the well-defined Cherenkov angle. This makes the PR more efficient to capture via e.g. a horn antenna compared to when the target is angled at $90°$. Although in both cases the beam position sensitivity derived numerically was the same, for the reasons stated above, a target angled at θ_{Ch} was chosen.

As mentioned in Section 2.4, the key requirement of the ChDR BPM is to cut off the proton signal which dominates at frequencies below a few GHz assuming

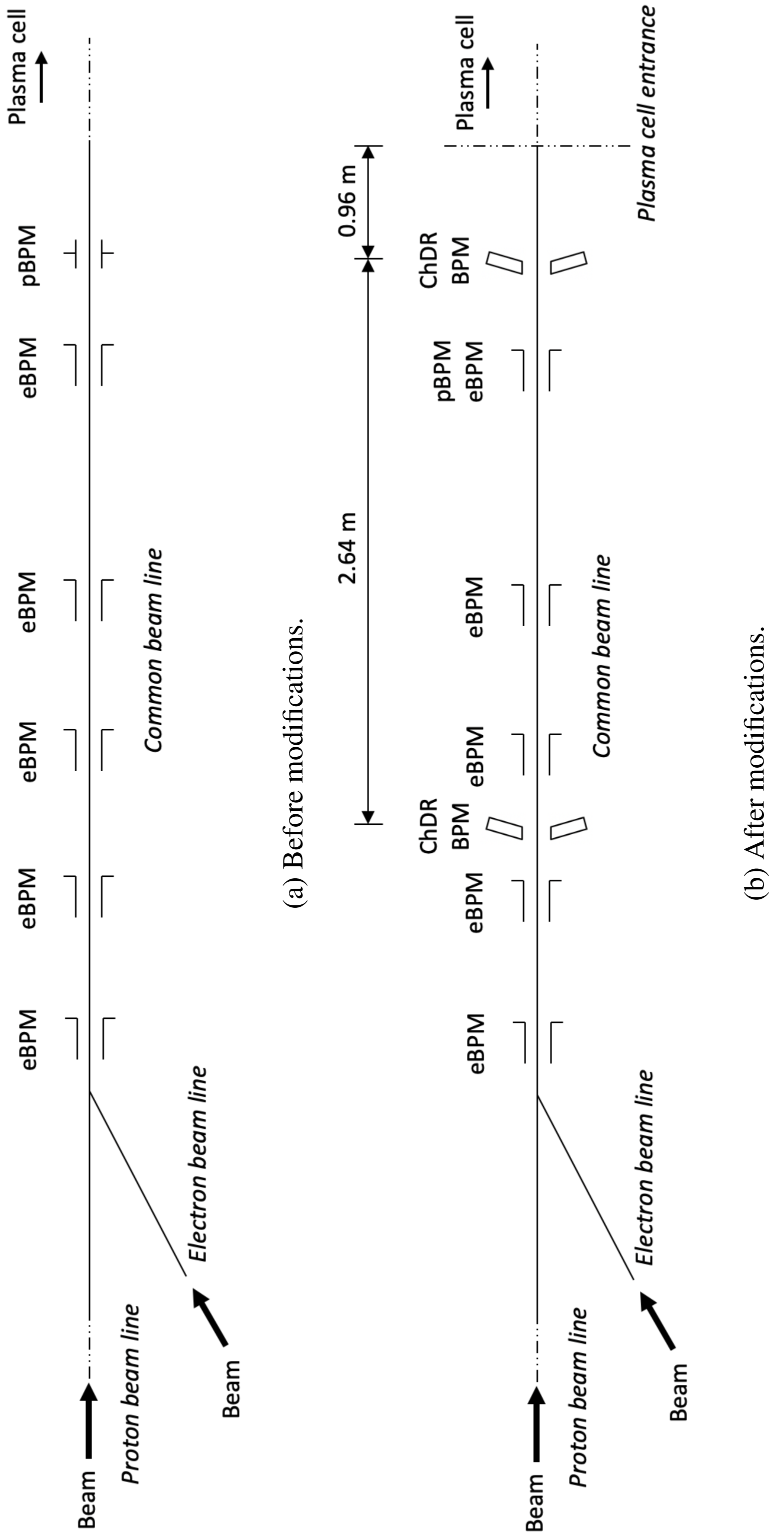

(a) Before modifications.

(b) After modifications.

Figure 4.3: Schematic of the AWAKE beam line modifications with the conversion of an existing pBPM into a ChDR BPM and installation of an additional ChDR BPM.

perfect Gaussian longitudinal particle distributions for the beam parameters at AWAKE. Therefore, the targets, which are essentially dielectric-loaded circular waveguides with the lowest cut-off frequency of the dominant transverse electric mode given by [83]

$$f_{TE11} = \frac{p'_{11}}{\pi d\sqrt{\epsilon\mu}} \cong \frac{1.8412c}{\pi d\sqrt{\varepsilon_r}}, \tag{4.1}$$

where d is the target diameter and $p'_{11} \cong 1.8412$ the 1st root of the derivative of the Bessel function of second kind J'_1, had to provide an appropriate level of high-pass filtering. The cut-off frequencies for $d = 6\,\mathrm{mm}$ and Cherenkov angles for three different dielectric materials are shown in Table 4.1. A material with a lower relative permittivity ε_r results in a higher cut-off frequency which is advantageous in isolating the electron beam signal. However, this means a smaller Cherenkov angle which may not be compatible with the geometry of the pBPM. The mechanical design of the pBPM will be presented and discussed in Section 5.1.

Table 4.1: The relative dielectric permittivity, cut-off frequency of the dominant mode of a dielectric-loaded circular waveguide with $d = 6\,\mathrm{mm}$, and Cherenkov angle of different dielectric materials.

Material	ε_r	f_{TE11}/GHz	θ_{Ch}
Alumina	9.9	9.3	71°
Fused silica	3.75	15.1	59°
PTFE	2.1	20.2	46°

Previously, a BPM based on $18\,\mathrm{mm}$ diameter, cylindrical PTFE targets was tested in-air [59] at CLEAR [58]. Whilst this test showed that the signals extracted from the ChDR targets were sensitive to the beam position, this dielectric material cannot be used in an operational BPM due to its fast radiation degradation and vacuum outgassing incompatibility.

By considering all of the above factors, alumina was chosen as the target material for the AWAKE ChDR BPM. The exact dimensions of the targets were investigated numerically in CST, and will be discussed in the following sections.

4.1.3 2D simulation

The simulation campaign in CST Studio for the design of the AWAKE ChDR BPM cylindrical targets first began with a “quasi” 2D model using the Wakefield solver i.e. the y transverse coordinate was set to a very small dimension wrt. the other coordinates. This is the simplest case and can provide a qualitative picture of the propagation of ChDR inside and outside the dielectric target. The Wakefield solver was chosen since the field pattern is most representative of the TEM-field of a relativistic particle beam. In addition, there were no limitations in terms of the boundary conditions as was the case with the PCA and simulation comparison in Section 3.4.2, since PEC is required along an entire plane to model the beam pipe. The model is shown in Fig. 4.4. Here, two alumina targets with a width of $15\,\mathrm{mm}$ (green) are modelled. These are shown inserted inside a PEC structure (grey) which acts as the beam pipe, the blue areas are the beam pipe vacuum and the outside air areas respectively. The alumina targets are positioned at 71° (the Cherenkov angle for alumina) wrt. the direction of travel of the beam, which is shown by the blue and orange arrows in the centre of the simulation domain propagating in the z direction. The bunch charge is $600\,\mathrm{pC}$ and the RMS longitudinal bunch length is $4\,\mathrm{ps}$. All boundaries of the calculation domain are open space, which are indicated by the purple markers at the boundaries, except for the minimum and maximum y boundaries which are magnetic, shown by the blue marker, i.e. the transverse component of the magnetic field is zero $H_t = 0$. Electric and magnetic field probes were placed at distances of $-5\,\mathrm{mm}$ (probe 1), $0\,\mathrm{mm}$ (probe 2) and $5\,\mathrm{mm}$ (probe 3) away from the exit face of the alumina. The cross product of the electric and magnetic field vectors of the radiation measured at the

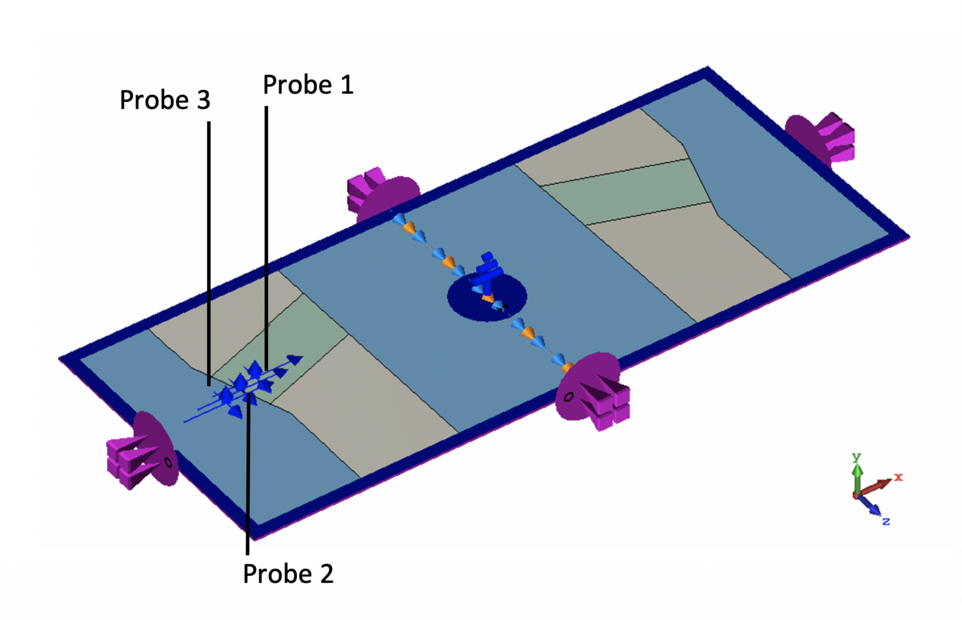

Figure 4.4: "Quasi" 2D model in CST of two $15\,\mathrm{mm}$ wide alumina targets angled at $71°$ wrt. the direction of beam travel (blue and orange arrows).

probes gives the Poynting vector which describes the directional power flow. The field propagation is shown in Fig. 4.5 where a ChDR wave front in the alumina target can be observed, propagating at θ_{Ch}. Two more circular-line wave fronts are also visible at $t = 0.2\,\mathrm{ns}$ behind the beam field. These are from DR of the first and second edge of the alumina. Upon exit of the ChDR radiation, the majority of the radiated power is at θ_{Ch} and some power is reflected back into the alumina ($t = 0.5\,\mathrm{ns}$) due to the mismatch of the wave impedance of the dielectric-loaded waveguide and the free space wave impedance ($\eta_0 \cong 120\pi\,\Omega$). This can also be seen from the field probe measurements shown in Fig. 4.6. The first peak from the probe 1 measurement (blue trace) represents the ChDR generated at the surface of the alumina dielectric. The second peak of the blue trace shows the reflected power from the exit face corresponding to the radiation front inside the alumina at $t = 0.5\,\mathrm{ns}$ in Fig. 4.5. The measurements from probes 2 and 3 shows the power flow of ChDR upon exit and $5\,\mathrm{mm}$ after exiting the alumina. The smaller peaks

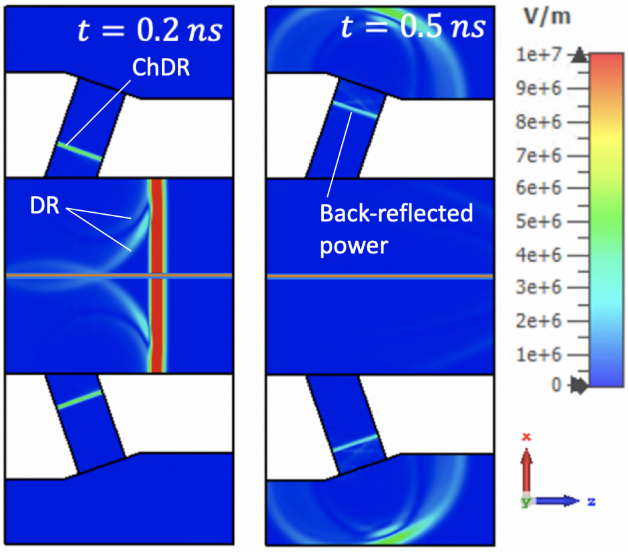

Figure 4.5: Contour plot of the modulus of the E-field for the 2D model shown in Fig. 4.4 at time $t = 0.2\,\mathrm{ns}$ and $t = 0.5\,\mathrm{ns}$. The beam is travelling in the positive z direction.

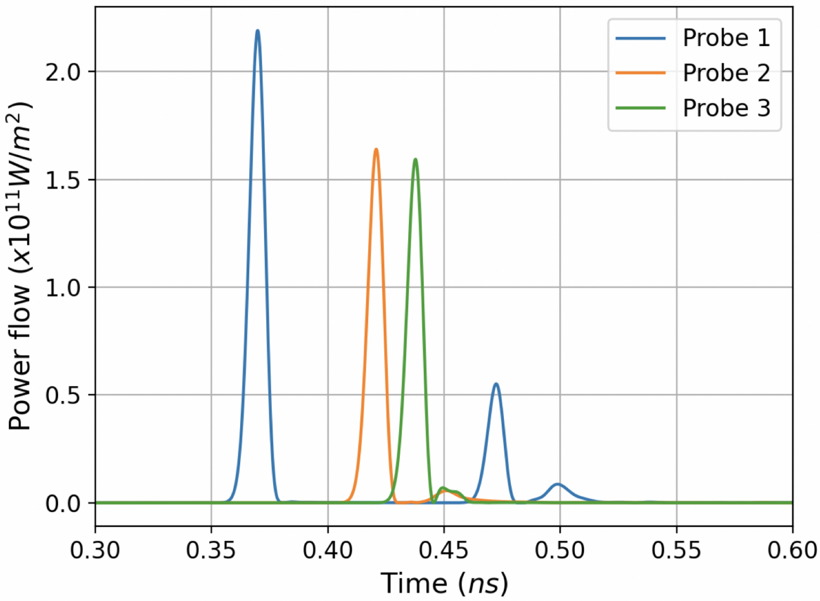

Figure 4.6: Plot of the power flow versus time using probes 1, 2 and 3 indicated in Fig. 4.4 which have distances of $-5\,\mathrm{mm}$, $0\,\mathrm{mm}$ and $5\,\mathrm{mm}$ from the exit face of the alumina respectively.

in all three traces located at $0.45\,\mathrm{ns}$ and $0.50\,\mathrm{ns}$ are due to DR which can be easily distinguished from the ChDR peaks in time.

4.1.4 3D simulation

To improve accuracy and a true representation of the geometric object in the simulations performed with CST Studio, a 3D model was created. In this case, only one ChDR alumina target was modelled to reduce the simulation volume and computation time as shown in Fig. 4.7. Again, the alumina is in green and the vacuum beam pipe with a diameter of $60\,\mathrm{mm}$, which is the same as that in AWAKE, is in blue. The calculation domain has open boundaries in the z direction and electric

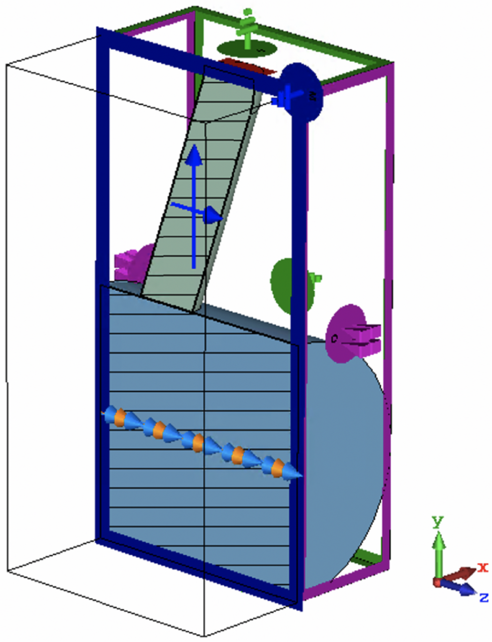

Figure 4.7: The 3D model in CST of a $15\,\mathrm{mm}$ diameter alumina target (green) angled at 71° wrt. the direction of beam travel i.e. the positive z direction. The model is shown as a cut at $x = 0$. The blue volume represents the vacuum beam pipe which has a diameter of $60\,\mathrm{mm}$. The blue crossed arrows located inside the alumina is a probe for measuring the power flow.

boundaries everywhere else. A symmetry plane is also considered shown by the blue magnetic boundary that divides the calculation domain in two. This halves the computation time. A bend had to be included at the end of the target in order to achieve alignment of the exit face of the dielectric with the $zx-$plane so that a waveguide port could be defined which is used to perfectly absorb all power. However, in practice the bend isn't present and the exit face is angled at θ_{Ch}. The $(90^\circ - \theta_{Ch})$-bend, required by CST, should have minimal impact on the results. The background material is PEC. The beam field evolution is shown in Fig. 4.8 and the power flow at the probe (blue crossed arrows in Fig. 4.7) is shown in Fig. 4.9. In the 3D case, DR is generated along the whole cylindrical edge of the target exposed to the beam field. Hence, the relative magnitude of DR to ChDR is much larger than in the 2D case. This can be seen by the first ChDR peak and the second DR peak in Fig. 4.9. The third small peak at $0.46\,\mathrm{ns}$ is due to the internal reflection of the DR which does not propagate at θ_{Ch} inside the alumina

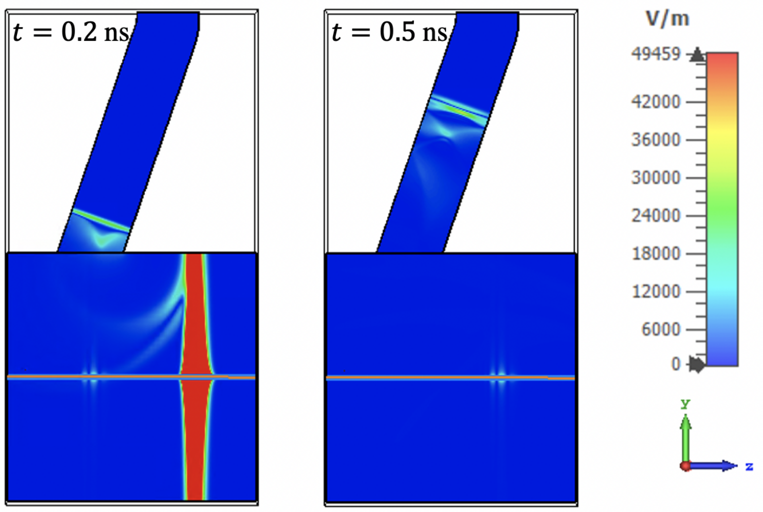

Figure 4.8: Contour plot of the modulus of the E-field for the 3D model shown in Fig. 4.7 at time $t = 0.2\,\mathrm{ns}$ and $t = 0.5\,\mathrm{ns}$ in the yz-plane. The beam is travelling in the positive z direction.

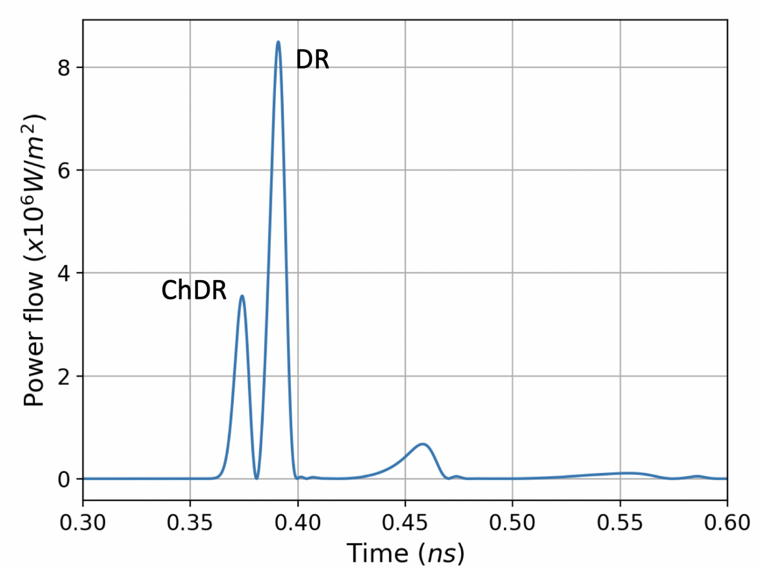

Figure 4.9: Plot of the power flow versus time at the probe indicated by the blue crossed arrows in Fig. 4.7 which is at the same location, relative to the entrance of the alumina, as probe 1 in Fig. 4.4 in Section 4.1.3.

target. These three peaks correspond to the three wave fronts that can be seen to propagate inside the alumina at $t = 0.5\,\mathrm{ns}$ in Fig. 4.8. Some simulation noise is visible along the beam direction in Fig. 4.8 but is so small in magnitude compared to the beam field that it does not significantly impact the results.

4.1.5 Target length

To understand how the radiation changes for different dielectric lengths, probes were placed at distances of $10\,\mathrm{mm}$ along the alumina target for the same model as presented in Section 4.1.4, as illustrated in Fig. 4.10. Fig. 4.11 shows the field evolution and Fig. 4.12 shows the power flow measured at increasing distances from the entrance face of the alumina target. It can be seen that the maximum value of the first peak in each probe measurement, which corresponds to the ChDR, decreases linearly as a function of distance along the dielectric. This can also be

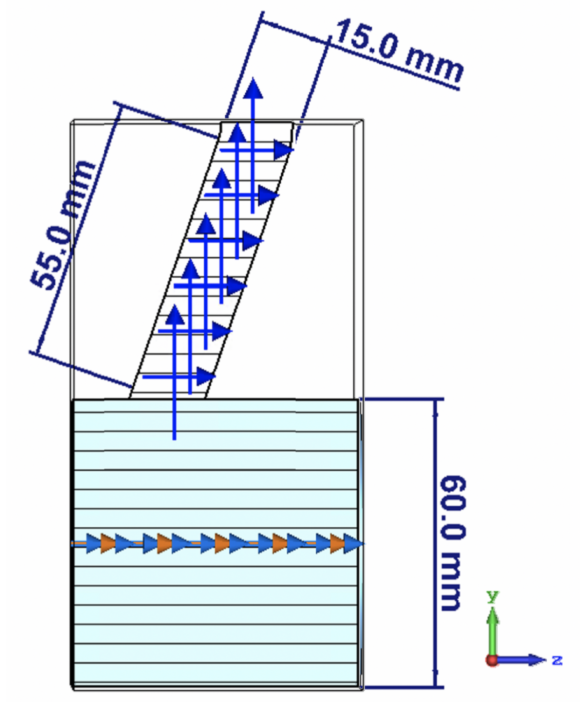

Figure 4.10: Cross-section of the 3D model in CST of a $15\,\mathrm{mm}$ diameter alumina target angled at 71° wrt. the direction of beam travel (in the positive z direction) and the position of the field probes (blue crossed arrows) along the target length spaced at $10\,\mathrm{mm}$ intervals.

seen from the decreasing magnitude of the modulus of the E-field of the first wave front propagating through the dielectric in Fig. 4.11 at times $t = 0.2$, 0.4 and $0.6\,\mathrm{ns}$. The number of peaks in each probe trace also increases with increasing distance along the dielectric as more internal reflections of DR inside the waveguide occur. This is also evident at $t = 0.6\,\mathrm{ns}$ in Fig. 4.11. In the 3D simulation, the DR and ChDR are not easily distinguishable at larger distances from the entrance face of the dielectric due to the mixing of the ChDR and DR. Hence, for the design of the target, the dielectric length was kept as short as possible to minimise reflections and keep the environment as clean as possible.

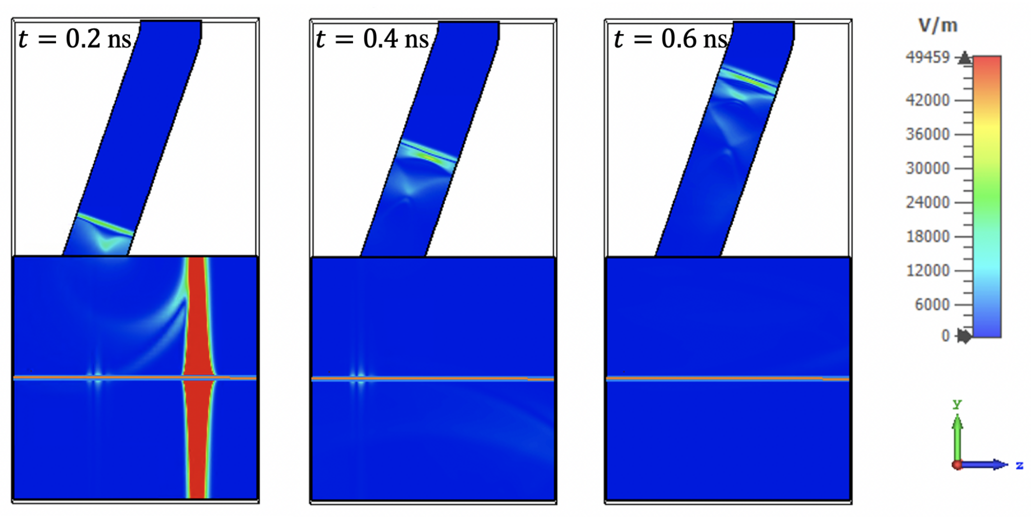

Figure 4.11: Contour plot of the modulus of the E-field for the 3D model shown in Fig. 4.7 at time $t = 0.2\,\mathrm{ns}$, $t = 0.4\,\mathrm{ns}$ and $t = 0.6\,\mathrm{ns}$ in the yz-plane. The beam is travelling in the positive z direction.

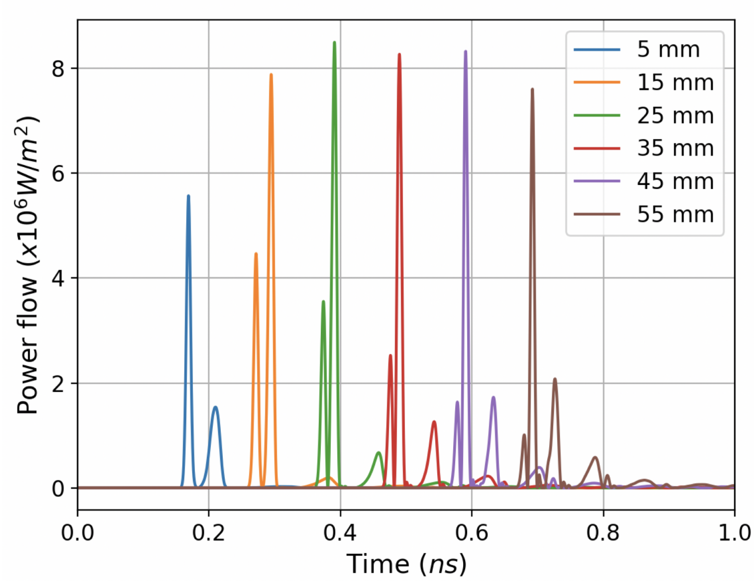

Figure 4.12: Plot of the power flow of PR versus time from the probes that are shown by the crossed blue arrows in Fig. 4.10 that are located at several distances (legend) from the entrance of the alumina.

4.1.6 Target diameter

To understand the impact of the diameter on the PR exiting the alumina target, three different diameters were simulated. These were $15\,\mathrm{mm}$, $6\,\mathrm{mm}$ and $4\,\mathrm{mm}$ with cut-off frequencies of the fundamental TE11-mode at $3.8\,\mathrm{GHz}$, $9.3\,\mathrm{GHz}$ and $14.3\,\mathrm{GHz}$ respectively. The frequency responses of these targets are shown in Fig. 4.13. By using a smaller dielectric diameter to achieve a higher cut-off frequency comes at the cost of the amount of ChDR that is generated. Moreover, there are manufacturing, handling and brazing limitations on the minimum target diameter. Since alumina is a brittle material, the smaller the target diameter, the larger the risk of damage during the manufacturing process. As a compromise between these factors, a dielectric diameter of $6\,\mathrm{mm}$ was chosen. To filter at higher frequencies in the range of $15 - 40$ GHz, as required for suppressing the majority

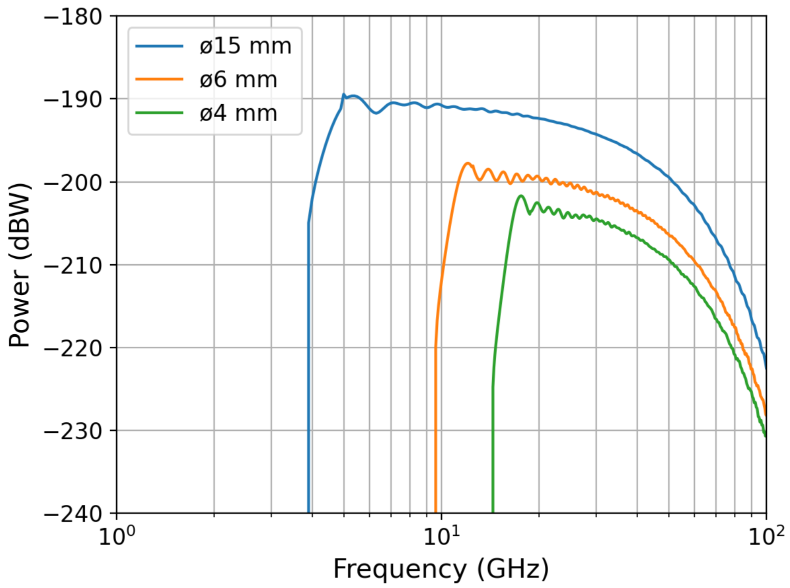

Figure 4.13: Plot of the power of PR from the alumina targets versus frequency for different target diameters.

of the proton bunch power spectrum, industry standard WR28 rectangular waveguides were chosen to transmit the signal from the target. These have a TE10-mode cut-off frequency of $21.1\,\mathrm{GHz}$ and operate in the range $26.5-40\,\mathrm{GHz}$. Due to the availability of in-house WR28 waveguide components, such as band pass filters, an operating frequency of $30\,\mathrm{GHz}$ was chosen. This meant that partial high-pass signal filtering would occur at the level of the alumina and the remaining filtering would be done by the WR28 rectangular waveguide and following components.

4.1.7 ChDR BPM signal properties from CST simulations

In order to obtain the expected signal output power levels and other signal properties of the ChDR target, a full 3D model including the cylindrical alumina ChDR

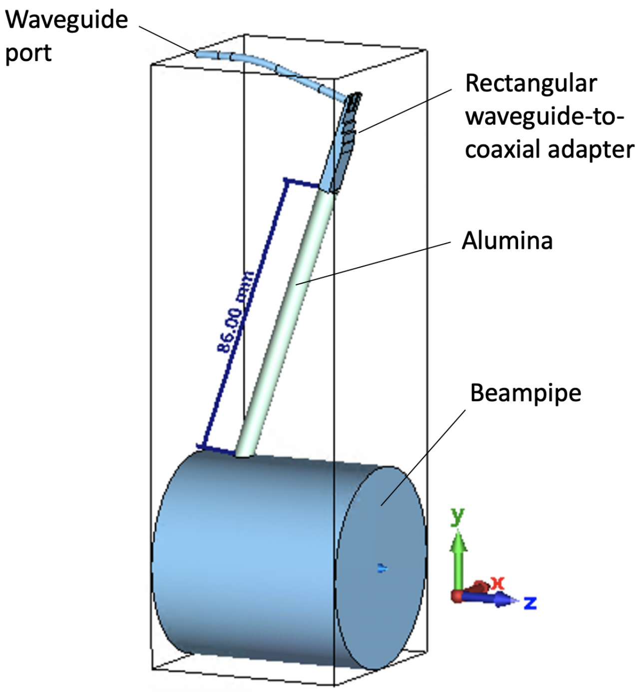

Figure 4.14: 3D model in CST of the beam pipe with one ChDR alumina target (green), the following WR28 rectangular waveguide section and a WG-to-coaxial transition.

target waveguide and a following WR28 rectangular waveguide was created in CST, as shown in Fig. 4.14. A commercial HP R281A waveguide-to-coaxial adapter was also included at the end of the rectangular waveguide transmission line. The dimensions of the adapter and CST model are shown in Fig. 4.15. The frequency response of the adapter from numerical simulation is shown in Fig. 4.16, along with a measurement performed in the laboratory using a Vector Network Analyser (VNA). For the latter, the scattering parameter (or S-parameter) plotted is called the transmission parameter, or S21, which is the ratio of the output voltage wave and the input voltage wave. These results show that the rectangular WR28 waveguide section and the following WG-to-coaxial adapter passes power wave signals above approximately $21\,\mathrm{GHz}$. Again, a bend of the coaxial line was required in the CST simulation model as shown in Fig. 4.14 to include a waveg-

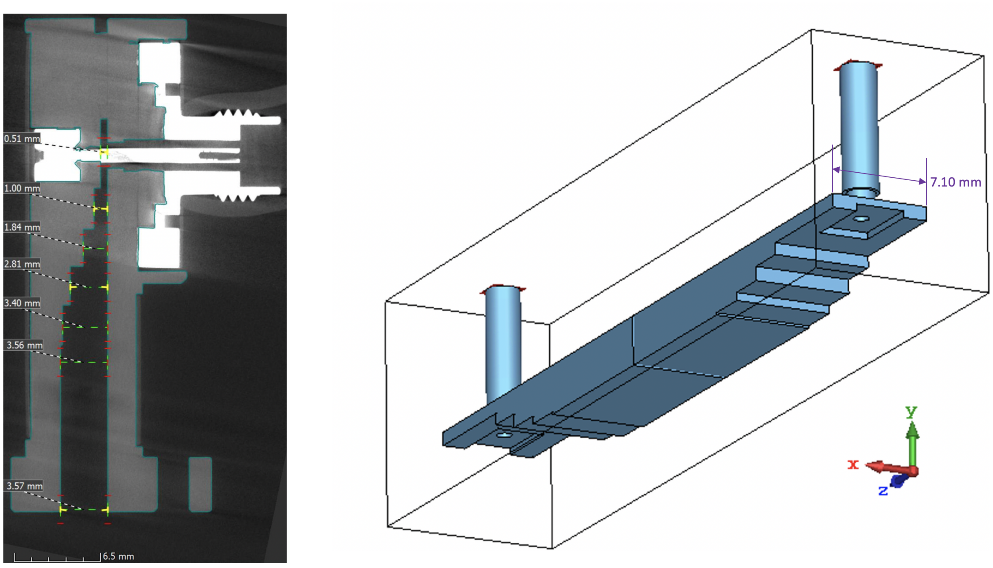

(a) (b)

Figure 4.15: (a) Labelled image of the dimensions of a commercial HP R281A waveguide-to-coaxial adapter. (b) CST model in a back-to-back configuration of two commercial HP R281A waveguide-to-coaxial adapters with the same dimensions as in (a).

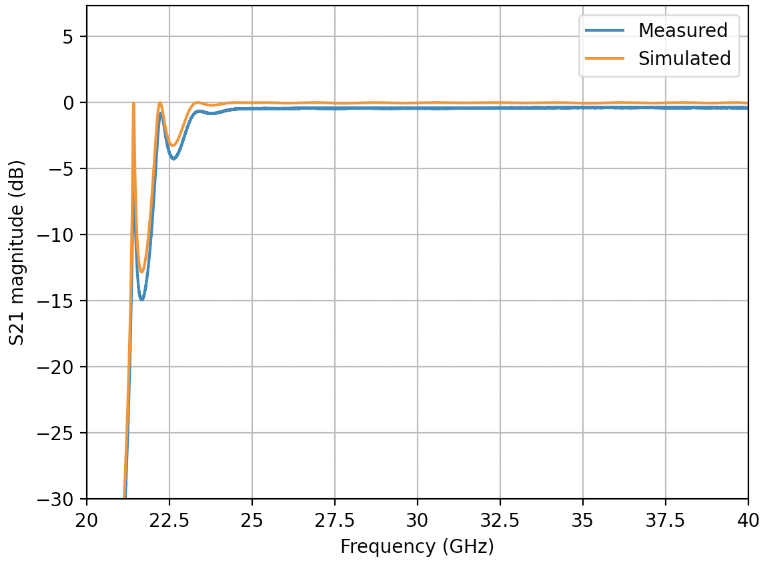

Figure 4.16: Plot of the modulus of the S21 transmission coefficient (in dB) versus frequency for the HP R281A waveguide-to-coaxial adapter.

uide port at the end of the coaxial line to absorb and compute the signal power. As discussed in Section 4.1.5, the length of the alumina ChDR radiator waveguide was kept as short as possible whilst still being compatible with the pBPM bodies but long enough to attach a variety of different signal processing components as the initial part of the RF signal processing. The length was chosen to be $86\,\mathrm{mm}$, with $56\,\mathrm{mm}$ of the alumina staying inside the pBPM body, leaving $30\,\mathrm{mm}$ available for any mechanical attachments.

The time-domain waveform of the signals appearing at the waveguide port at the end of the coaxial line are presented in Fig. 4.17 for different vertical distances of the beam from the beam pipe centre (y direction) i.e. a beam position variation along the vertical plane. These results are for a bunch charge of $600\,\mathrm{pC}$ and longitudinal RMS bunch length of $4\,\mathrm{ps}$. Various characteristics, including the position sensitivity and resolution potential of the ChDR BPM were estimated from these numerical results. By taking the peak value of the time signals in Fig. 4.17 and

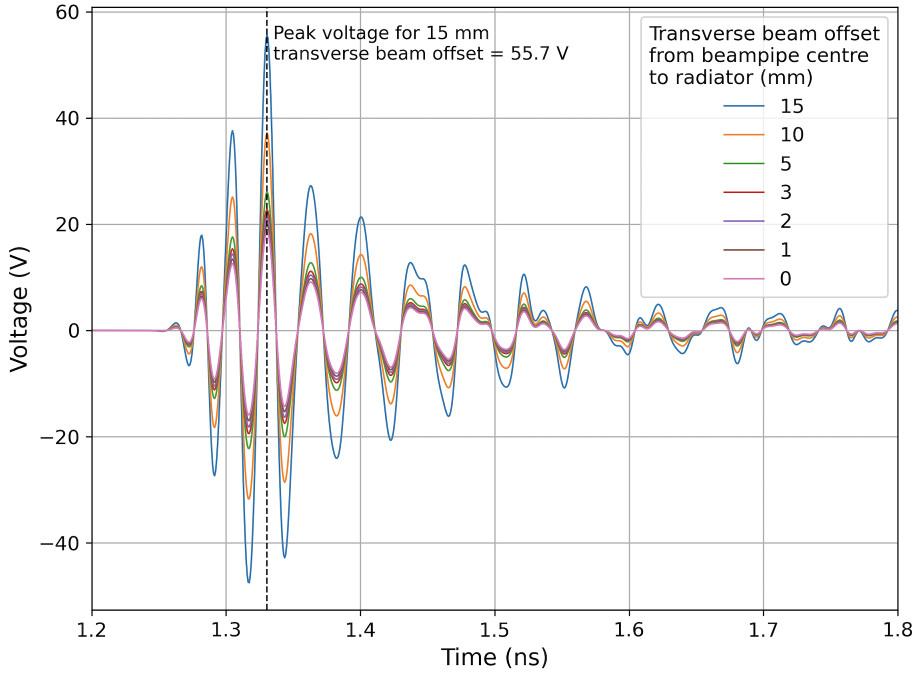

Figure 4.17: Plot of the time response of the complete ChDR radiator arrangement at different vertical beam positions, analyzed using CST.

plotting them against the beam offset, an exponential curve was fitted to the data as shown in Fig. 4.18. The exponential fit for the peak voltage is given by

$$U(y) = A \exp\{T \times y\} + B, \tag{4.2}$$

where $A = 12.0\,\mathrm{V}$, $T = 9.38 \times 10^{-2}\,\mathrm{mm}^{-1}$ and $B = 6.81\,\mathrm{V}$ are the fit parameters, and y is the vertical beam offset. Assuming the ideal case of a perfect symmetric pair of ChDR targets in the vertical plane, this position response was mirrored, i.e. $U(-y)$, and the normalized difference-over-sum position signal $\Delta U/\Sigma U$ was calculated, following the procedure for a "standard" BPM pick-up, see also Eq. 2.13. The result is shown in Fig. 4.19, with a linear region between approximately $\pm 4\,\mathrm{mm}$. The gradient of $\Delta U/\Sigma U$ in the linear region gives the position sensitivity S which is $6 \times 10^{-3}\,/\mathrm{mm}$.

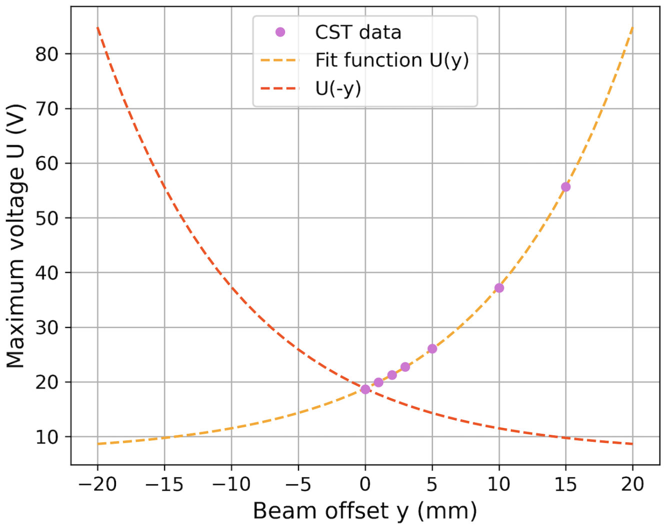

Figure 4.18: Plot of the peak voltage U of the time signals in Fig. 4.17 versus the vertical beam offset y. The fit function $U(y)$ is given in Eq. 4.2. The same response is mirrored for a target on the opposite side of the beam pipe with position response given by $U(-y)$.

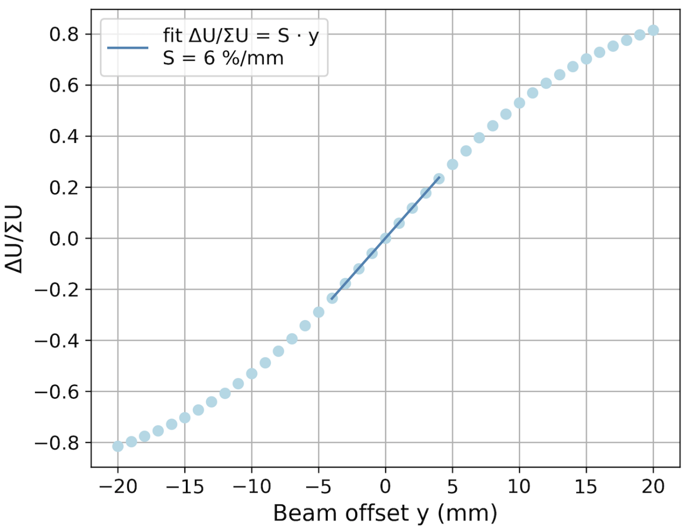

Figure 4.19: Plot of the difference-over-sum of the peak voltage signals $\Delta U/\Sigma U$ from two identical ChDR alumina targets in the same plane, i.e. a complete ChDR BPM pick-up, versus the vertical beam offset y. The blue line is a linear fit in the region between $y = \pm 4\,\mathrm{mm}$, and S is the position sensitivity, i.e. the gradient of the linear fit, and is $6\%/\mathrm{mm}$.

By passing the time signals through a band-pass filter (BPF) with $30\,\mathrm{GHz}$ centre frequency, $300\,\mathrm{MHz}$ bandwidth (BW) and (maximum-flat) Butterworth characteristic, the expected time response signal after the BPF was obtained. This was performed using the Quite universal circuit simulation (Qucs) software [84]. The effect of a $30\,\mathrm{GHz}$, $1\,\mathrm{GHz}$ BW Butterworth BPF on the output signal of the coaxial line was also studied for comparison. Both results shown in Fig. 4.20 and 4.21. The noise voltages V_{noise} were calculated using Eq. 2.33 for the $300\,\mathrm{MHz}$ and $1\,\mathrm{GHz}$ BW filters to be $-83.0\,\mathrm{dBm}$ and $-77.8\,\mathrm{dBm}$ respectively with $T = 300\,\mathrm{K}$ and $R_l = 50\,\Omega$. The maximum achievable resolution was calculated using Eq. 2.32, a position sensitivity of $60\,/\mathrm{m}$ and an estimation of $-12\,\mathrm{dB} = 1/4$ for insertion losses on the signal to account for several metres of rectangular waveguide between the pick-up and the acquisition system, to be $9\,\mathrm{\mu m}$ and $6\,\mathrm{\mu m}$ for $300\,\mathrm{MHz}$ and $1\,\mathrm{GHz}$ BW filters respectively.

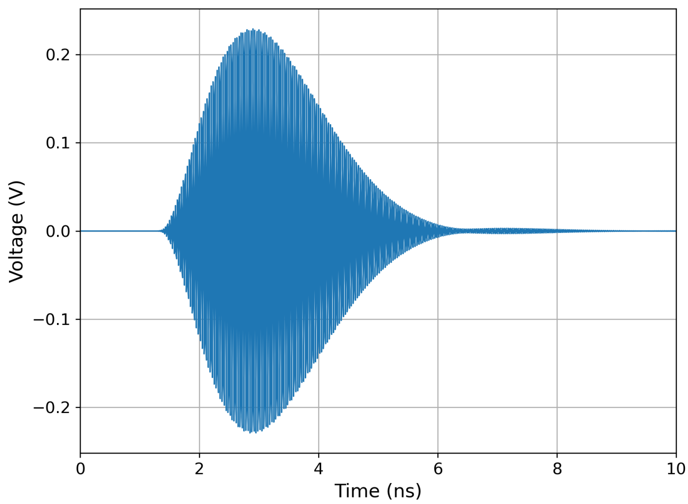

Figure 4.20: Plot of the expected voltage signal of the ChDR BPM model in Fig. 4.14 versus time following a Butterworth band-pass filter with $30\,\mathrm{GHz}$ centre frequency and $300\,\mathrm{MHz}$ BW for $0\,\mathrm{mm}$ vertical beam displacement.

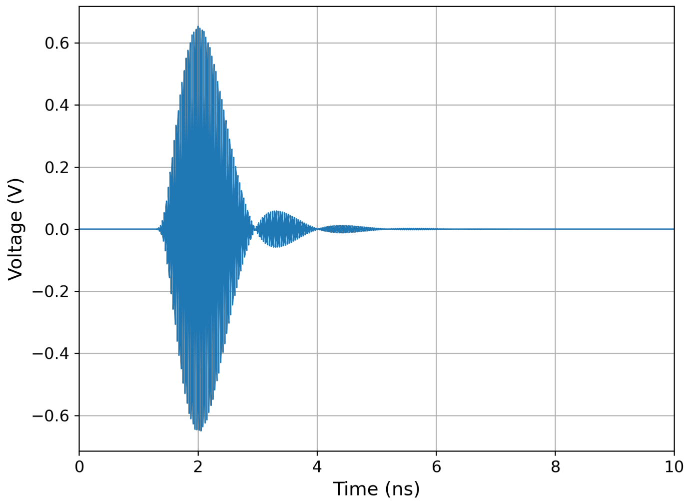

Figure 4.21: Plot of the expected voltage signal of the ChDR BPM model in Fig. 4.14 versus time following a Butterworth band-pass filter with $30\,\mathrm{GHz}$ centre frequency and $1\,\mathrm{GHz}$ BW for $0\,\mathrm{mm}$ vertical beam displacement.

4.1.8 Design of a dielectric-loaded circular-WG to rectangular-WG transition

To maximise signal transmission from the alumina rod, which is a circular dielectric-loaded waveguide to the commercial WR28 rectangular waveguide, a transition was designed and optimised numerically in CST. The mode contributions to the total energy output at the exit of the alumina can be obtained from the simulation model shown in Section 4.1.4 for a $6\,\mathrm{mm}$ diameter alumina target. For an operating frequency of up to 40 GHz, the dielectric-loaded ChDR circular waveguide is heavily over-moded where 16 modes exist below $40\,\mathrm{GHz}$. Fortunately, the majority of the total energy is dominated by the TE11 mode, which is dictated by the particle beam field direction, and there is almost no coupling from the beam to the other modes. The field pattern of this mode is indicated in Fig. 4.22. In the case of the WR28 rectangular waveguide, only the dominant TE10 mode exists

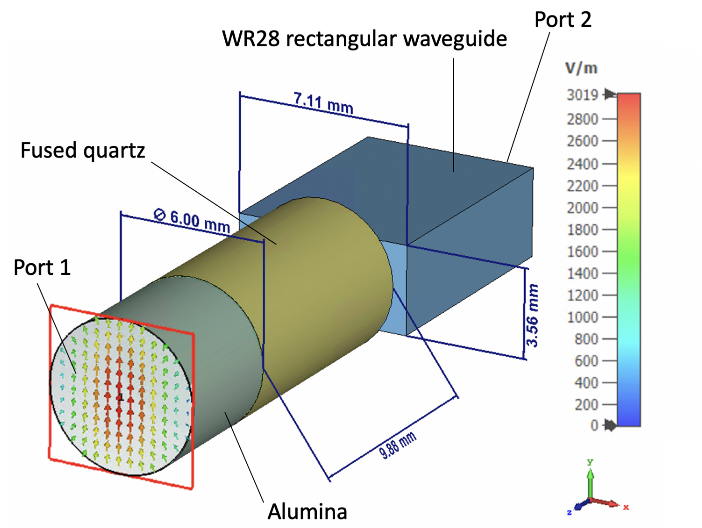

Figure 4.22: CST model of a section of the alumina target and the following signal processing chain. These include a transition made of fused quartz and WR28 rectangular waveguide. The dominant TE11 mode E-field distribution is shown on the circular face of the alumina target.

below $40\,\mathrm{GHz}$, which has a similar field pattern as the TE11-mode in the circular waveguide. However, the wave impedance [85]

$$Z_{TEmn} = \frac{\eta_0}{\sqrt{\varepsilon_r \left[1 - \left(\frac{f_{TEmn}}{f}\right)^2\right]}}, \tag{4.3}$$

where $\eta_0 = 377\,\Omega$ is the impedance of free space, of the dominant TE-modes of the circular and rectangular waveguides at the preferred operating frequency of $f = 30\,\mathrm{GHz}$ differ substantially, $Z_{TE11c} = 126\,\Omega$ for the dielectric-loaded circular waveguide, and $Z_{TE10r} = 528\,\Omega$ for the rectangular WR28 waveguide. In Eq. 4.3 f_{TEmn} is the waveguide cut-off frequency of the TE-mode of interest, i.e. $f_{TE11c} \cong 9.3\,\mathrm{GHz}$ for the circular waveguide, see also Eq. 4.1, and $f_{TE10r} \cong 21.1\,\mathrm{GHz}$ as shown in Fig. 4.16.

It could be demonstrated that an additional dielectric section with a value of relative dielectric permittivity in between that of the dielectric-loaded circular waveguide (alumina: $\varepsilon_r = 9.9$) and that of the rectangular waveguide (air: $\varepsilon_r = 1$) improves signal transmission [86]. For the purpose of an operational BPM with controlled, low signal reflections, fused quartz was chosen as an "intermediate" dielectric with $\varepsilon_r = 3.75$ for a circular waveguide section of $6\,\mathrm{mm}$ diameter, giving a wave impedance at the dominant TE11-mode at $30\,\mathrm{GHz}$ of $225\,\Omega$. To act as a quarter-wave transformer, the physical length of this intermediate circular waveguide section should be $l \approx n\lambda_g/4$, where n is an integer number and [85]

$$\lambda_g = \frac{c}{f\sqrt{1-\left(\frac{f_{TE11}}{f}\right)^2}} \tag{4.4}$$

is the guide wavelength $\lambda_g \cong 11.6\,\mathrm{mm}$ at $f = 30\,\mathrm{GHz}$ for the TE11-mode cut-off frequency $f_{TE11} \cong 15.1\,\mathrm{GHz}$. Following this simplistic approach leads to, e.g. $l \approx 3\lambda_g/4 = 8.7\,\mathrm{mm}$. However, a numerical optimization in CST was followed to achieve the maximum forward transmission coefficient S21 at $30\,\mathrm{GHz}$. The modulus of the transmission coefficient as a function of frequency, $|S21|(f)$, is shown in Fig. 4.23 for the model in Fig. 4.22 with and without the fused quartz transition. The maxima of the $|S21|$ plot with the inclusion of the transition (orange trace) is a result of the standing waves that are set-up inside the transition. The frequency spacing between the maxima is a function of the length of the transition and corresponds to the inverse of the round-trip time of radiation propagating inside the fused quartz. Hence, the longer the transition, the shorter the frequency spacing between maxima. For an optimised length of the waveguide transistion of $9.88\,\mathrm{mm}$, it can be seen that the modulus of S21 is $-0.057\,\mathrm{dB} = 0.993$ at $30\,\mathrm{GHz}$. This corresponds to $99\,\%$ power transmission compared to $35\,\%$ power transmission at $30\,\mathrm{GHz}$ without the fused quartz transition.

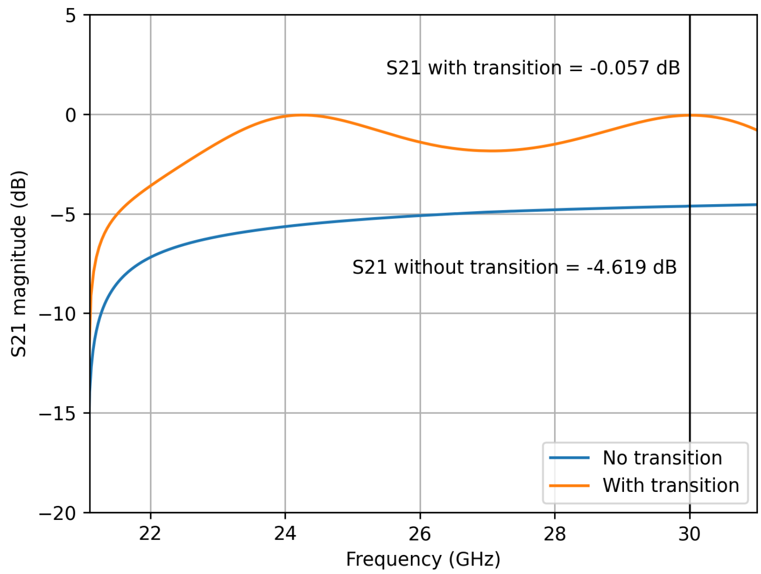

Figure 4.23: Plot of the modulus of the forward transmission coefficient S21 (in dB) as a function of frequency for the model in Fig. 4.22 with and without the fused quartz transition.

By including this waveguide transition in the 3D model of Section 4.1.7, the expected time-domain waveform was re-computed, and the effect of a $300\,\mathrm{MHz}$ or $1\,\mathrm{GHz}$ BW filter on the output signal was simulated in Qucs. The results are shown in Figures 4.24 and 4.25. The estimated resolution improves when the transition is included to $6\,\mu\mathrm{m}$ and $4\,\mu\mathrm{m}$ for a $300\,\mathrm{MHz}$ BW and a $1\,\mathrm{GHz}$ BW filter respectively. Therefore, by maximising the signal transmission at the chosen operating frequency of the BPM via a transition between the alumina and the WR28 rectangular-waveguide, the resolution of the BPM improved and a 1 GHz BW filter provides a better resolution than a $300\,\mathrm{MHz}$ BW filter.

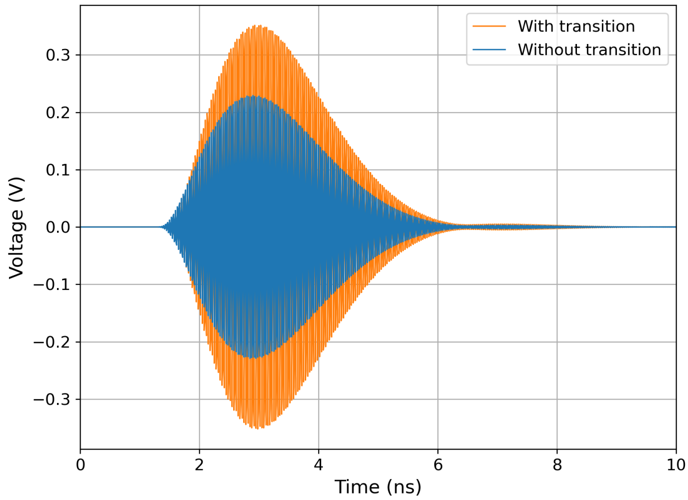

Figure 4.24: Plot of the expected voltage signal as a function of time following a Butterworth band-pass filter with $30\,\mathrm{GHz}$ centre frequency and $300\,\mathrm{MHz}$ BW for a $0\,\mathrm{mm}$ vertical beam displacement with (orange trace) and without (blue trace) the fused quartz transition.

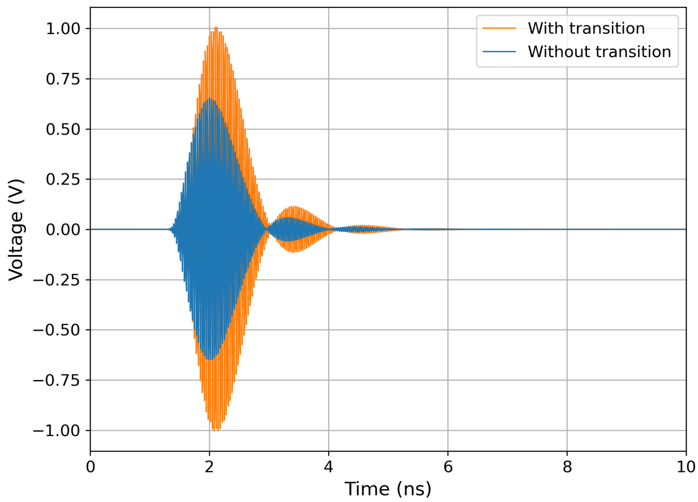

Figure 4.25: Plot of the expected voltage signal as a function of time following a Butterworth band-pass filter with $30\,\mathrm{GHz}$ centre frequency and $1\,\mathrm{GHz}$ BW for a $0\,\mathrm{mm}$ vertical beam displacement with (orange trace) and without (blue trace) the fused quartz transition.

4.1.9 Design of a circular dielectric-loaded waveguide-to-coaxial adapter

As an alternative way to detect the signal from the ChDR alumina target, a direct transition to a coaxial line, i.e. a circular dielectric-loaded waveguide-to-coaxial adapter, was evaluated empirically, with some optimization in CST. The simple geometry with the dimensions and the CST 3D model are shown in Fig. 4.26. Similar to most waveguide-to-coaxial transitions, a short circuit waveguide stub of length approximately $\lambda/4$ is used, with the coaxial centre conductor pin located at the maximum of the E-field. The modulus of the S21 transmission coefficient is shown in Fig. 4.27, clearly indicating the cut-off frequency of the $6\,\mathrm{mm}$ diameter alumina target shown by the sharp transition at $9.3\,\mathrm{GHz}$. Above this frequency, the transmission is broad-band and shows no resonance effects; however, due to the different, unmatched wave impedance, it has an unwanted high insertion loss of approximately $3\,\mathrm{dB}$. Replacing the commercial HP R281A waveguide-to-coaxial adapter in the model shown in Fig. 4.14 in Section 4.1.7 by this very simple circular dielectric-loaded waveguide-to-coaxial adapter (Fig. 4.26) returns the computed time-domain signal waveform at the output. This signal was then

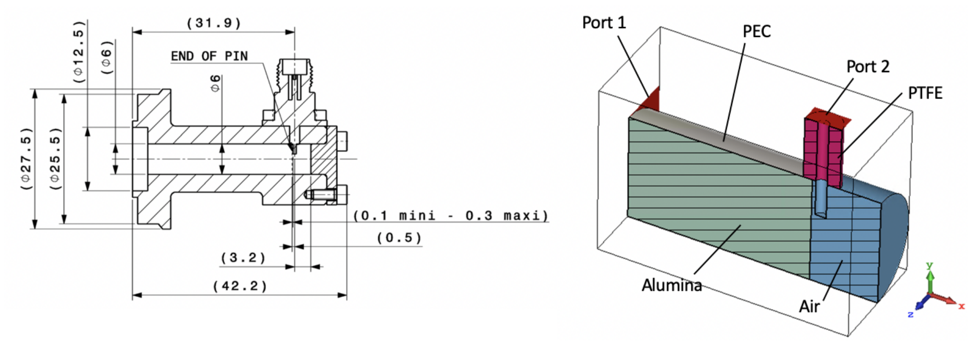

Figure 4.26: Technical drawing with dimensions (left) and CST model of the circular dielectric-loaded waveguide-to-coaxial adapter.

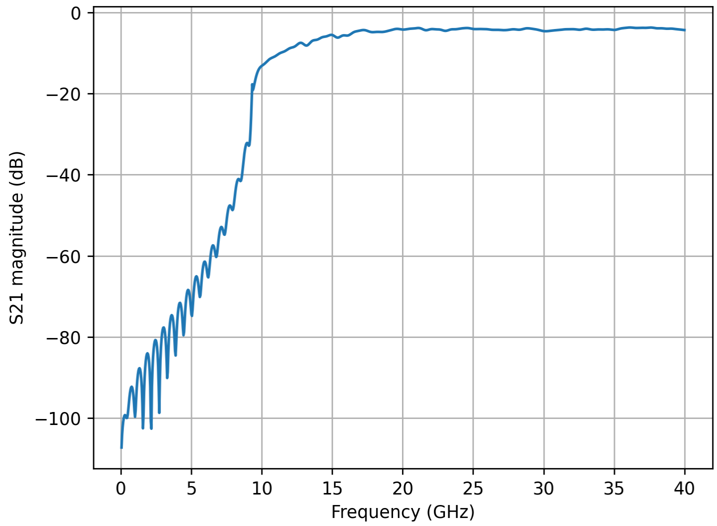

Figure 4.27: Plot of the modulus of the S21 transmission coefficient (in dB) as a function of frequency for the circular dielectric-loaded waveguide-to-coaxial adapter.

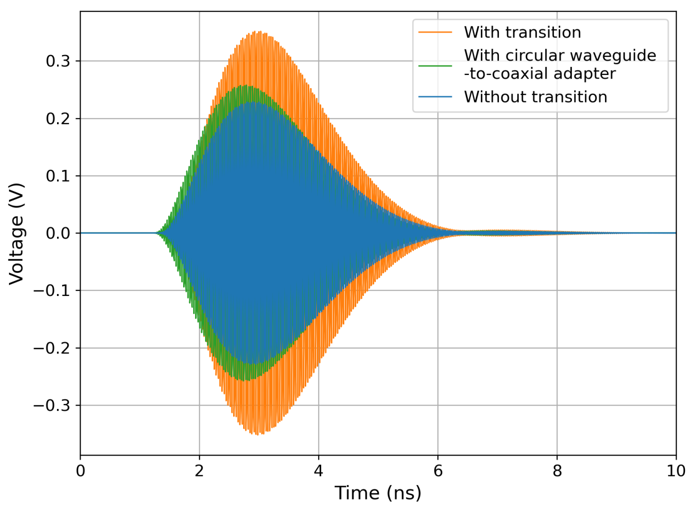

Figure 4.28: Plot of the expected voltage signal as a function of time following a Butterworth band-pass filter with $30\,\mathrm{GHz}$ centre frequency and $300\,\mathrm{MHz}$ BW for a $0\,\mathrm{mm}$ vertical beam displacement with (orange trace) and without (blue trace) the fused quartz transition, and with the circular dielectric-loaded waveguide-to-coaxial adapter (green trace).

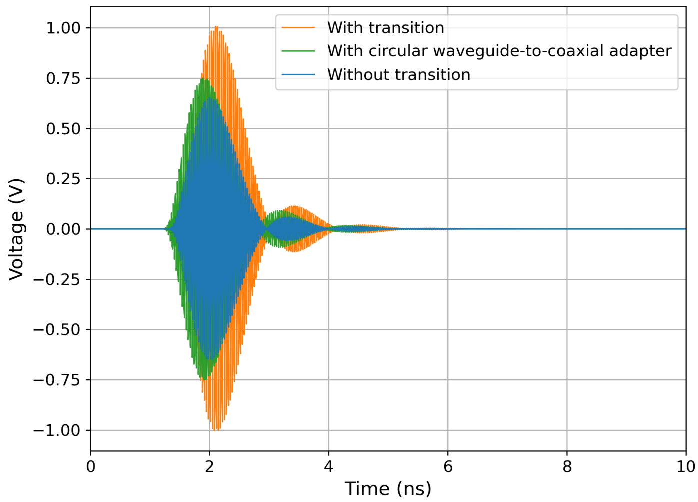

Figure 4.29: Plot of the expected voltage signal following a Butterworth band-pass filter with $30\,\mathrm{GHz}$ centre frequency and $1\,\mathrm{GHz}$ BW for a $0\,\mathrm{mm}$ vertical beam displacement with (orange trace) and without (blue trace) the fused quartz transition, and with the circular dielectric-loaded waveguide-to-coaxial adapter (green trace).

fed into the band-pass filters computed with Qucs for a $30\,\mathrm{GHz}$ centre frequency, with $300\,\mathrm{MHz}$ and $1\,\mathrm{GHz}$ bandwidth; the output signals are shown in Fig. 4.28 and 4.29. The signal shapes and levels are similar to those calculated with the HP R281A adapter.

The circular dielectric-loaded waveguide-to-coaxial adapter discussed in this Section, the commercial HP R281A waveguide-to-coaxial adapter detailed in Section 4.1.7 and the transition described in 4.1.8 were all tested with a laboratory set-up. The set-up design and measurements are presented in the following section.

4.2 RF test-bench characterization of the ChDR target

While beam studies are the ultimate test to characterize the ChDR BPM pick-up, RF measurements on a test-bench under well-controlled conditions in the laboratory help to close the gap between numerical EM simulations and beam measurements. Typically, a stretched-wire or similar coaxial conductor arrangement is used for the RF characterization of an electromagnetic beam pick-up, using a pulse signal or the generator of a vector network analyzer (VNA) as stimulus signal. Because of the large diameter of the AWAKE beam pipe, unwanted non-TEM higher-order modes appear already at low frequencies where the frequency of the lowest TE11-mode would be:

$$f_{TE11coax} = \frac{c}{\pi\sqrt{\mu_r\varepsilon_r}\left(\frac{D+d}{2}\right)} \lessapprox 3.18\,\mathrm{GHz}, \tag{4.5}$$

with $D = 60\,\mathrm{mm}$ being the AWAKE beam pipe diameter and d the diameter of the stretched wire which is considered negligible compared to D. To allow a HOM-free TEM characterization in a frequency range up to $\sim 40\,\mathrm{GHz}$ the outer diameter needs to be $D \lessapprox 4.8\,\mathrm{mm}$, which is incompatible with the $6\,\mathrm{mm}$ diameter of the ChDR radiator.

The RF measurement of the ChDR pick-up is based on a slab line, which is a circular cylinder with radius b between two parallel plates with separation a, proved to be a viable solution. The slab transmission-line was excited with an almost pure TEM field using a VNA and the RF signal was coupled out of the alumina pick-up, enabling the characterization of the transfer function in the frequency domain and the time domain impulse response. Analytical and numerical studies were used to define the geometry of the set-up.

4.2.1 Slab line theory

A schematic of a slab line is shown in Fig. 4.30 [87]. The distance of the centre of the cylinder from the centre of the plates is δ. However, in our application the simple symmetric slab line with $\delta = 0$ was used. The characteristic impedance of a uniform, homogeneous two-conductor, lossless transmission line is

$$Z_0 = \sqrt{\frac{L'}{C'}}, \tag{4.6}$$

where L' is the inductance and C' is the capacitance per unit length. The velocity of propagation is given by

$$v = \frac{1}{\sqrt{L'C'}} = \frac{c}{\sqrt{\mu_r \varepsilon_r}}, \tag{4.7}$$

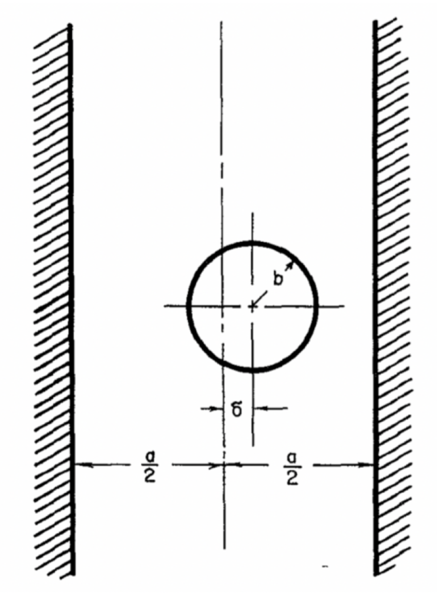

Figure 4.30: Schematic of a slab line with central cylinder and parallel plates [87].

where μ_r is the relative permeability and ε_r is the relative permittivity. By substituting Eq. 4.7 into 4.6, the characteristic impedance can be written

$$Z_0 = \frac{1}{vC'} = \frac{\sqrt{\varepsilon_r}}{cC'}, \tag{4.8}$$

assuming non-magnetic materials ($\mu_r = 1$). Air ($\varepsilon_r = 1$) fills the space between the central cylinder and the walls of the slab line with. Therefore, $Z_0 = 1/cC'$. The capacitance is defined as the ratio of the electrostatic charge on the cylinder and the potential difference i.e. the voltage between the cylinder and the plates. The charge (per unit length) Q' is given by the integral of the surface charge density $\rho(\varphi)$ (Gauss's law):

$$Q' = \int_0^{2\pi} \rho(\varphi) b d\varphi. \tag{4.9}$$

The electrostatic potential can be expressed

$$\phi(r, \varphi) = \frac{1}{\varepsilon} \int_0^{2\pi} \rho(\varphi') G(b, \varphi', r, \varphi) b d\varphi', \tag{4.10}$$

where $G(r', \varphi', r, \varphi)$ is the Green's function, which is the potential ϕ at point (r, φ) due to unit line charge at (r', φ'). The potential function and, hence, the Green's function must obey the same boundary conditions, namely that the function vanishes at the surface on the plates and the charge is located on the surface of the cylinder, $r' = b$. For points on the cylinder, the potential must be a constant value. This is then expressed

$$\phi_0(r, \varphi) = \frac{1}{\varepsilon} \int_0^{2\pi} \rho(\varphi') G(b, \varphi', b, \varphi) b d\varphi'. \tag{4.11}$$

This problem can then be solved using a variational method as described in [87]. The simplified formula for the characteristic impedance of a symmetric slab line,

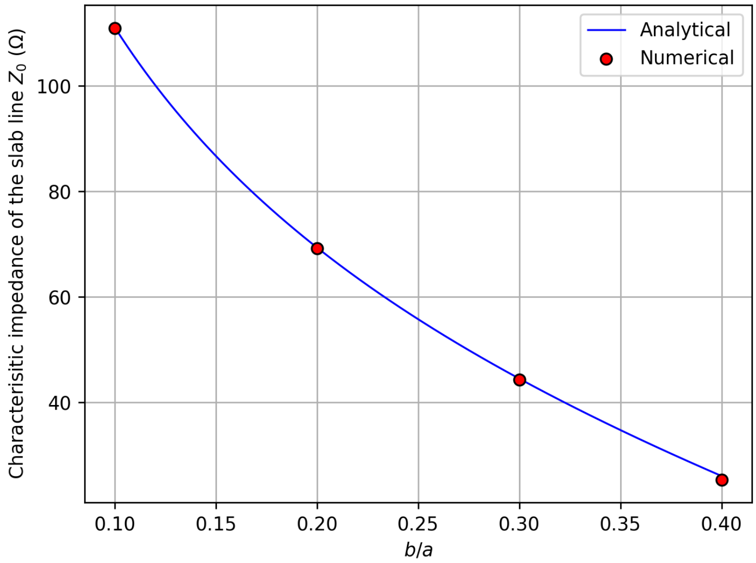

Figure 4.31: Characteristic impedance of the slab line vs. the ratio of the central cylinder radius b and plate spacing a.

i.e. when there is no offset of the cylinder ($\delta = 0$), is then given by [87]

$$Z_0 = \eta_0 \left[\frac{1}{2\pi} \ln\left(\frac{2a}{\pi b}\right) - \frac{0.2153R^2}{1 + 5.682R^2} \right], \tag{4.12}$$

with $\eta_0 \cong 377\,\Omega$ being the wave impedance of free space and $R = (b/a)^2$. The analytical expression for the characteristic impedance plotted against the ratio of the central cylinder radius and plate spacing is shown in Fig. 4.31.

4.2.2 Slab line design

To achieve a slab line characteristic impedance $Z_0 = 50\,\Omega \;\Rightarrow\; b/a = 0.2745$. For a central conductor of diameter $2b = 1.00\,\mathrm{mm}$, and a desired slab line impedance of $Z_0 = 50\,\Omega$, the plate separation should be $a = 1.822\,\mathrm{mm}$.

The slab line was modelled in CST, as shown in Fig. 4.32. The transmission

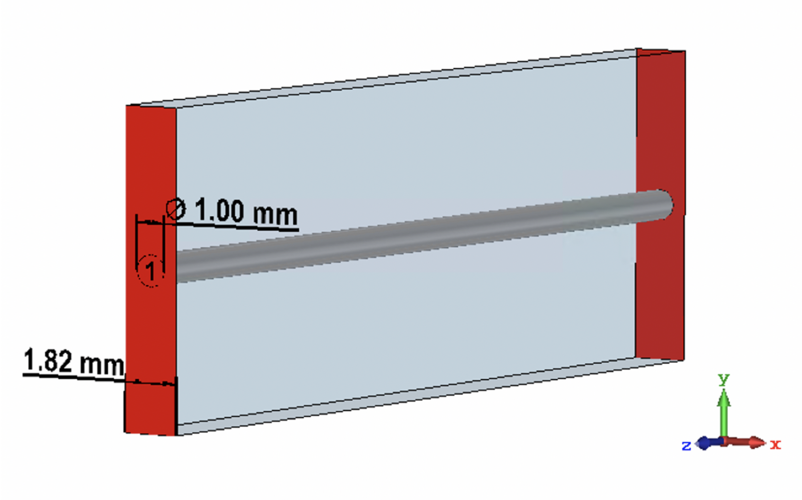

Figure 4.32: CST simulation geometry of the slab line with $b/a = 0.2745$.

line is excited via port 1 shown by the red surface on the left-hand side and the transmitted signal is absorbed at port 2 located on the opposite side. The boundary conditions are transverse electric and the simulation frequency ranges from 0 to $44\,\mathrm{GHz}$. The mesh density is 15 mesh cells per wavelength. The line impedance is calculated in CST by applying Eq. 4.6 and the numerical results for several b/a values are displayed in Fig. 4.31 as red circles. For the practical setup, a $2.4\,\mathrm{mm}$ coaxial connector was required for the connection to a VNA. The slab line side of this connector consists of a female centre connector of $0.55\,\mathrm{mm}$ diameter, which is able to accept pins with a maximum diameter of $0.3\,\mathrm{mm}$, see the details in Fig. 4.33. The characteristic impedance of the coaxial line-segment inside the $2.4\,\mathrm{mm}$ connector was calculated using the well-known equation for coaxial cylinders

$$Z_0 = \frac{\eta_0}{2\pi\sqrt{\varepsilon_r}} \ln\left(\frac{D}{d}\right) \cong \frac{60\,\Omega}{\sqrt{\varepsilon_r}} \ln\left(\frac{D}{d}\right) \tag{4.13}$$

and is $50\,\Omega$, with D being the diameter of the outer shielding conductor and d the diameter of the inner centre conductor.

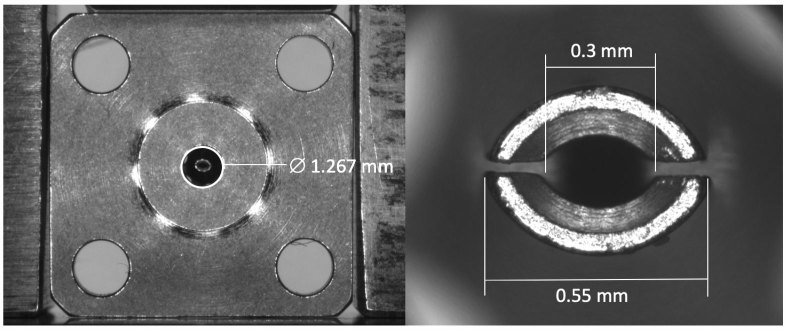

Figure 4.33: Image of the slab line side of the $2.4\,\mathrm{mm}$ coaxial flange connector, which is used to attach a $50\,\Omega$ coaxial cable to the slab line.

With the calculated dimensions of the slab line ensuring $50\,\Omega$ characteristic impedance i.e. $b/a = 0.2745$, there still exists three non-TEM modes below $44\,\mathrm{GHz}$, as seen in Fig. 4.34 and using the model in Fig. 4.32. However, the TEM field from the coaxial cable mainly excites the TEM mode in the slab line, as proved by a numerical CST simulation shown in Fig. 4.35 by analyzing the

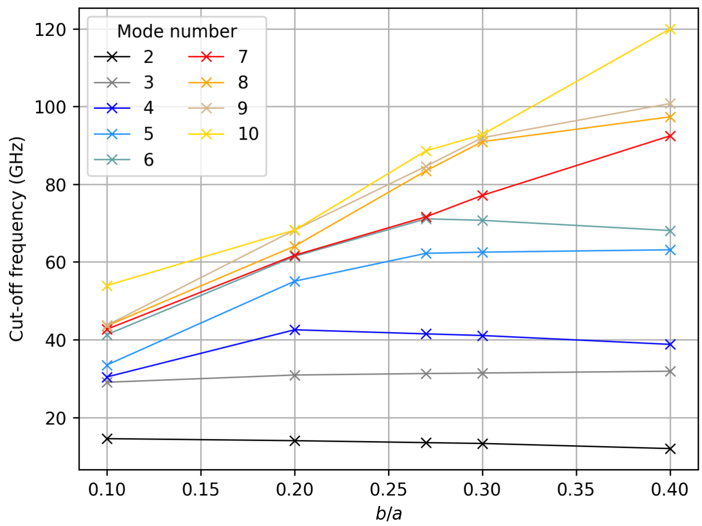

Figure 4.34: Cut-off frequencies of the first 10 modes for different plate separations using the simulation geometry as shown in Fig. 4.32.

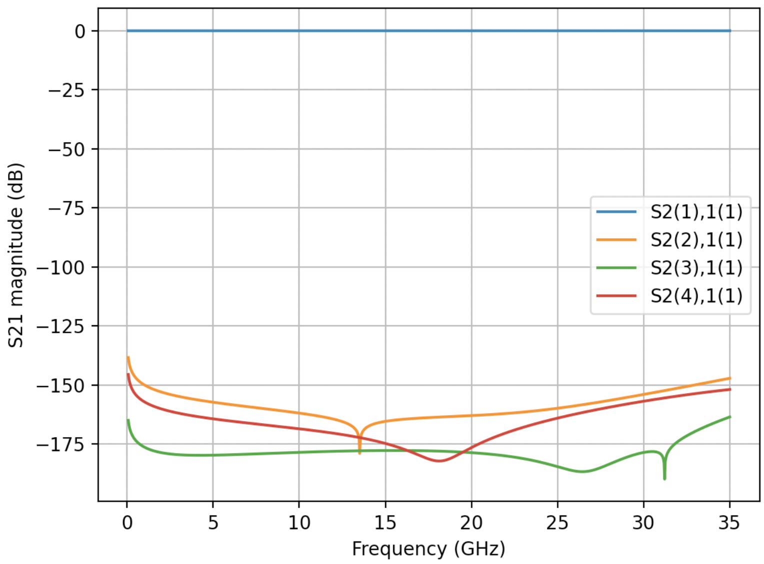

Figure 4.35: Plot of |S21| parameter vs. frequency for modes below 44 GHz with TEM excitation, using the simulation geometry as shown in Fig. 4.32. The legend shows the mode number for both port 1 and 2. For example, S2(3),1(1) represents the transmission coefficient S21 with first mode excitation, i.e. TEM mode excitation, at port 1 and third mode absorption at port 2.

scattering (S) parameters – here, the modulus of the S21 transmission parameter – of the structure for the various mode patterns with a TEM mode excitation.

Since the central tube conductor of the slab line and the centre conductor of the coaxial adapter have different diameters, a tapered transition between them was designed to minimize the change in the characteristic impedance, thus to minimise reflections. The model of the conical transition, as it was optimized, is shown in Fig. 4.36. Port 1 excites the TEM mode in the coaxial line and port 2 absorbs the first 10 modes of the slab line. A step signal is introduced at port 1 and the line impedance result is shown in Fig. 4.37 as a function of the round trip time of light in the dielectric which in this case is air. The length of the transition was scanned and the optimal length was found to be 0.5 mm.

A simplified model with the entire slab line and the coaxial connectors on

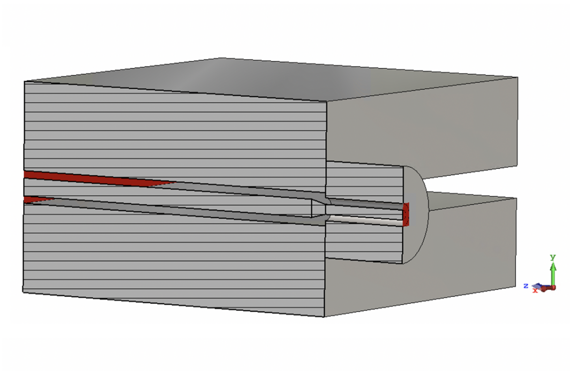

Figure 4.36: Model for optimising the transition length between the coaxial connector and the central tube conductor.

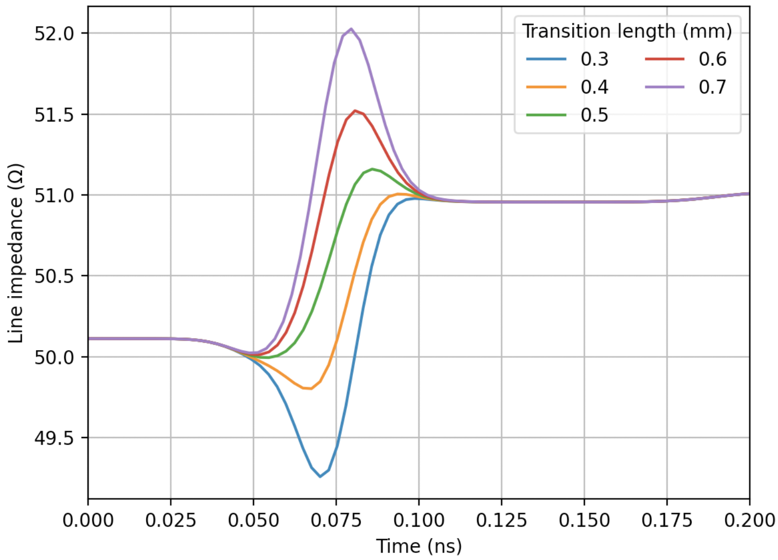

Figure 4.37: Plot of line impedance vs. round trip time, i.e. two times the distance along the transmission line divided by the phase velocity of light in the dielectric, of the coaxial-to-slab line transition for different transition lengths.

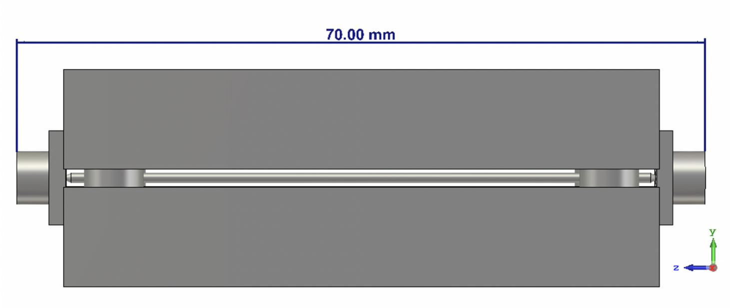

Figure 4.38: Simplified model of the slab line in CST.

either side of the line is shown in Fig. 4.38 and the final mechanical design of the slab line is shown in the technical drawing Fig. 4.39. The length of the ground plates, $60\,\mathrm{mm}$, was chosen to allow for the addition of a top plate with the alumina target and to prevent sagging of the central conductor. The width, $40\,\mathrm{mm}$, was chosen by looking at the E-field through a slice of the slab line in CST, Fig. 4.40, and ensuring that there is a reasonably low EM-field near the outer edges of the plates.

The components labelled in the technical drawing are made of aluminium, apart from the central tube and the transitions, which are made from stainless steel, and the coaxial connectors which are made of a mixture of metals, the details of which can be found in [89]. By replacing the top plate with a ChDR alumina target assembly, the transfer function and time-domain response of the alumina target can be characterised. The CST model is shown in Fig. 4.41, where the left inset is a model including the HP R281A WR28 rectangular waveguide-to-coaxial adapter and the right inset is the same with the addition of the circular dielectric-loaded waveguide-to-coaxial transition made from fused quartz. Again, the ChDR is generated inside the alumina and propagates at the Cherenkov angle. The DR from the edge of the entrance of the alumina also propagates inside the target. This is indicated by the contour plot of the E-field on the left inset of

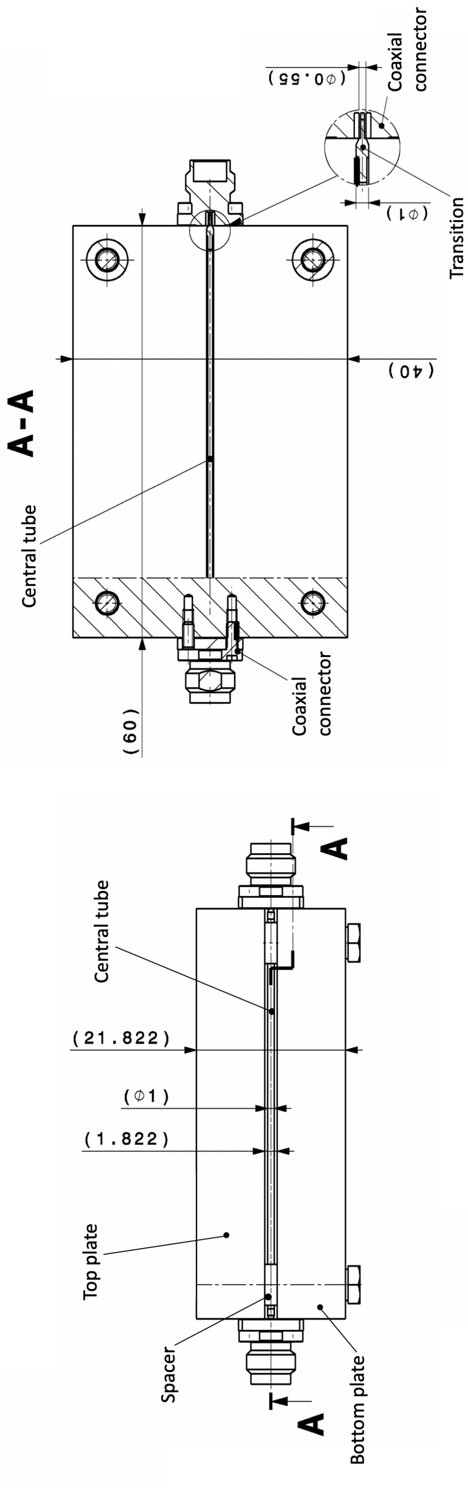

Figure 4.39: Technical drawing of the slab line [88]. The dimensions are given in mm.

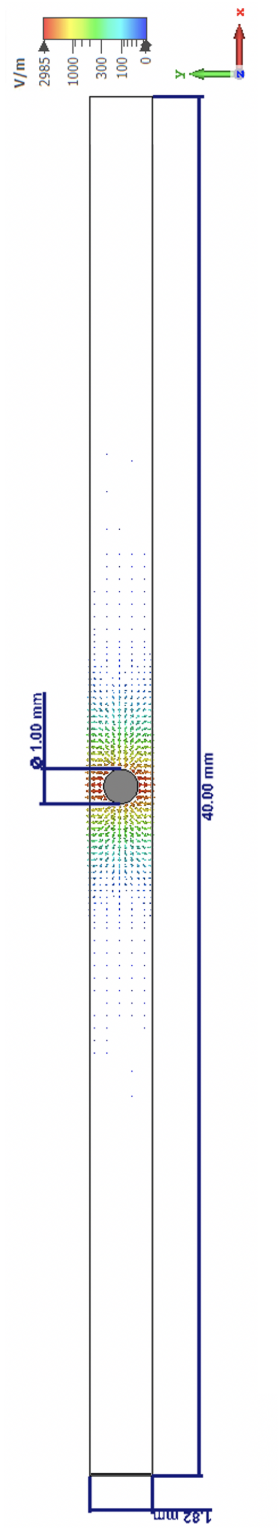

Figure 4.40: 2D slice of the slab line and the E-field distribution.

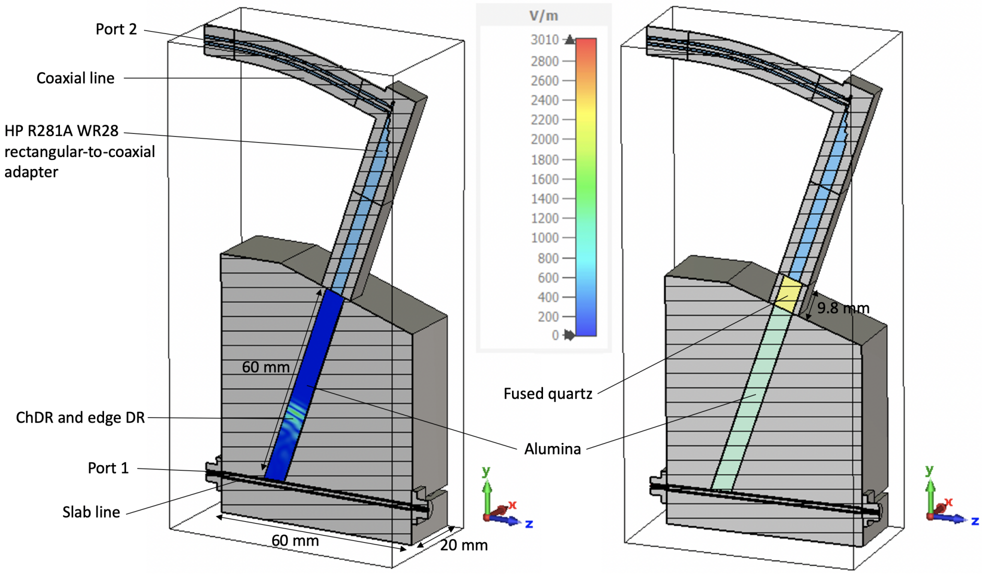

Figure 4.41: CST model of the alumina target with excitation via a slab line. The signal was calculated using a HP R281A WR28 rectangular waveguide-to-coaxial adapter without (left) and with (right) the fused quartz transition. The ChDR and DR inside the alumina are shown by the contour plot of the E-field (left).

Fig. 4.41. The signal from the alumina can also be measured with the circular dielectric-loaded waveguide-to-coaxial adapter from Section 4.1.9. This model is shown in Fig. 4.42. Fig. 4.43 displays the mechanical design with the fused quartz transition and WR28 rectangular waveguide attachment as an example.

The results of the numerical computations for the four different models, Fig. 4.38, Fig. 4.41 left and right, and Fig. 4.42, will be presented in the next section and compared with the RF-measurements performed with a VNA.

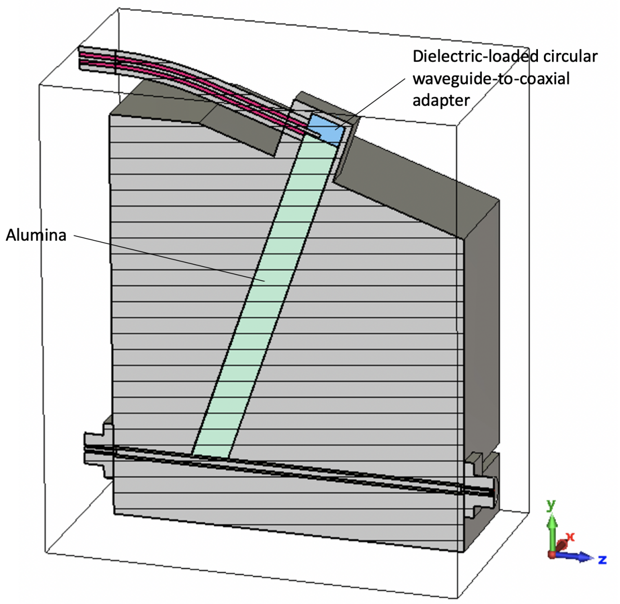

Figure 4.42: CST model of the alumina target with excitation via a slab line. The signal is measured using the circular dielectric-loaded waveguide-to-coaxial adapter described in Section 4.1.9.

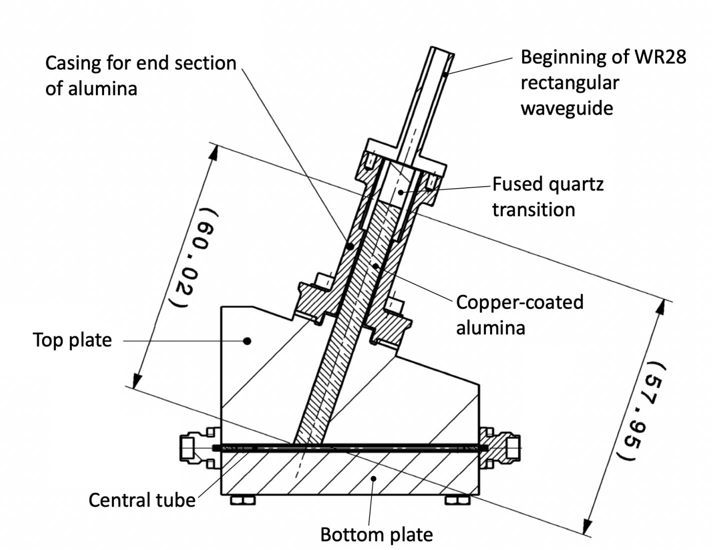

Figure 4.43: Technical drawing of the alumina target and slab line [88]. The fused quartz transition is shown at the end of the alumina and connected to a WR28 rectangular waveguide section.

4.2.3 Laboratory measurements of the slab line and comparison to numerical simulations

To characterise the ChDR alumina target by measuring its transfer function and the time-domain response, the slab line assemblies with and without the alumina target (Figures 4.43 and 4.39 respectively) in the previous section were manufactured. The laboratory set-up of the various assemblies for the slab line are shown in Figures 4.44, 4.45 and 4.46.

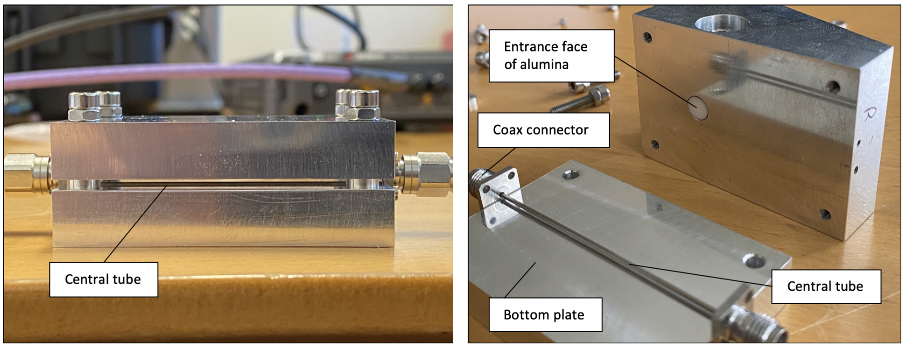

Figure 4.44: Laboratory set-up of the slab line with central tube, and top and bottom ground plates (left). Disassembled slab line set-up with the top plate that holds the alumina target (right).

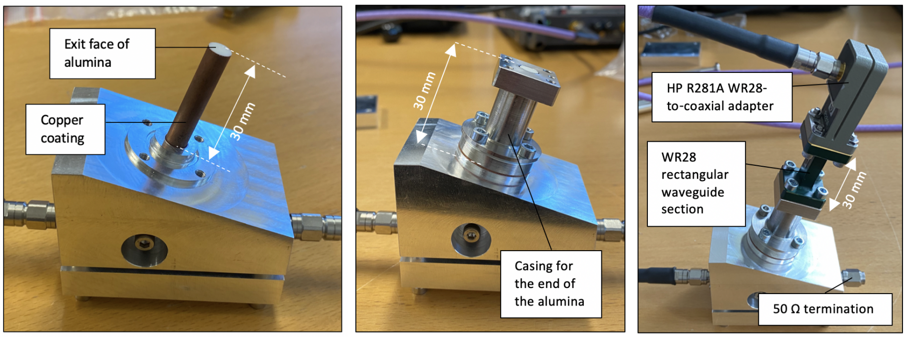

Figure 4.45: Assembled slab line with the copper-coated alumina target (left), the casing for the end of the alumina target (middle), and the WR28 rectangular waveguide section and the HP R281A WR28 rectangular waveguide-to-coaxial adapter (right).

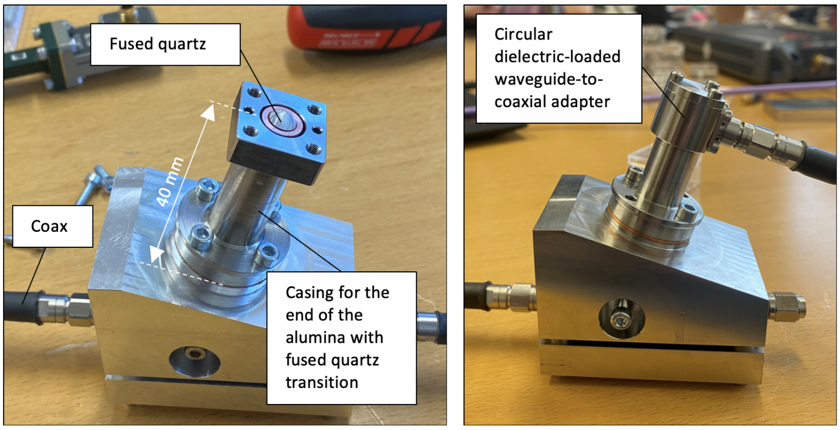

Figure 4.46: Set-up of the slab line with the alumina target and fused quartz transition (left), and with the circular dielectric-loaded waveguide-to-coaxial adapter detailed in Section 4.1.9 (right).

The characteristic impedance along the slab line with (Fig. 4.45 left), and without (Fig. 4.44 left) the alumina was measured with a Keysight P5007A USB VNA operating from $10\,\mathrm{MHz}$ to $44\,\mathrm{GHz}$. The VNA measures the S-parameters, and for this particular time-domain reflectometry (TDR) measurement the S11 reflection coefficient $\Gamma(f)$. Operating the instrument in time-domain, TDR step response mode enables the inverse fast Fourier transform (iFFT) together with the convolution of a Heaviside step function, by multiplying the frequency domain response with $\delta(f)/2 + 1/j2\pi f$. The measured TDR coefficient $\Gamma(t)$ is then converted by the VNA to the characteristic impedance

$$Z(t) = Z_0 \frac{1 + \Gamma(t)}{1 - \Gamma(t)}, \tag{4.14}$$

where $Z_0 = 50\,\Omega$ is the reference characteristic impedance of the instrument. The round trip time t is related to the distance along the line s via $s = v_p t/2$, where $v_p = c/\sqrt{\varepsilon_r}$ is the phase velocity of light in the dielectric which in this case is $\varepsilon_r = 1$ for air.

The characteristic impedance as a function of the round trip time is shown in Fig. 4.47 along with the computed result from CST. First, when the alumina is not included, the characteristic impedance stays close to the designed value of $50\,\Omega$. Increases in the impedance in both the measured and simulated results can be seen at around $0.05\,\mathrm{ns}$ and $0.45\,\mathrm{ns}$ due to the transition between the tube and the coaxial connectors. The distance calculated from the difference between these two points in time corresponds to the length of the slab line, which is $60\,\mathrm{mm}$.

When the top plate that holds the ChDR alumina target assembly is included, there is a large increase in the characteristic impedance at around $0.2\,\mathrm{ns}$, peaking at $64\,\Omega$ in the measured response, which agrees well with the CST simulation (Fig. 4.47). This is due to the ChDR alumina target located at around $20\,\mathrm{mm}$ from the start of the slab line, which presents a local jump in characteristic impedance, i.e. being more inductive. The differences between the measured and simulated

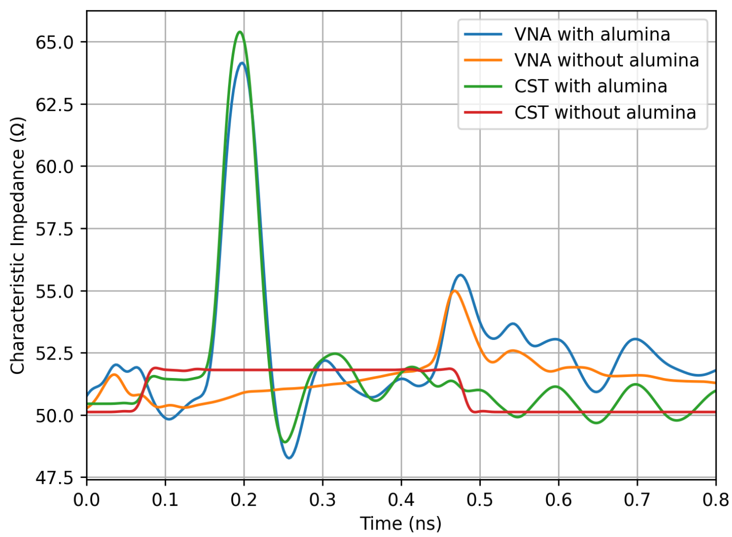

Figure 4.47: Characteristic impedance as a function of the round trip time of the slab line with and without the alumina target. Both the measured and numerically analysed cases are shown.

cases are due to manufacturing tolerances. Furthermore, in the numerical simulations, all materials were implemented as perfect, lossless materials.

Since there is no known method of analytically analyzing HOMs for the slab line, a modal analysis was carried out numerically in CST as presented in Fig. 4.34. It was shown that 3 non-TEM modes exist below $44\,\mathrm{GHz}$. However, only the TEM-mode is excited by the coaxial line (Fig. 4.35). This was verified by S-parameter measurements with the VNA. These results are plotted in Fig. 4.48 and show an almost perfect forward transmission (S21) over the entire range of frequencies, with very low reflections (S11).

The coaxial line to port 2 of the VNA was then removed from one end of the slab line and replaced with a $50\,\Omega$ termination as shown in Fig. 4.45 (right). A $30\,\mathrm{mm}$ long, WR28 rectangular waveguide piece and the HP R281A WR28 rectangular waveguide-to-coaxial adapter were added to the end of the alumina target,

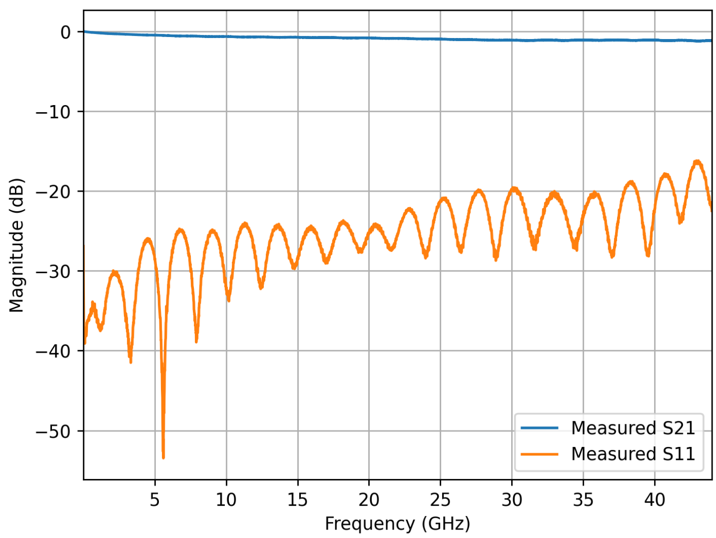

Figure 4.48: Plot of the $|S21(f)|$ forward transmission and the $|S11(f)|$ reflection coefficient, the so-called return loss, of the slab line.

to which the coaxial line was then attached to, to measure the transmitted radiation. The measured S21 transfer function is shown in Fig. 4.49, along with the analysis from CST using the model shown in Fig. 4.41 (left) from Section 4.2.2. The discrepancy between the measured and simulated result below approximately $21\,\mathrm{GHz}$ arises due to two reasons. First, the bandwidth limitation of the input signal is restricted to frequencies between 2.6 and $44\,\mathrm{GHz}$ in order to imitate the input signal of the VNA and results in the discontinuity of the blue trace at $2.6\,\mathrm{GHz}$. Furthermore, the simulation is carried out with the time domain solver where an accuracy of the frequency domain signals has to be defined to ensure a reasonable simulation duration. This was set to $-40\,\mathrm{dB}$. Hence, anything below $-40\,\mathrm{dB}$ should not be compared with the measured result.

The USB VNA then applies the iFFT to the $S21(f)$ data to generate the time-

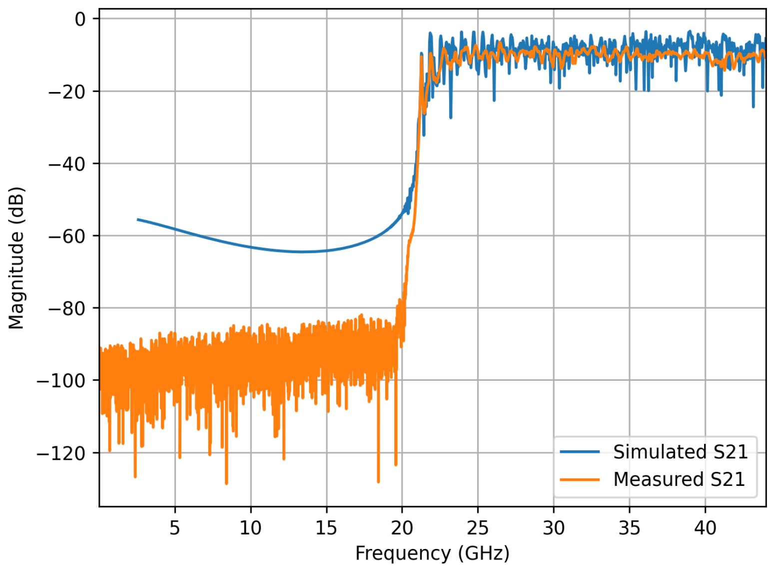

Figure 4.49: Plot of measured and simulated |S21| transfer response vs. frequency for the alumina target excited via a slab line. This measurement was performed with the HP R281A waveguide-to-coaxial adapter.

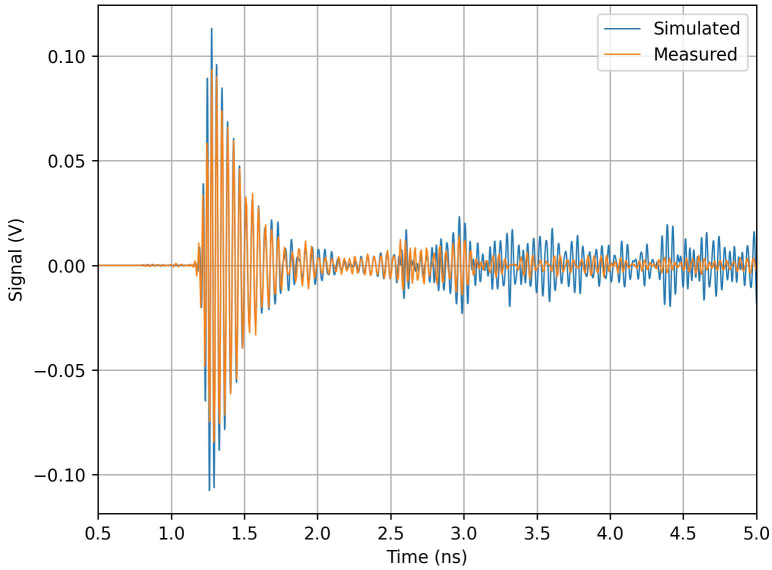

Figure 4.50: Plot of measured signal vs. time of the alumina target excited via a slab line. The signal is measured with a HP R281A waveguide-to-coaxial adapter.

domain impulse response. This is shown together with the simulated result in Fig. 4.50. The measured frequency-domain (FD) and time-domain (TD) responses agree relatively well with the simulations. However, there is much more "ringing" observed in the numerical TD response compared to the measured case. This discrepancy is partly due to numerical noise which can be reduced by using a smaller mesh cell size in the simulations, as well as shrinking the frequency range in the simulation to the pass-band of the system, which has a high-pass like characteristic. In fact, extending the simulation response to frequencies well below the cut-off frequency f_{TE10} does not give any additional information, but only adds numerical noise. Other factors that contribute to the excessive ringing could be the lack of surface impedance and roughness of the materials in the simulation.

It can also be seen from the TD response that there is an initial signal that arrives at around $1.2\,\mathrm{ns}$. Due to the mismatch between the wave impedances of the circular dielectric-loaded waveguide (alumina target) and the WR28 rectangular waveguide, there is a fraction of the signal power that is reflected back into the alumina waveguide. Upon reaching the entrance face of the circular alumina WG, again a wave impedance mismatch is present, and once more a fraction of the already reflected signal power is reflected back, now heading towards the WR28 waveguide and being detected with a delay to the incident signal. This is evident in the TD response with a signal peaking around $1.4\,\mathrm{ns}$ after the initial pulse, corresponding to the round trip time of the radiation travelling inside the $60\,\mathrm{mm}$ long alumina target and the $\sim 60\,\mathrm{mm}$ long air-filled WR28 waveguide. This back and forth travelling signal power in the alumina target forms standing wave effects, which contribute to the regularly-spaced notches in the S21 FD response.

The measurements were repeated with the fused quartz transition and HP R281A adapter, and with the circular dielectric-loaded waveguide-to-coaxial adapter, shown in Fig. 4.46, left and right respectively. The computations were performed with the corresponding CST models shown in Figures 4.41 (right) and 4.42. The measured and simulated FD and TD responses are plotted in Figures 4.51, 4.52, 4.53 and 4.54. Whilst the WR28 waveguide suppresses the signal transmission below the cut-off frequency of the dominant TE10-mode, which is $21.1\,\mathrm{GHz}$, as shown by the sharp transition in the FD at this frequency in Figures 4.49 and 4.51, the circular waveguide-to-coaxial adapter provides the FD for the entire frequency range down to the cut-off frequency of the dominant TE11-mode of the circular alumina waveguide, which is approximately $9.3\,\mathrm{GHz}$, as shown by Fig. 4.53.

The ChDR target was fully characterised using the slab line and VNA to frequencies up to $44\,\mathrm{GHz}$. The measurements matched well with and verified numerical simulations; discrepancies were due to machining tolerances, numerical noise and inaccuracies in the modelling of the materials.

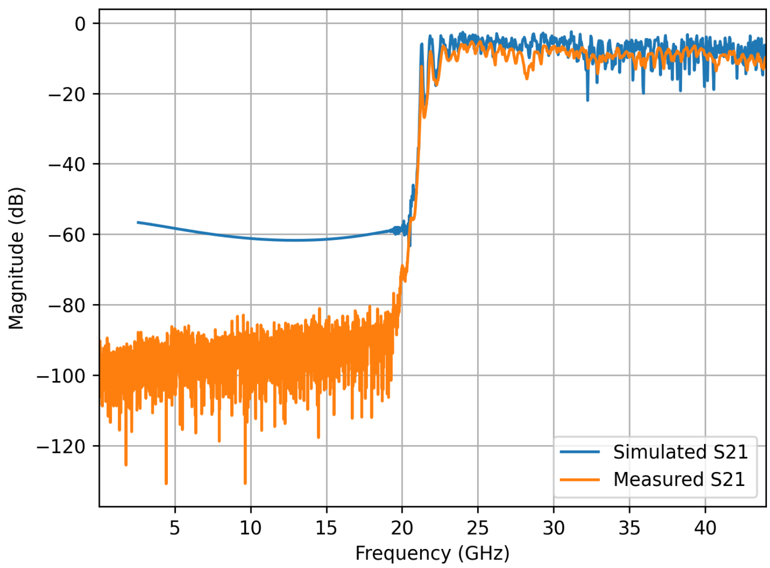

Figure 4.51: Plot of measured and simulated |S21| vs. frequency for the alumina target excited via a slab line. The signal goes through a fused quartz transition, a short WR28 waveguide piece and a HP R281A waveguide-to-coaxial adapter.

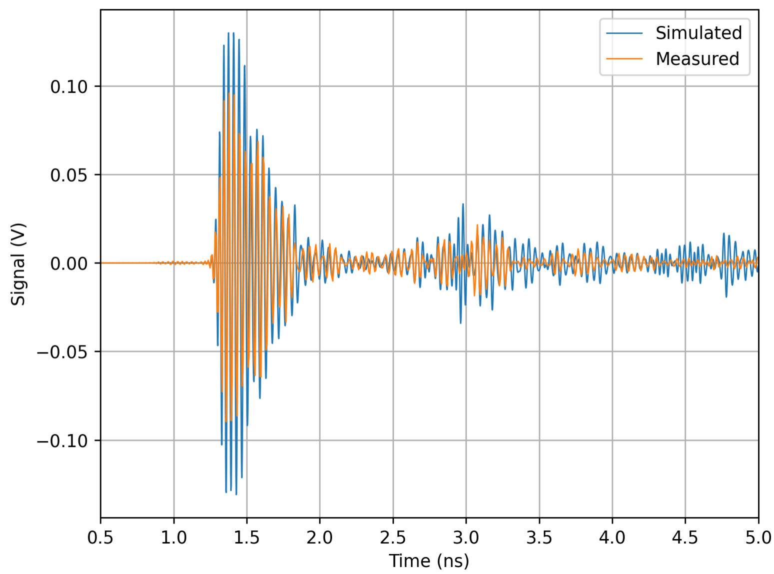

Figure 4.52: Plot of measured and simulated time-domain response of the alumina target excited via a slab line. The signal goes through a fused quartz transition, a short WR28 waveguide piece and a HP R281A waveguide-to-coaxial adapter.

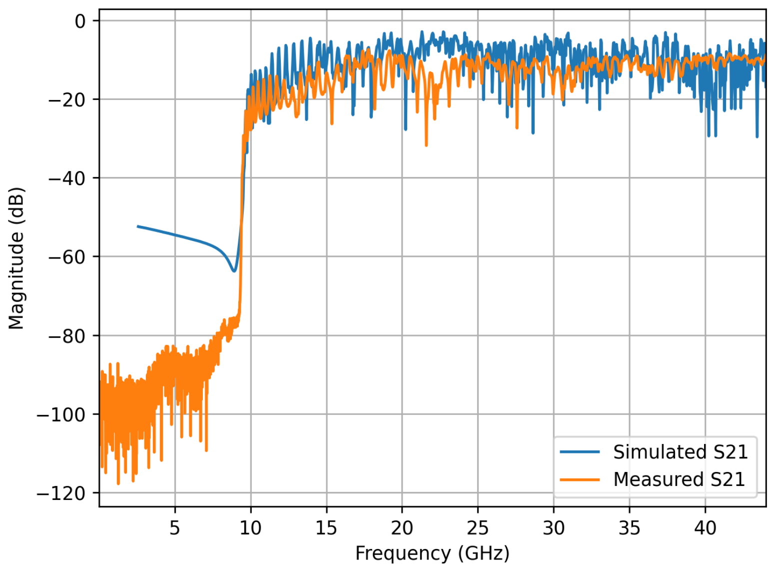

Figure 4.53: Plot of measured and simulated |S21| vs. frequency for the alumina target excited via a slab line. The output signal of the alumina is measured with a circular dielectric-loaded waveguide-to-coaxial adapter.

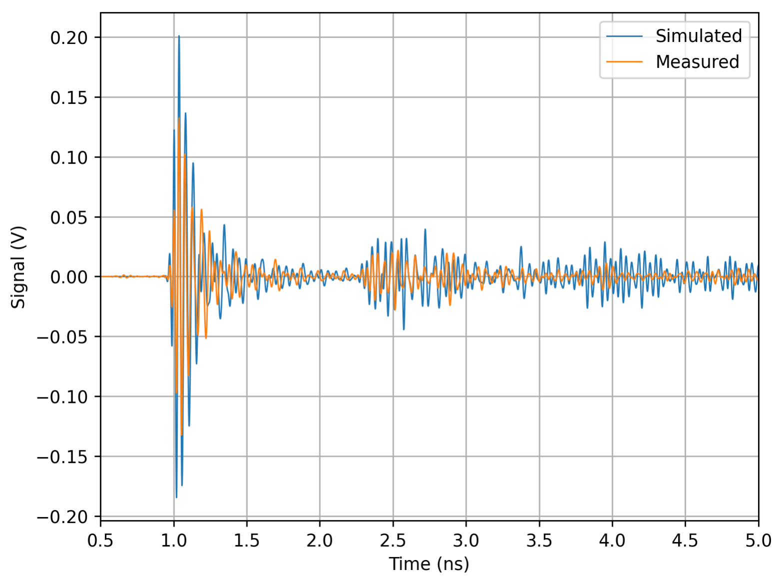

Figure 4.54: Plot of measured and simulated time-domain response of the alumina target excited via a slab line. The output signal of the alumina is measured with a circular dielectric-loaded waveguide-to-coaxial adapter.

4.3 Conclusions

This chapter studied the effect of different target shapes and sizes on the characteristics of the emitted ChDR. The numerical analysis revealed that the direction and amount of ChDR emitted for the same dielectric material and similar surface area exposed to the beam field does not change significantly for different target shapes. Therefore, a cylindrical target was chosen due to ease of manufacturing.

For the specific application of the ChDR BPM at AWAKE a variety of constraints had to be included in the ChDR design. These included the compatibility of the target with the geometry of the existing pBPM bodies. This dictated the type of material that was chosen as a large ChDR angle was required to fit the geometrical requirement. Hence, alumina with $\varepsilon_r = 9.9$ and $\theta_{Ch} = 71^\circ$ was chosen. Another requirement was to restrict the frequency content passing through the target to frequencies higher than several GHz in order to suppress the beam field from the proton beam, so that the ChDR BPM would be insensitive to the proton bunches. This dictated the diameter of the cylindrical target. Given the manufacturing limitations and reduced output power at smaller target diameters as shown by the numerical simulations in Section 4.1.6, a diameter of $6\,\mathrm{mm}$ was chosen with a cut-off frequency of $9.3\,\mathrm{GHz}$. The length was also maintained as short as possible to minimise the number of internal reflections of the DR generated by the edge of the target. A full 3D simulation was then performed with the chosen target material and dimensions in CST Wakefield solver presented in Section 4.1.7. The output voltage level with the electron beam parameters similar to those at AWAKE showed very comfortable signal amplitudes of several tens of volts. With the inclusion of a band-pass filter of $30\,\mathrm{GHz}$ centre frequency and $300\,\mathrm{MHz}$ bandwidth, the output signal level was still a few hundred milli-volt. Based on the position sensitivity found by the numerical analysis and the theoretical in-band noise level, the maximum achievable position resolution of the ChDR BPM was estimated to be $9\,\mu\mathrm{m}$.

Different types of transitions following the exit of the alumina target were also studied numerically. These included a dielectric-loaded circular-WG to rectangular-WG transition in Section 4.1.8, which improved the theoretical position resolution from $9\,\mu\mathrm{m}$ to $6\,\mu\mathrm{m}$ (when including a $30\,\mathrm{GHz}$ centre frequency and $300\,\mathrm{MHz}$ BW filter), and a dielectric-loaded circular WG-to-coaxial adapter in Section 4.1.9 which, unlike the WR28 rectangular WG transmission line with a cutoff frequency of $21.1\,\mathrm{GHz}$, provides signal transmission above $9.3\,\mathrm{GHz}$, i.e. the cut-off frequency of the alumina target.

Section 4.2 detailed the theory and design of a test-bench for RF characterisation of the ChDR target. This involved a so-called slab line, consisting of two ground planes and a central conducting rod, with dimensions chosen to match the characteristic impedance of the coaxial lines connected to the VNA. The VNA performed a frequency sweep up to $44\,\mathrm{GHz}$ which provided the frequency response of the ChDR target in the range of interest, and with an in-built iFFT function, the time-domain response was also measured. These measurements were done for the various set-ups that were studied numerically. The RF measurements provided a full characterisation of the ChDR target and a verification of the numerical simulations.

5 Beam studies at AWAKE and CLEAR

The previous chapter showed the design process and the verification of the numerical simulations with RF characterisation of the ChDR BPM target. This chapter will present the experimental results from parasitic tests with proton and electron-beams at AWAKE, and dedicated electron-beam studies at the CLEAR test facility. These include charge scans and beam position scans with various signal processing chains and at different detection frequencies.

5.1 Mechanical design of the ChDR BPMs for AWAKE and CLEAR

In total, 10 ChDR radiators were manufactured based on the design presented in the previous chapter. Two ChDR BPMs, which utilised 8 radiators, were installed in the AWAKE common beam-line and one plane of a ChDR BPM, which utilised the remaining 2 radiators, was installed at the CLEAR test facility. The technical drawings created with the aid of the Mechanical and Materials Engineering (MME) group at CERN are shown in Figures 5.1, 5.2, 5.3 and 5.4 [90], where the corresponding item names and materials are given in Table 5.1. The ChDR alumina (Al_2O_3 ceramic) rods were coated with a $15 - 35$ µm thick Mo-Mn-silica compound, and finished with a $2 - 5$ µm conductive Ni layer. They were then brazed to the collars (item number 3 in Figure 5.1) which were then welded to the ChDR target housing (Figure 5.1). These were inserted into the main ChDR BPM body for AWAKE, as shown in Figure 5.3, and for CLEAR, as shown in

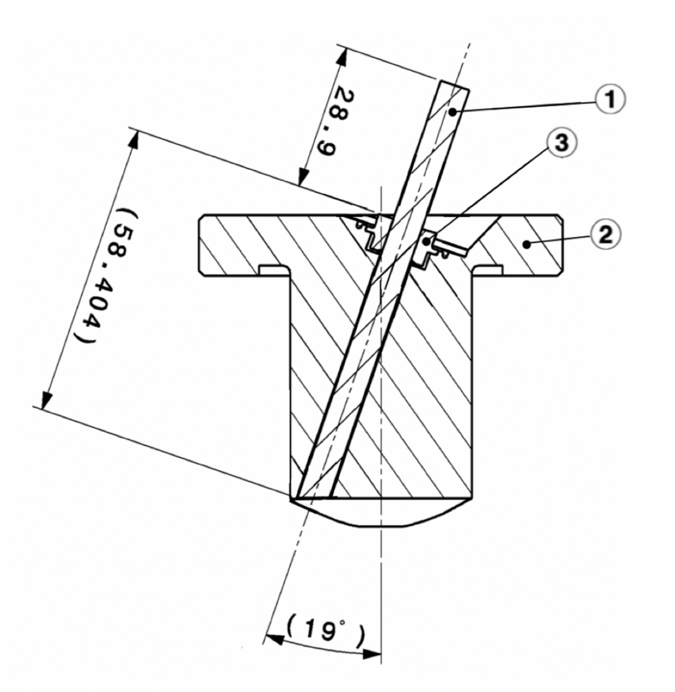

Figure 5.1: Mechanical drawing of the ChDR target housing with one $6\,\mathrm{mm}$ diameter alumina target inside [90].

Figure 5.4. Figure 5.5 shows the CLEAR ChDR BPM targets and housing as a 3D schematic (left) in its body (middle) prior to installation (right).

Table 5.1: Names and materials of the components of the ChDR BPM at AWAKE and CLEAR.

Item number	Item name	Material
1	6 mm-diameter radiator	Metalized ceramic Al_2O_3
2	DN40 flange	Stainless steel
3	Collar for brazing	Stainless steel
4	ChDR BPM body for CLEAR	Stainless steel
5	ChDR BPM body for AWAKE	Aluminium
6	60/63 mm-diameter flange	Stainless steel

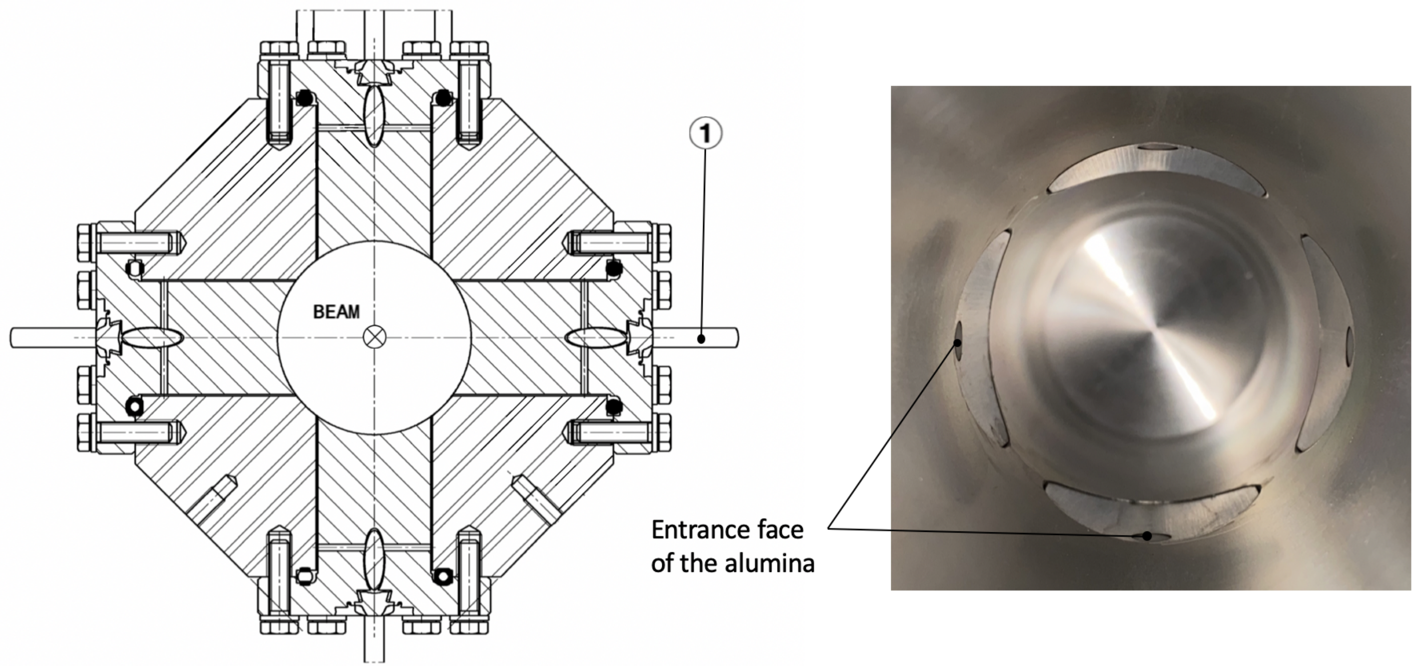

Figure 5.2: Mechanical drawing of the ChDR BPM for AWAKE as a cross-section (left) [90] and a photo from the inside of the ChDR BPM for AWAKE (right).

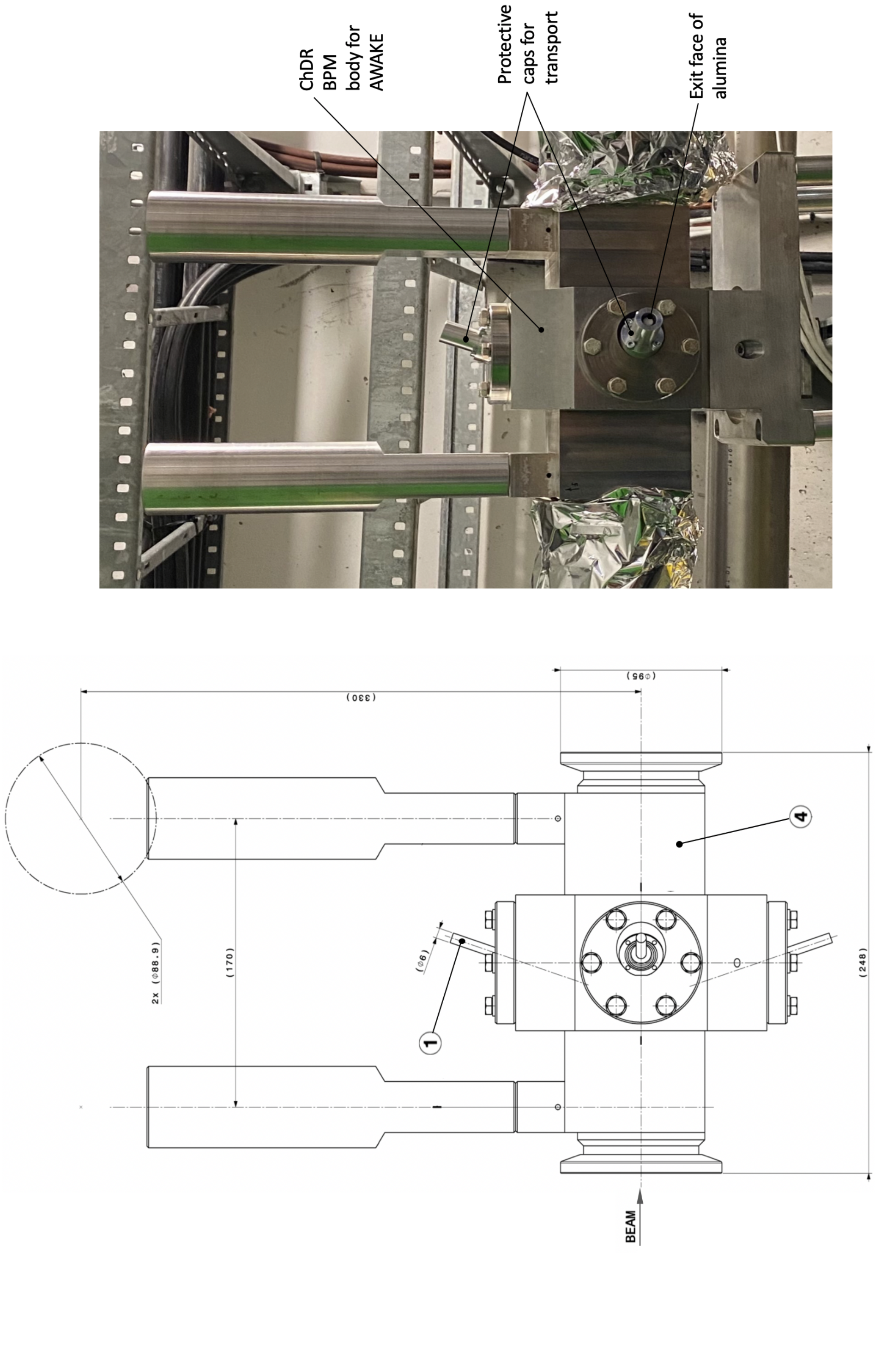

Figure 5.3: Mechanical drawing of the ChDR BPM for AWAKE (left) [90] and a photo of the ChDR BPM for AWAKE in the AWAKE common beam-line (right).

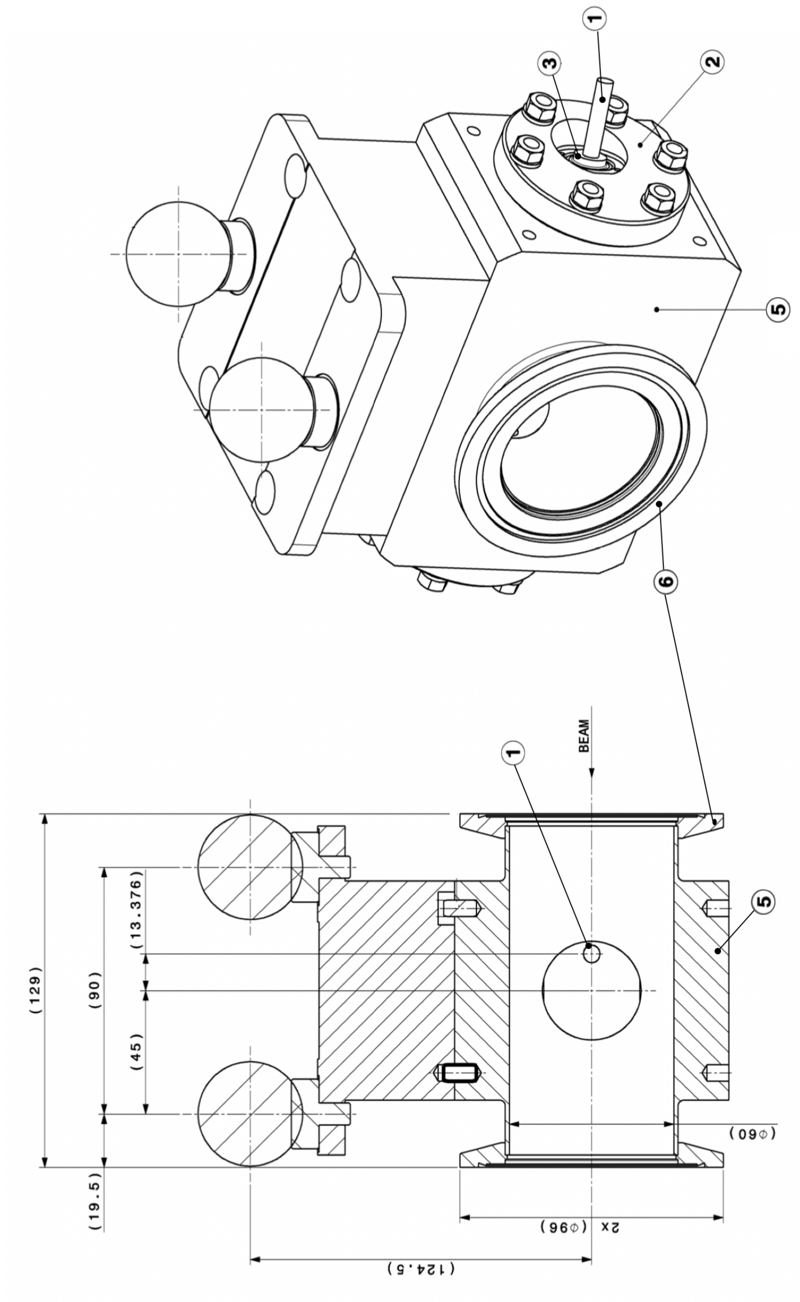

Figure 5.4: Mechanical drawing of the ChDR BPM for CLEAR [90].

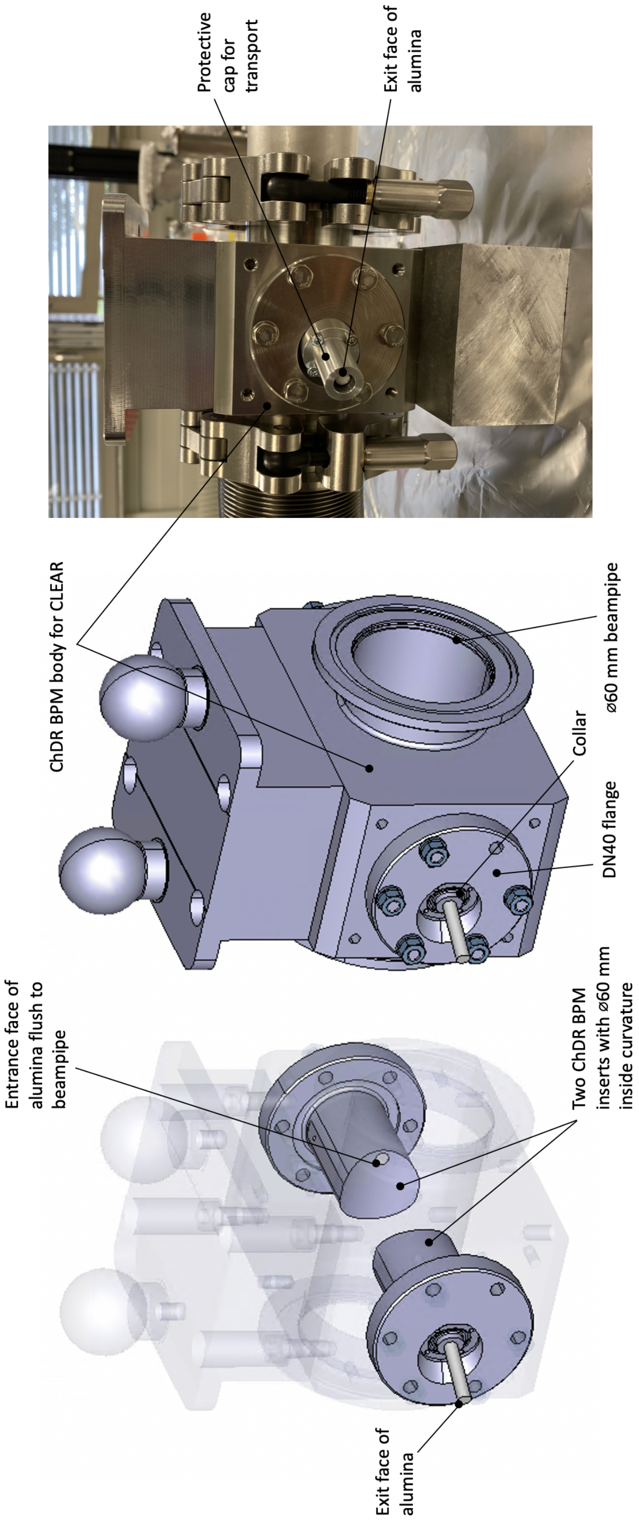

Figure 5.5: 3D rendering of the ChDR BPM inserts (left) and full BPM assembly (middle), and a photo of the ChDR BPM prior to installation (right).

5.2 Beam tests at AWAKE

Two ChDR BPMs were installed at AWAKE (Fig. 5.3) at a distance of $2.64\,\mathrm{m}$ apart. Only the horizontal plane of the ChDR BPM further from the plasma cell was tested due to limitations in the availability of RF components in the detection frequency band of interest, which was between 26.5 and $40\,\mathrm{GHz}$ (Ka-band). The signal detection chain (Fig. 5.6) following the alumina radiator and circular dielectric-loaded waveguide to WR28 waveguide transition consists of an approximately $1.5\,\mathrm{m}$ long set of WR28 rectangular waveguides (straight sections and bends), followed by WR28 waveguide components and a base-band detection system:

- Band-pass filter with $30\,\mathrm{GHz}$ central frequency and $300\,\mathrm{MHz}$ $3\,\mathrm{dB}$-bandwidth
- $0-60\,\mathrm{dB}$ remotely controlled variable attenuator (MI-WAVE, model 511A), used to control the input power to the detector
- Zero-bias Schottky-diode detector with WR28 waveguide input and $3.5\,\mathrm{mm}$ (SMA) coaxial output (Millitech Inc., DXP-28)
- $6\,\mathrm{GHz}$ oscilloscope (Tektronix, MSO6), located outside of the AWAKE tunnel to record the detected waveforms.

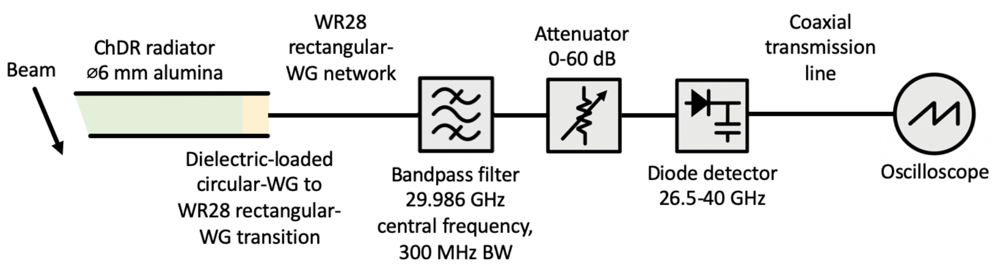

Figure 5.6: Schematic of the detection chain used at AWAKE.

Since the AWAKE experiment runs for several weeks throughout the year with high intensity proton bunches fed by the SPS, the beam time is mainly dedicated to physics studies of PWFA. However, parasitic measurements with the above mentioned set-up of the ChDR BPM were taken in April 2022 with electrons and protons individually, and with both beams simultaneously. Measurements were taken for two proton bunch populations, 1×10^{11} protons ($\equiv 16\,\mathrm{nC}$ bunch charge) and 3×10^{11} protons ($\equiv 48\,\mathrm{nC}$ bunch charge). Fig. 5.7 shows the signal waveform for a single event recorded on the oscilloscope for one of the horizontal radiators for three particle beam configurations; electron bunches only, proton bunches only and both beam bunches simultaneously. The proton bunch charge was $16\,\mathrm{nC}$ and the electron bunch charge was $250\,\mathrm{pC}$. The variable attenuator was set to $10\,\mathrm{dB}$ for the cases where the electron bunches were present (blue and orange traces), and $0\,\mathrm{dB}$ for the *protons only* green trace. When only the protons

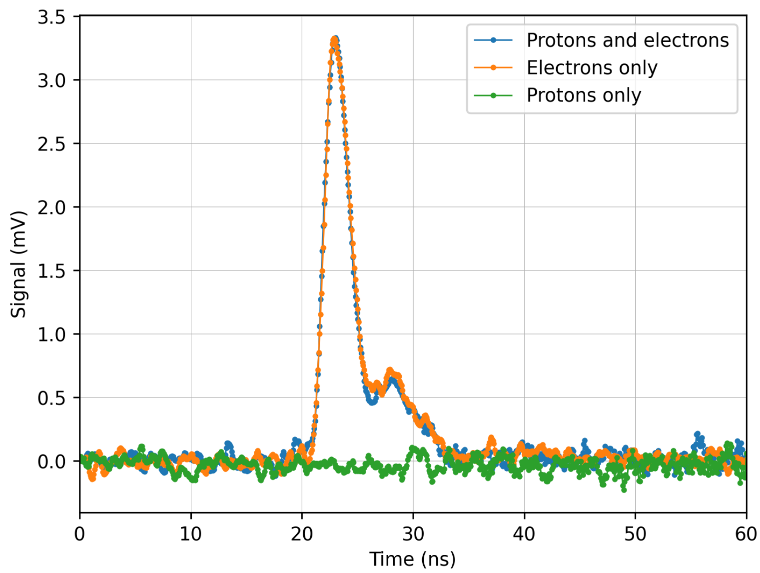

Figure 5.7: Plot of a single event of the detected signal waveform versus time for one of the horizontal radiators for three different beam configurations; electrons only, protons only and both bunched beams simultaneously.

were present, no signal was detected by the ChDR BPM (green trace). With only the electron bunches present, as well as with both bunched beams present, the signal shape and level remained the same (orange and blue traces). Therefore, the alumina radiators successfully suppressed the lower frequency signal components of the high intensity proton bunch signal (with $16\,\mathrm{nC}$ proton bunch charge), while successfully detecting the high frequency signal contents of the electrons with a bunch charge of $250\,\mathrm{pC}$.

Fig. 5.8 presents the detected signal waveform on the oscilloscope for the three different beam configurations, but now for a higher intensity proton bunch charge of $48\,\mathrm{nC}$. The read-out system configuration and the setting of the attenuator was the same as in the previous experiment with $16\,\mathrm{nC}$ proton bunch charge. It was observed, when operating with this high proton bunch charge, that some residual

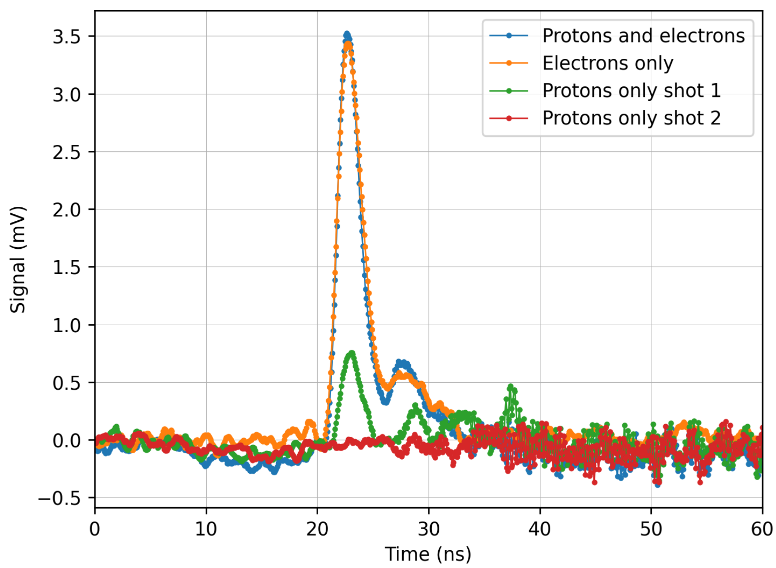

Figure 5.8: Plot of a single event of the detected waveform versus time of the ChDR signal pulse for one of the horizontal radiators for three different beam configurations; electrons only, protons only and both bunched beams simultaneously.

proton signal was detected, but with large shot-to-shot fluctuations in waveform shape and level. As an example, Fig. 5.8 shows two oscilloscope acquisitions when only the proton bunches were present, one showing no signal at all (red trace), the other some residual proton signal (green trace). This indicates that the spectrum of the proton bunches arriving from the SPS has a large shot-to-shot variability and for some shots extends to frequencies higher than the $30\,\mathrm{GHz}$ detection frequency. At present, there is no way to reliably measure the longitudinal proton bunch particle distribution to these high frequencies at AWAKE. It was, therefore, important to revisit the chosen detection frequency of $30\,\mathrm{GHz}$ and investigate possible alternatives, also at even higher frequencies. Although the initial tests performed at AWAKE provided valuable information about the response of the ChDR BPM to various beam configurations, a more systematic study at different detection frequencies was carried out at the CLEAR beam test facility with a dedicated electron beam. This will be discussed in the following section.

5.3 Beam studies at CLEAR

The experimental campaign at CLEAR involved measuring the ChDR from the alumina radiators at three different frequency ranges with waveguide Schottky diode detectors, all comprising a rectangular waveguide input and a coaxial output. The first measurements were performed in the lowest frequency range between 26.5 and $40\,\mathrm{GHz}$ (Ka-band, using WR28 type waveguide components). This was tested with a horn antenna connected to a commercial WR28 rectangular-waveguide $10\,\mathrm{dB}$ fixed attenuator, followed by a diode detector of the same waveguide type input and coaxial output. Another configuration was tested in this frequency range where the horn antenna was omitted and the output of the alumina was connected directly to the WR28 waveguide attenuator in view of systematically approaching the set-up used at AWAKE. In the case of the lowest detection frequency range, both alumina radiators were measured simultaneously utilizing independent, symmetric set-ups. The other two measured frequency ranges were $50 - 75$ GHz (V-band, using WR15 type waveguide components) and $75 - 110$ GHz (W-band, using WR10 type waveguide components). Both of these were tested with an appropriate horn antenna connected to a diode detector with respectively a WR15 or WR10 rectangular waveguide input, and a coaxial output. In these two frequency ranges only one of the two alumina radiators was measured due to the limited availability of RF components.

It is worth noting that the Ka-, V- and W-band frequency ranges are defined for the lowest TE10-mode in the corresponding rectangular waveguide type. The actual measurement frequency range may include an *over-moded* situation. For example, while the Ka-band detection system is defined in the frequency range $26.5 - 40$ GHz, in practice it exceeds this range i.e. it passes, and to some extent also detects frequencies above $40\,\mathrm{GHz}$ for the TE10 and the next higher-order modes (TE01, TE20) simultaneously.

In this section, the results from the rectangular waveguide detection chains (WR28, WR15 and WR10) will be presented and discussed.

5.3.1 Overview of the CLEAR test facility

CLEAR is a user test facility located at CERN delivering single and multi-electron-bunch trains with nominal parameters shown in Table 5.2 [91]. It is divided into two main sections; a $20\,\mathrm{m}$ long injector beam-line where the beam is conditioned to the required parameters and a $16\,\mathrm{m}$ long experimental beam-line where the majority of the user experiments are located. A schematic of the CLEAR beam-line

Table 5.2: Nominal electron beam parameters delivered to the experimental beam-line at CLEAR [91].

Beam parameter	Value
Energy	60-220 MeV
Bunch charge	0.01-2 nC
Bunch length	1-4 ps
Repetition rate	0.83-10 Hz
Bunch frequency	1.5 GHz
RF frequency	3 GHz
RMS energy spread	<0.2 %
Number of bunches in a train	1-200

is shown in Fig. 5.9. The injector beam-line begins with the RF gun where a pulsed UV laser with a frequency of $1.5\,\mathrm{GHz}$ hits a Cs_2Te photocathode to produce the electron bunches that are accelerated to $5\,\mathrm{MeV}$. The RF gun is then followed by three accelerating cavities that bring the energy of the electron beam to the nominal range of $60 - 220\ \mathrm{MeV}$. Close to the end of the injector beam-line there is an RF deflecting cavity (RFD) used to make bunch length measurements and a dipole magnet for measuring the beam energy. The experimental beam-line holds the majority of the user experiments, including those installed in-vacuum and in-air. Along the entire beam-line there are various beam diagnostic instruments for measuring the properties of the electron beam. These include integrated current transformers (ICT) for measuring the bunch charge, several beam television (BTV) screens for measuring the bunch transverse sizes, and a number of inductive BPMs for beam position measurements.

The ChDR BPM was installed approximately $7\,\mathrm{m}$ upstream of the in-air test stand (Fig. 5.10) and is located between several beam diagnostic instruments including two BTVs (620 and 730) and two inductive BPMs (595 and 690). A few corrector dipole magnets also exist before and after the ChDR BPM (DHJ 540, 590 and 710).

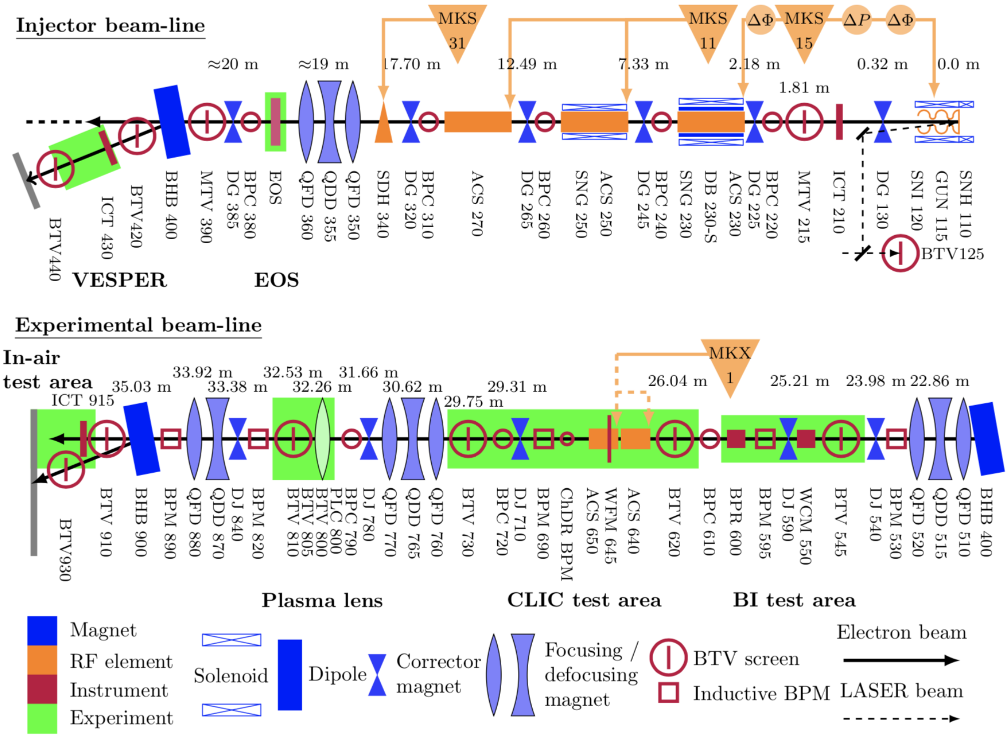

Figure 5.9: Schematic of the CLEAR beam-line, divided into the injector beam-line (top) and the experimental beam-line (bottom) [92].

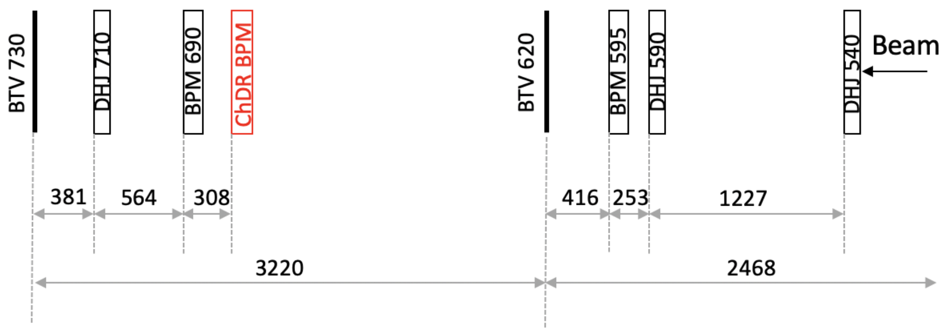

Figure 5.10: Schematic of a section of the CLEAR beam-line where the ChDR BPM is located and the surrounding components. All dimensions are given in mm.

5.3.2 Set-up of the detection chain for the Ka-band measurements

As previously mentioned, the commercial WR28 rectangular waveguide operates in the fundamental TE10-mode in the Ka-band ($26.5 - 40$ GHz), and was chosen to transmit the signal from the exit of the alumina to the detector. Two different set-ups to couple the signal from the exit of the alumina to the WR28 waveguide were tested, one via a horn antenna, the other via direct waveguide connection. Schematics for their signal detection chains are shown in Figures 5.11a and 5.11b.

The first of these read-out set-ups is shown in Figure 5.12 for the left side of the two alumina radiators. The opposite right side alumina radiator was equipped with the same set-up. Since the polarisation of the field exiting the alumina is determined by the TEM-like field of the beam, the horn antenna was oriented with

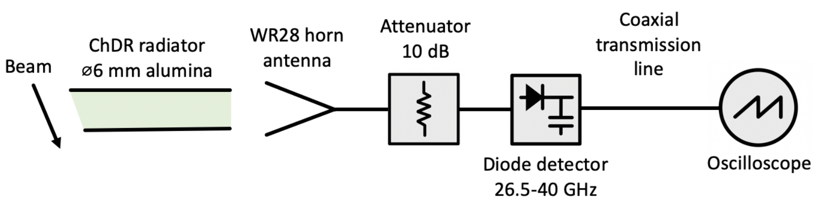

(a) with a waveguide horn antenna at the exit of the alumina.

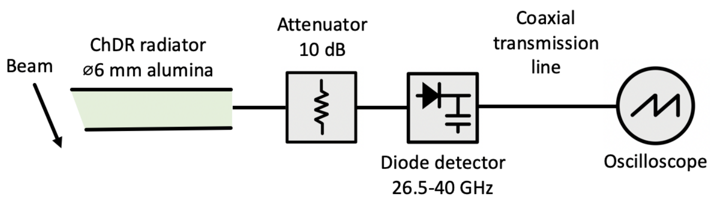

(b) with a direct waveguide connection at the exit of the alumina.

Figure 5.11: Schematics of the Ka-band signal detection chain

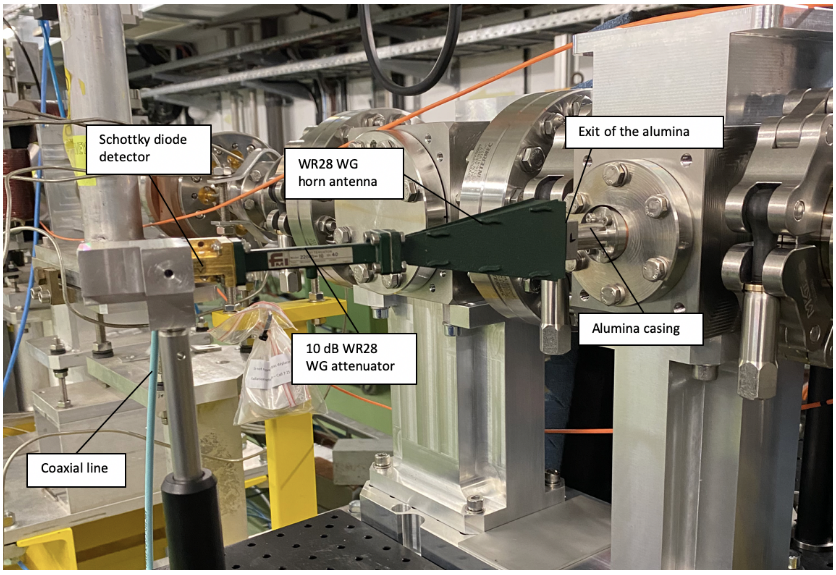

(a) Left read-out arm (when looking downstream) of the ChDR BPM at CLEAR, with the signal processing chain including the horn antenna, rectangular WG attenuator, Schottky diode detector and coaxial cable which transmits the detected signal to an oscilloscope outside of the tunnel.

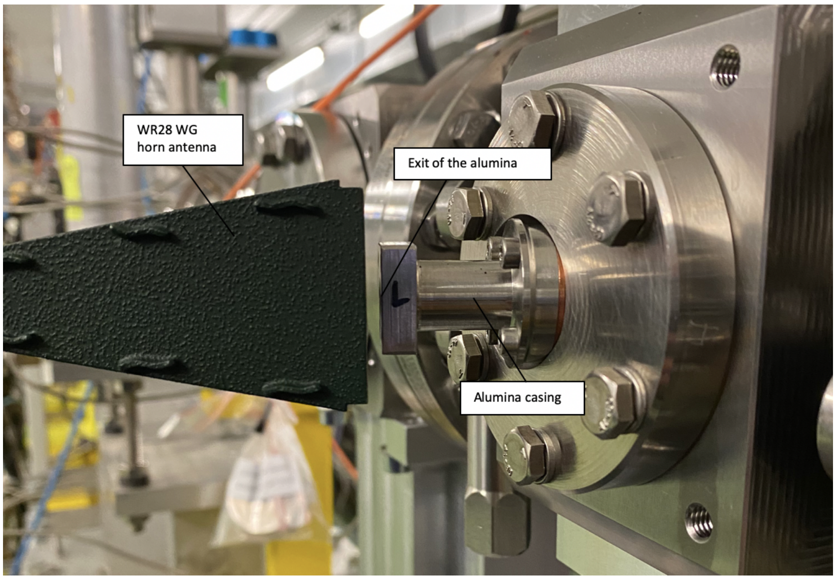

(b) Exit of the alumina target and the positioning of the horn antenna.

Figure 5.12: Photos of the ChDR BPM set-up at CLEAR with Ka-band ($26.5 - 40$ GHz) detection chain using horn antennas.

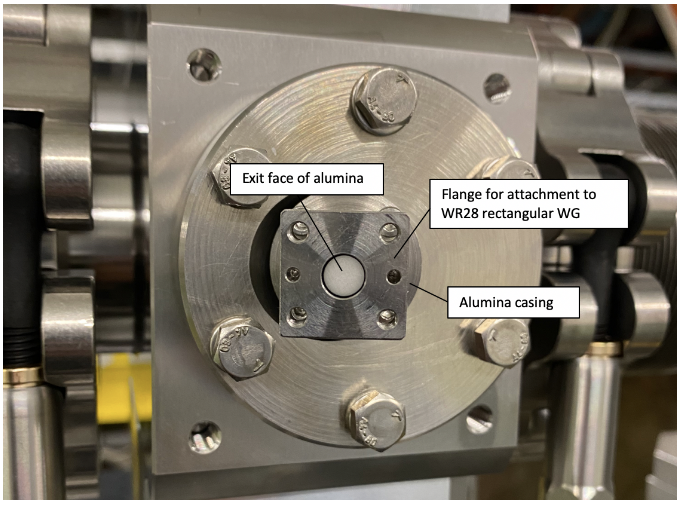

(a) Exit face of one of the two alumina targets.

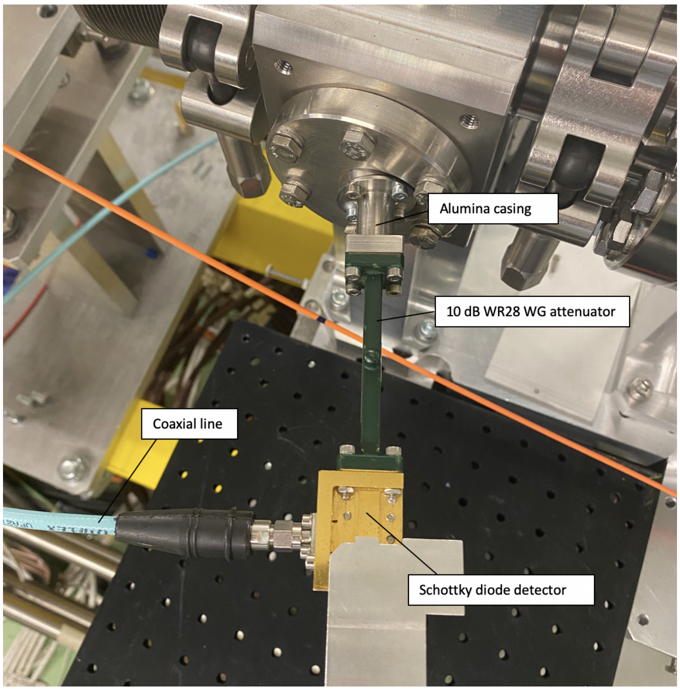

(b) Signal detection chain in the Ka-band with the $10\,\mathrm{dB}$ WG attenuator directly connected to the exit of the alumina.

Figure 5.13: Photos of the ChDR BPM set-up at CLEAR with Ka-band $(26.5-40\text{ GHz})$ detection chain using a direct waveguide connection between the exit of the alumina and the WR28 WG attenuator.

its long axis perpendicular to the direction of particle beam travel. The casing of the alumina rod was used to aid the alignment of the horn antenna. The horn antenna was directly attached to a WR28 rectangular WG $10\,\mathrm{dB}$ fixed attenuator, which was attached to a zero-bias Schottky diode detector. The WG attenuator was used to reduce the power entering the detector to prevent risk of damage. A coaxial line transmitted the output signal of the detector to an oscilloscope with $6\,\mathrm{GHz}$ analog bandwidth, and a sampling rate of $25\,\mathrm{GS/s}$, located outside of the CLEAR tunnel.

A different set-up was also tested, which involved a direct connection between the exit face of the alumina target and the WR28 WG attenuator. This is shown in Fig. 5.13, and was tested to approach the same set-up that was used at AWAKE.

5.3.3 The Schottky diode detector

Commercial RF zero-bias waveguide Schottky diode detectors were used to measure the signal from the ChDR BPM. These WG detectors are physically advantageous for this application because they have a rectangular waveguide input and a coaxial output. The diode detector rectifies the input signal so that the output signal represents the positive or negative envelope of the RF input waveform, i.e. the *base-band* signal. The frequency content, as well as any phase information of the RF input signal is lost by this operation.

The output voltage V_{out} of the diode detector is related to the input power P_{in} via [93]

$$V_{out} = K(\sqrt{P_{in}})^{\alpha}, \tag{5.1}$$

where K is a constant and $\sqrt{P_{in}}$ is proportional to the input voltage of the detector V_{in}. Below a certain input power level, $\alpha \approx 2$, which is the so-called *square-law* regime; the output voltage of the detector V_{out} is proportional to the

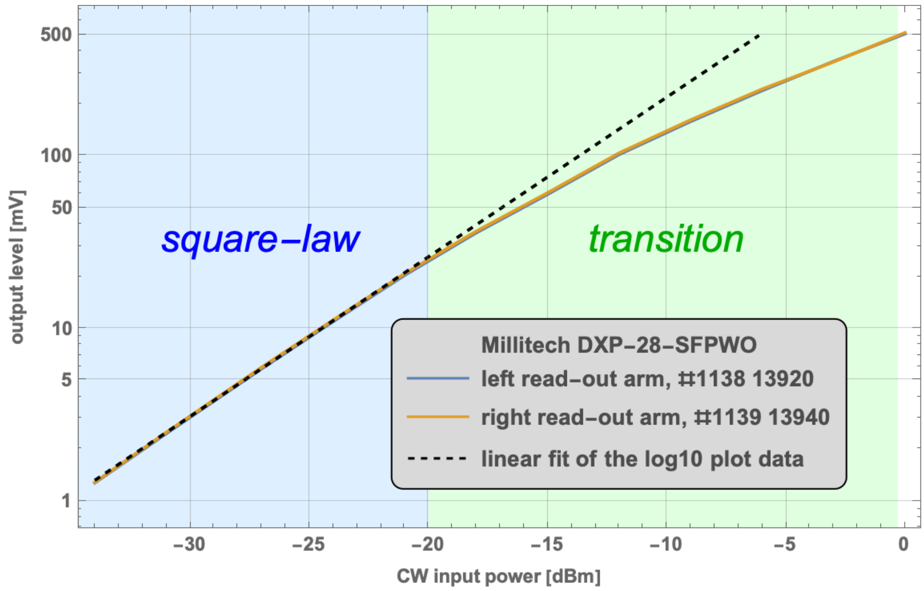

Figure 5.14: Measured Schottky detectors, Millitech type DXP-28-SPFWO.

input power P_{in} which is proportional to V_{in}^2. Fig. 5.14 shows the measured characteristic of the two WR28 Schottky detectors used for the Ka-band beam tests, performed with a continuous wave (CW) sinusoidal RF signal of $f = 30\,\mathrm{GHz}$ at the input and the high impedance $(100\,\mathrm{k\Omega})$ load of a voltmeter at the output. At RF power levels $P_{in} \lesssim -20\,\mathrm{dBm}$ they operate in the square-law regime. Since the bunch charge is proportional to the input voltage of the detector V_{in}, the output voltage of the detector V_{out} is expected to be proportional to the square of the bunch charge in this square-law regime. In other words, the square-root of the output voltage of the detector is proportional to the bunch charge $\sqrt{V_{out}} \propto Ne$, where N is the number of particles in the bunch and e is the unit of elementary charge. For $P_{in} \gtrsim -20\,\mathrm{dBm}$ the diode response *transitions* from the square-law to the linear (vs. input voltage) regime, and for even higher input power levels, $P_{in} \gtrsim 0\,\mathrm{dBm}$, the diode goes into the linear, “peak detecting” regime. It is advantageous to operate the diodes in the square-law regime, which gives a linear response of the output voltage to the input power, in order to reduce the complexity of the data post processing since no special non-linear corrections are required. Terminating the output of the diode with the $50\,\Omega$ load impedance of an oscilloscope results in a high video bandwidth of $\sim 1\,\mathrm{GHz}$, meaning the detected output envelope follows changes of the input signal with rise/fall-times of $\sim 350\,\mathrm{ps}$.

5.3.4 Measurement procedure

The key measurements that were performed with the ChDR BPM for different signal processing chains involved a bunch charge scan and a series of beam position scans. The bunch charge scan was an important measurement to provide the bunch intensity region where the detectors are operating in the square-law regime. For the beam position scans, the measured signal was kept below the threshold separating the square-law and the transition region of the diode response.

A typical measurement procedure started by setting and verifying the bunch length and charge via the RFD and ICT at the beginning of the injector line. Once these parameters were set, the beam was transported to the experimental beam-line where the ChDR BPM is located. A loss-free transport was checked via the second ICT located at the end of the experimental beam-line. The bunch charge was then increased and with zero current in the corrector magnets DHJ 590 and 710. The beam was centred by adjusting corrector magnet DHJ 540, while observing the beam position at the inductive BPMs 595 and 690, see also Fig. 5.10. This provided a ballistic beam from the location of magnet DHJ 540 down to the screen monitor BTV 730. Now the screen of BTV 730 was inserted and the reference position for a centred beam was recorded. The bunch charge was then scanned and the readings from the ICT and oscilloscope of the ChDR BPM were recorded, both at the beam repetition rate of $10\,\mathrm{Hz}$. 100 consecutive oscilloscope signal waveforms were taken for each bunch charge setting. In the following signal post-processing, the peak of the detected signal waveform from each oscilloscope shot was extracted, then averaged for each bunch charge and these values were then square-rooted to clearly identify the square-law region of the diode detector. The bunch charge was then adjusted to a value well below the threshold with some margin for the beam position scans.

After completing the beam setup, a beam position scan was performed by adjusting the current in corrector magnet DHJ 540. Again, 100 consecutive oscilloscope waveforms were recorded at each beam position setting. The beam position on the screen of BTV 730 was recorded as reference via a data acquisition script provided by CLEAR, since the inductive BPMs proved to be inaccurate at low bunch charge. The expected beam position at the location of the ChDR BPM was then calculated by considering the distances between the various components and by taking the error on each distance measurement as $10\,\mathrm{mm}$, with the result that a $1\,\mathrm{mm}$ beam displacement on the BTV 730 screen corresponds to a $(0.75 \pm 0.01)\,\mathrm{mm}$ displacement at the location of the ChDR BPM where the error has been propagated from the distance measurements. This same position scan procedure was then repeated for different signal processing chains and detection frequency ranges. Although a small angle is introduced in the beam trajectory by the corrector magnet DHJ 540 at each beam position of the scan, the impact parameter is considered to be constant along the entrance face of the radiator due to the small diameter of the radiator in comparison to the distances between the instruments of interest. However, for larger radiators and angles of beam trajectory, this effect may be significant and would need to be accounted for, or the beam would need to be directed on a parallel trajectory wrt. the entrance face of the radiator.

5.3.5 Bunch charge scan results

An example of the signals from the oscilloscope using the Ka-band detection chain with the horn antenna is shown in Fig. 5.15 for a centred beam with $1\,\mathrm{ps}$ RMS bunch length, $155\,\mathrm{MeV}$ energy and $45\,\mathrm{pC}$ bunch charge. The orange trace shows the signal from the left read-out arm of the ChDR BPM, when looking downstream, and the blue trace shows the signal from the right arm. At approximately $1\,\mathrm{ns}$, the electron bunch passes the ChDR BPM and is detected. Not only do the signals show a good symmetry between the two arms, the rise time observed in the detected time domain signal is in the $t_r \approx 100\,\mathrm{ps}$ regime, meaning the video bandwidth of the entire detection system, including dispersion effects of the cables and bandwidth of the oscilloscope, is much higher than expected from the

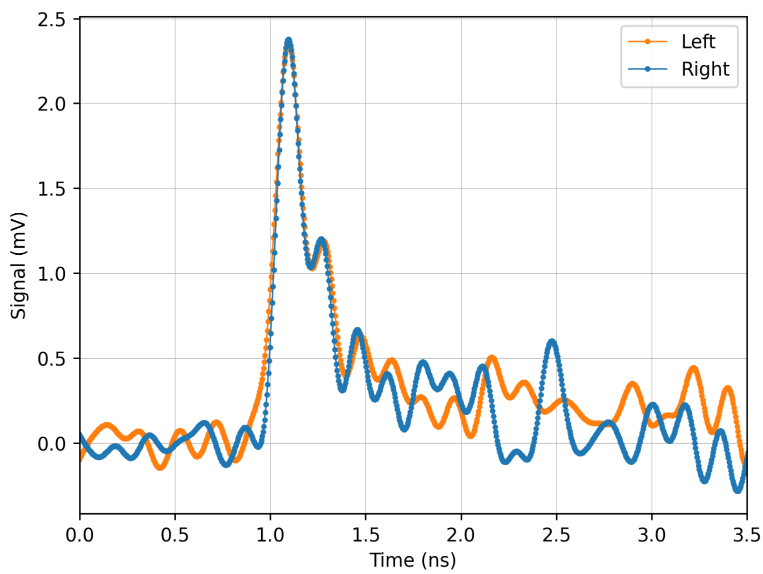

Figure 5.15: Plot of the measured oscilloscope signals (single shot) of the left and right ChDR BPM radiators versus time for a $155\,\mathrm{MeV}$, $45\,\mathrm{pC}$ bunch. The detection chains involve two waveguide horn antennas in the Ka-band with nominal detection frequency range of $26.5 - 40$ GHz.

manufacturer's datasheet of the WG diode detectors ($t_r \approx 350\,\mathrm{ps}$). This allows one to better resolve details in the time domain response of the ChDR radiator and its detection system.

The bunch charge was scanned from 25 to $280\,\mathrm{pC}$ using the ICT as a reference and the traces on the oscilloscope from both read-out arms were recorded. Trace-by-trace, the peak voltage of the waveform of each arm was obtained in the post-processing analysis. The maxima of the first peak was used since this is the main signal peak that is detected from the passage of the beam next to the radiator and is symmetric across both arms. The peaks that follow i.e. after approximately $1.4\,\mathrm{ns}$ are due to unknown reflection effects that vary shot-to-shot and are not symmetric across the arms. Integrating the first peak over a short window either side of the maxima, and within the first peak, also produces a similar result as was checked in the post-processing analysis. The average of the peak voltages was then calculated at each bunch charge setting with the error being the standard error, which is due to shot-to-shot fluctuations of the machine parameters. The square-root of the average peak voltages was then calculated and the errors were propagated from the errors in the average peak voltages.

The shot-to-shot logging of the bunch charge done at CLEAR, using the ICT, is imperfect and sometimes misses shots when the machine is operated at the high repetition rate of $10\,\mathrm{Hz}$. Due to this imperfect synchronisation between the logged bunch charge data on the control system and the data from the oscilloscope, the average charge was calculated for each bunch charge setting with the error being the standard error.

The square-root of the peak voltages of both arms averaged across 100 shots for each bunch charge setting is plotted against the average bunch charge in Fig. 5.16. The plot again shows a good symmetry between the left and right read-out arms,

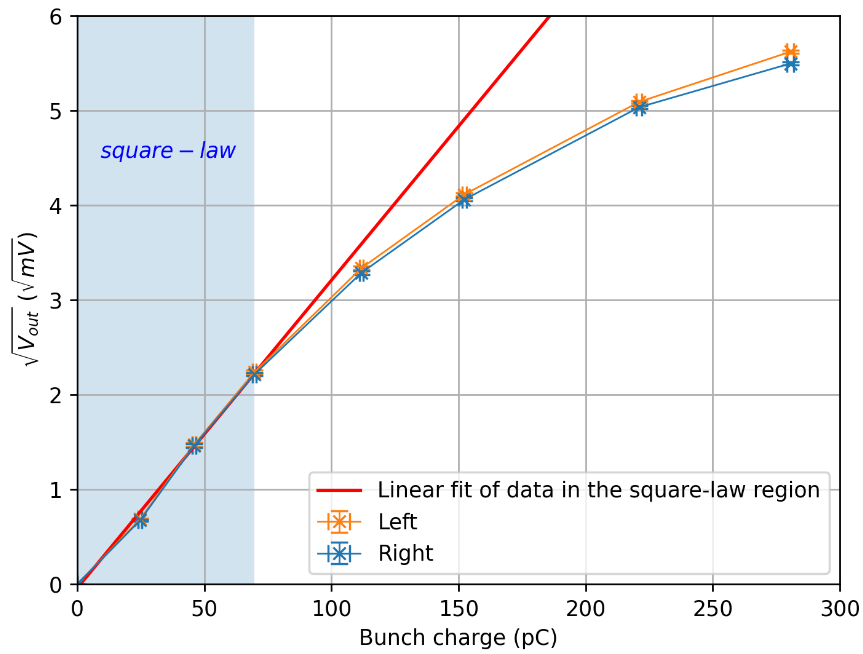

Figure 5.16: Plot of the square-root of the averaged peak output voltages versus the averaged bunch charge.

and gives the ChDR BPM response vs. bunch charge. Below approximately $70\,\mathrm{pC}$, the detector response is in the square-law regime where the square-root of the output voltage of the detector $\sqrt{V_{out}}$, which is proportional to the input voltage of the detector V_{in}, is proportional to the bunch charge Ne.

5.3.6 Beam position scan results

Prior to the beam position scan, the bunch charge was reduced to less than $70\,\mathrm{pC}$, so that the diodes always operated in the square-law regime. The beam position was then scanned between a range of $\pm 5\,\mathrm{mm}$ on the BTV 730 screen by adjusting the current in the corrector magnet DHJ 540. This corresponds to a range of $\pm 3.75\,\mathrm{mm}$ at the location of the ChDR BPM. The position of the beam on the screen was displayed at a rate of $0.83\,\mathrm{Hz}$ via a script developed by the CLEAR operations team. This script performed Gaussian fits to the horizontal and vertical beam profiles, and took the location of the maxima as the respective beam position. The beam position stability was verified on the CLEAR control displays prior to the beam measurement campaign, during which the position on the screen was recorded with the error being half of the pixel size of the imagining system, which is $0.16\,\mathrm{mm}$. The error of the scaling factor $(0.75 \pm 0.01)\,\mathrm{mm}$ has a negligible effect on the error of the position measurement when propagated through. For each oscilloscope acquisition, a signal post-processing was performed, extracting the difference divided by the sum of the square-root of the peak values of the left and right arm signals from the two ChDR radiators. This ensured a charge-normalised beam position signal. The average difference-over-sum was then calculated for the 100 shots for each beam position setting, with the uncertainty taken as the standard error. Fig. 5.17 shows these averaged difference-over-sum results plotted against the horizontal beam position given by the screen monitor for the Ka-band detection chain using the horn antennas (in red). As predicted by numerical simulations, the response is linear in this beam position range. The sensitivity, given by the gradient of the fit, is $(3.09 \pm 0.03)\,\%/\mathrm{mm}$, which is approximately half of the value predicted by numerical simulations.

The same procedure was repeated for the Ka-band detection scheme, but with a direct connection between the ChDR radiator and the WR28 waveguide, where Fig. 5.18 shows an example plot of the signals observed on the oscilloscope for the left and right read-out arms of the BPM when looking downstream. For the same beam parameters, the signal level is approximately 2.8 times higher than the signal level measured when using the horn antennas since less radiation is lost to the surroundings (Fig. 5.15). It can also be seen that the intensity of the reflections following the initial ChDR peak at $1.1\,\mathrm{ns}$ is lower when the waveguides

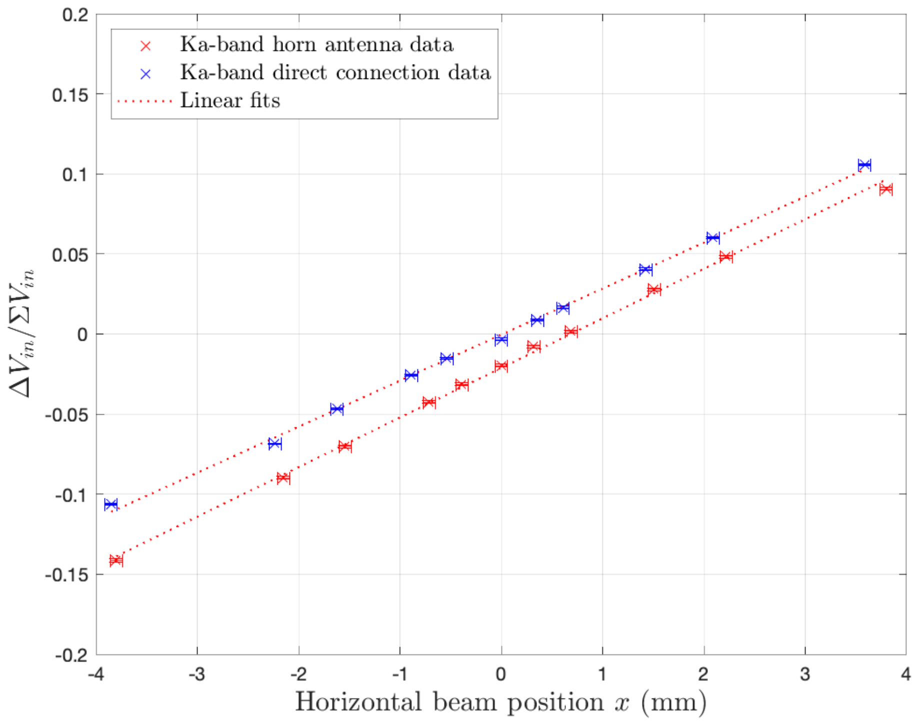

Figure 5.17: Plot of the averaged difference-over-sum of the peak input voltage into the detector versus the horizontal beam position x given by BTV 730. In red for the horn-antenna setup and in blue for the setup with direct waveguide connection. The red dotted line represents the linear fits $\Delta V_{in}/\Sigma V_{in} = b \cdot x + a$ for the two set-ups, where $b = (0.0309 \pm 0.0003)\ /\mathrm{mm}$ and $a = (-0.0212 \pm 0.0006)$ for the horn antenna set-up. $b = (0.0288 \pm 0.0003)\ /\mathrm{mm}$ and $a = (-0.0004 \pm 0.0006)$ for the direct WG connection set-up.

are connected directly to the ChDR radiators compared to when horn antennas are used. The peak in the waveform occurring at $\sim 165\,\mathrm{ps}$ after the initial ChDR peak exists in both set-ups. Therefore, this artefact is not a result of the environment. However, the exact cause of this reflection remains unidentified. What is known is that the time between the initial ChDR peak and the subsequent peak does not correspond to the round-trip time of radiation in the alumina waveguide ($1.8\,\mathrm{ns}$) or in the WR28 attenuator piece which is $70\,\mathrm{mm}$ long, equating to a round-trip time of $\sim 0.47\,\mathrm{ns}$. Since only the peak of the signal is of interest for the purpose

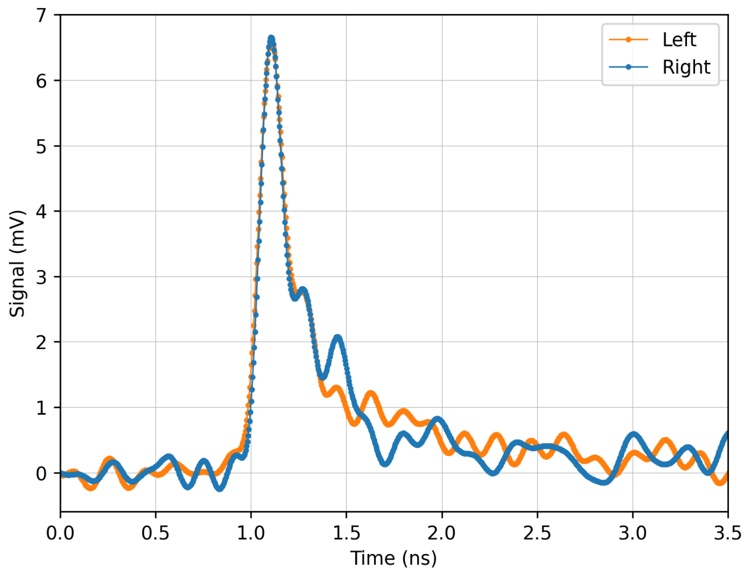

Figure 5.18: Plot of the measured oscilloscope signals (single shot) of the left and right ChDR BPM radiators versus time, for the direct waveguide connection and Ka-band detection.

of the beam position measurement, the difference-over-sum values were again calculated and averaged, and are shown as a function of horizontal beam position measured by BTV 730 in Fig. 5.17 (in blue). The measured sensitivity is (2.88 ± 0.03) %/mm. For this direct connection setup, the offset is smaller compared to when the horn antennas were used. This could be due to differences in alignment of the horn antennas resulting in different alumina-horn distances, which would result in an "electrical" offset wrt. the geometric centre. This is one of the main difficulties and disadvantages of this set-up in comparison to the direct waveguide connection.

The signal detection chain for the V-band is similar to the processing chain shown in Fig. 5.11a for the Ka-band, where the waveguide components and detector were replaced with those operating in the V-band $(50 - 75$ GHz$)$ and the fixed attenuator was removed. The detector used was a Millitech Inc. model DXP-15, which has a WR15 rectangular-waveguide input and a coaxial output. For a bunch with $1\,\mathrm{ps}$ RMS bunch length and $30\,\mathrm{pC}$ bunch charge, the horizontal beam position was scanned from $-5.5\,\mathrm{mm}$ to $5.6\,\mathrm{mm}$, scaled to the location of the ChDR BPM. The averaged waveforms of 100 consecutive beam shots recorded for each beam position setting are shown in Fig. 5.19. The dependence of the square-root of the average peak signal vs. each horizontal beam position setting is plotted in Fig. 5.20 where the error in $\sqrt{V_{out}}$ is propagated from the error of the average peak signal which is taken as the standard error. The red dotted line represents a fit of the data which follows

$$\sqrt{V_{out}} = a \cdot \exp(-b \cdot x), \tag{5.2}$$

where $\sqrt{V_{out}}$ is the square-root of the peak output voltage of the diode detector, x is the horizontal beam position, and a and b are the fit parameters. The difference of the fit of the experimental results compared to simulations is the miss-

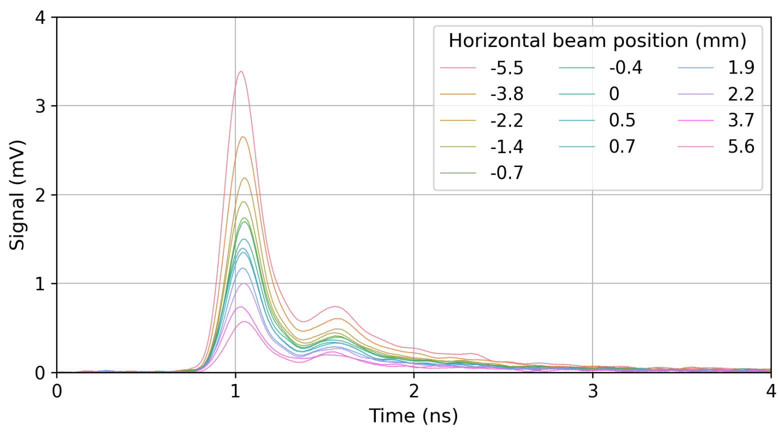

Figure 5.19: Plot of the averaged oscilloscope signals of the ChDR BPM versus time at different horizontal beam position settings. The nominal frequency range of this V-band detection system is $50 - 75$ GHz.

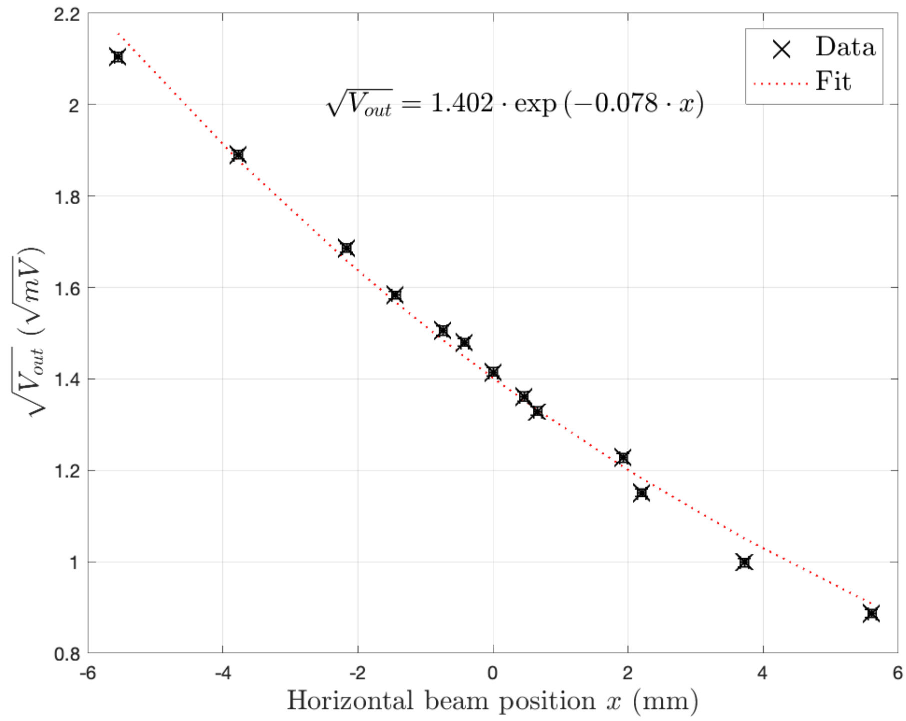

Figure 5.20: Plot of the square-root of the average signal peak at each horizontal beam position for detection setting in the V-band ($50 - 75$ GHz). The exponential fit is represented by the red dotted line.

ing constant B which is present in Eq. 4.2. This is because, in the experiment, when the beam is scanned to the extremities of the beam-pipe, the signal measured from the furthest radiator hits the noise level. For detection in the V-band, $a_V = 1.402\ (\mathrm{mV})^{0.5}$ and $b_V = 0.078\ (\mathrm{mm})^{-1}$. This exponential behaviour of the detected voltage is in agreement with the numerical simulations. A vertical beam position scan was also performed with this set-up and is presented in Fig. 5.21. It can be seen that there are no significant changes to the signal levels from the ChDR alumina radiator in the horizontal plane as the beam is scanned vertically, which is as expected.

Finally, a horizontal beam position scan was performed using a W-band horn antenna connected to an appropriate Schottky diode detector with a WR10 rectangular-waveguide input and coaxial output. The bunch parameters were $1\,\mathrm{ps}$ RMS bunch length and $60\,\mathrm{pC}$ bunch charge. The dependence of the square-root of the average peak signal value at each beam position setting is shown in Fig. 5.22, where again the error in $\sqrt{V_{out}}$ is propagated from the error in the average peak signal which is taken as the standard error. Again an exponential fit is repre-

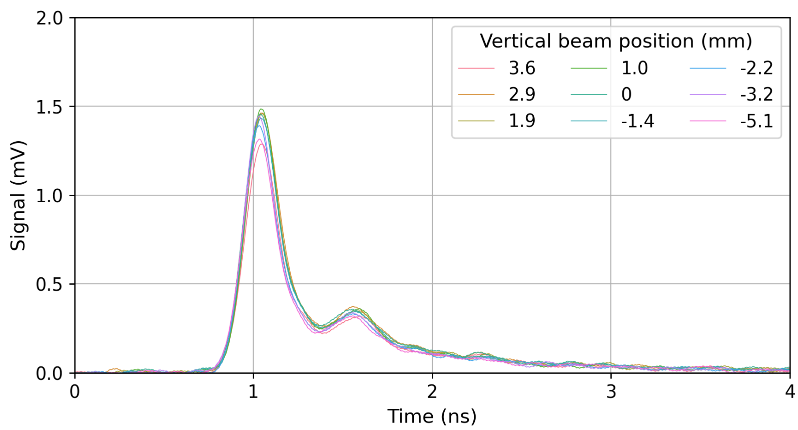

Figure 5.21: Plot of the measured signals of the horizontal ChDR BPM versus time at different vertical beam position settings. The detection system operates in the V-band with the nominal frequency range $50 - 75$ GHz.

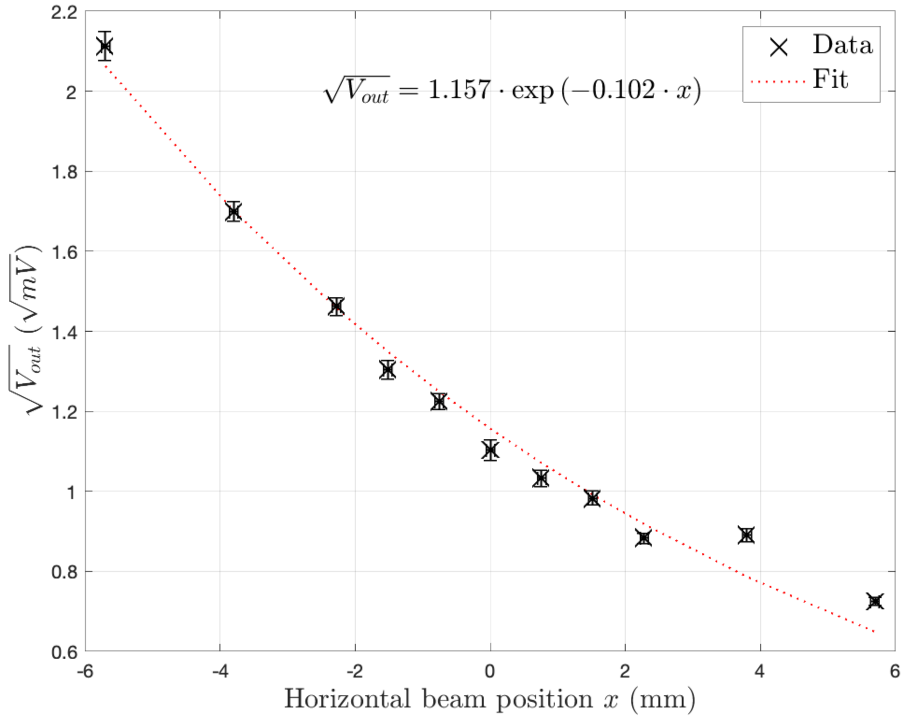

Figure 5.22: Plot of the square-root of the average signal peak at each horizontal beam position setting for detection in the W-band ($75 - 110$ GHz). The exponential fit is represented by the red dotted line.

sented by the red dotted line. The fit parameters with detection in the W-band are $a_W = 1.157\ (\mathrm{mV})^{0.5}$ and $b_W = 0.102\ (\mathrm{mm})^{-1}$.

Since only one of the two ChDR alumina radiators could be equipped with the V and W-band detection system, the BPM sensitivity was extrapolated by assuming a symmetric response in the opposite radiator. The difference-over-sum was calculated given this assumption and is compared in Fig. 5.23 where the red dotted lines represent linear fits of the curves in the range $\pm 2.5\,\mathrm{mm}$ of the centre of the device. The estimated sensitivities are $7.7\%/\mathrm{mm}$ for detection in the V-band and $10.0\%/\mathrm{mm}$ for detection in the W-band. Therefore, as the detection frequency band increases, the sensitivity increases, which is a surprising result as

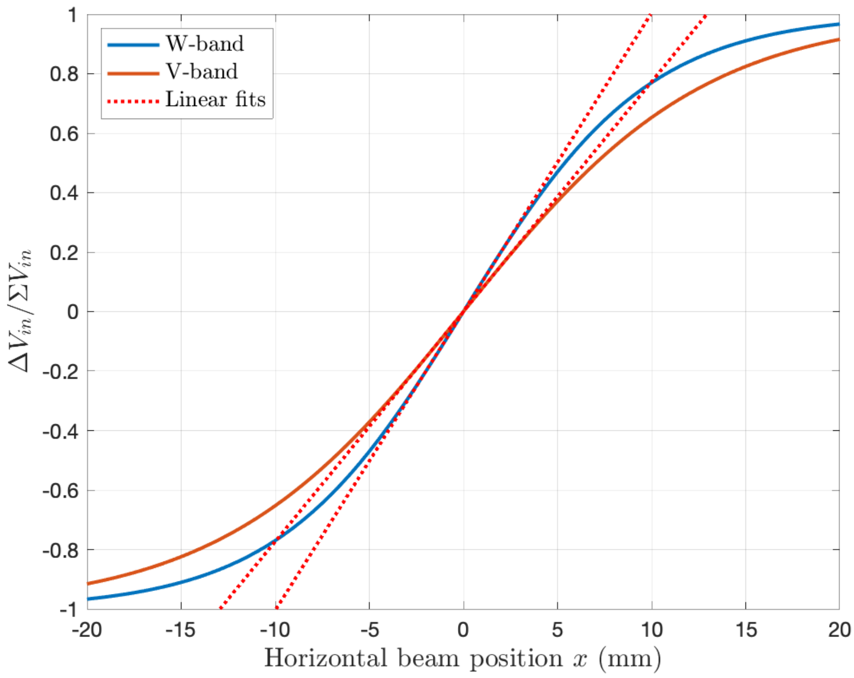

Figure 5.23: Plot of the difference-over-sum position response for the V-band and W-band detection frequencies using the fits for the data in Figures 5.22 and 5.20 respectively, and assuming a symmetric response in the opposite radiator. The linear fits are shown by the red dotted lines performed in a range of $\pm 2.5\,\mathrm{mm}$ where the gradient of the line gives the estimated position sensitivity which is $0.077\,/\mathrm{mm}$ and $0.100\,/\mathrm{mm}$ for the V- and W-band respectively.

this is not in agreement with the numerical simulations where the sensitivity is independent of the detection frequency. Although the discrepancy between the numerical analysis and beam measurements is not fully understood, a previous measurement campaign which aimed at verifying the theoretical model with beam studies at CLEAR showed that the sensitivity increased with detection frequency for a 15 mm diameter, cylindrical PTFE radiator which was measured using Ka-band waveguides and band-pass filters at $30\,\mathrm{GHz}$ and $36\,\mathrm{GHz}$ [76]. Further studies are required to verify the dependence of the sensitivity of the ChDR BPM on the detection frequency and the discrepancy with the numerical simulations.

5.4 Lessons learned

As demonstrated with the successful installation of three ChDR BPMs, two in the AWAKE beam-line and one at CLEAR, the ChDR BPM technology is suitable for in-vacuum integration into an accelerator.

The preliminary tests at AWAKE showed that the ChDR BPM is a possible solution to the problem of measuring the electron bunches (with a typical bunch length of $4\,\mathrm{ps}$ or $1.2\,\mathrm{mm}$ and a bunch charge of a few hundred pC) in the presence of more-intense ($16-48$ nC), but longer ($6-8$ cm), proton bunches from the SPS. This was demonstrated with a narrow-band detection scheme using Ka-band waveguide components at AWAKE where no signal was detected for proton bunches with a bunch charge of $16\,\mathrm{nC}$. However, residual proton signal was observed with a proton bunch charge of $48\,\mathrm{nC}$ with large shot-to-shot variations. This hints that the proton spectrum extends beyond the detection frequency of $30\,\mathrm{GHz}$. Therefore, to better understand the observed signals, it requires an independent system to measure the proton shot-by-shot bunch spectrum. At present, no such system exists at AWAKE.

The beam studies at CLEAR involved measuring the ChDR from the radiators with Schottky diode detectors in three different frequency ranges. These were the Ka-band ($26.5-40$ GHz), V-band ($50-75$ GHz) and W-band ($75-110$ GHz). For the Ka-band detection, the two different read-out set-ups were studied i.e. to couple the ChDR from the exit of the symmetrically arranged horizontal radiators to the detectors. The first was via two horn antennas, one for each radiator. The second set-up involved using a direct waveguide connection between each of the radiators to their respective detectors. For the V-band and W-band detection frequency ranges, only horn antennas were used. For these two ranges, only one of the two radiators was measured due to a limited availability of components.

A bunch charge scan was performed for each set-up. This showed that electron bunches with $1\ \mathrm{ps}$ RMS bunch length and as little as $30\ \mathrm{pC}$ bunch charge could still be detected with the ChDR BPM system. The bunch charge scans also allowed the square-law region of the diode detectors to be identified. In this region the square-root of the output voltage of the detectors $\sqrt{V_{out}}$ is proportional to the bunch charge. For the following beam position scans, the measured signal level was maintained in this regime.

The beam position scans for the Ka-band detection showed a linear difference-over-sum response to the horizontal beam position for the range of approximately $\pm 3.75\ \mathrm{mm}$ from the device centre. The measured position sensitivity for the horn antenna set-up was $(3.09 \pm 0.03)\ \%/\mathrm{mm}$ and for the direct waveguide connection set-up was $(2.88 \pm 0.03)\ \%/\mathrm{mm}$. Some limitations of these set-ups are the use of fixed attenuators instead of remote-controlled variable WG attenuators and, in the case of the horn antennas, the difficulty to perfectly align the antennas symmetrically with respect to the exit face of the radiators. The latter resulted in an "electrical" offset wrt. the geometric centre of the device. For future system development, the direct waveguide connection is a better set-up to reduce these asymmetries arising from the misalignment of the horn antennas. It was also seen that the detected signal was cleaner in the case of the direct waveguide connection. For future work, dedicated control measurements could be acquired without the particle beam and the noise could also be estimated from the oscilloscope shots.

For signal detection in the V-band and W-band, the horizontal beam position was scanned in the range of approximately $\pm 5.5\ \mathrm{mm}$ from the device centre. The dependence of $\sqrt{V_{out}}$ on the horizontal beam position follows an exponential fit as expected from numerical simulations. For these two detection frequency bands, it was not possible to measure the position sensitivity directly. However, by assuming that the position response is symmetric for the opposite radiator, the difference-over-sum as a function of the horizontal beam position was extrapolated. The estimated position sensitivity, equal to the gradient of the linear region of the difference-over-sum vs. horizontal beam position, was $7.7\,\%/\mathrm{mm}$ and $10.0\,\%/\mathrm{mm}$ for detection in the V- and W-band respectively. Although the trend shows an increase in sensitivity with increasing detection frequency from the Ka- to the W-band, the values obtained for the V- and W-band were estimated from a single radiator. To verify these results, a symmetric system should be implemented and further tested.

When comparing the measured ChDR BPM response to the numerical simulations, several interesting points arise. First, although the measured signal levels cannot be compared directly to what CST Studio predicts, due to the use of the Schottky diode detector to measure the ChDR which rectifies, and therefore alters the ChDR signal substantially, an exponential response of $\sqrt{V_{out}}$ to the horizontal beam position was observed, as predicted by CST. Secondly, when using the Ka-band detection, and measuring both radiators simultaneously with identical detection chain configurations for each radiator, the difference-over-sum shows a linear response for the horizontal beam position scan in the range of approximately $\pm 3.75\,\mathrm{mm}$ from the device centre. This is also in agreement with the CST simulations. However, the position sensitivity measured using the Ka-band setups is approximately two times smaller than the value predicted by CST, being $6\,\%/\mathrm{mm}$. Furthermore, this position sensitivity calculated by CST is independent of the read-out frequency range, which also does not match with the beam measurements. The beam studies instead show an increase of the position sensitivity with increasing detection frequency, which has also been observed in a separate R&D project with a different sized cylindrical radiator made of PTFE and similar signal processing chains. The reason for this discrepancy between beam measurements and simulations is not fully understood, but one contributing factor might be the frequency dependence of the relative permittivity of the dielectric which is not included in the numerical analysis. For the signal transmission, the studies performed with the slab-line presented in Section 4.2 under controlled laboratory conditions showed a good agreement between the numerical simulations and measurements. Hence, there are additional, uncontrolled physical factors present in the beam study set-ups, either related to the beam itself or in the detection system, which are not fully understood, investigated and incorporated into the numerical model. Therefore, it would be beneficial to test the ChDR BPM with a different detection system in order to understand if the frequency dependence of the position sensitivity is beam or detection-system related.

6 Conclusions and future work

This thesis detailed the work that was performed on the development of a BPM based on ChDR for use at the AWAKE experiment at CERN. The design of the ChDR BPM aimed at addressing the problem of measuring a shorter, less-intense electron bunch in the presence of a longer, more-intense proton bunch. The ChDR BPM design was supported by numerical simulations, and verified with RF measurements in the laboratory. It was also tested under a variety of beam conditions at both the AWAKE experiment and the CLEAR test facility.

From the PCA theory applied to a single and double triangular prism target, the angular distribution of the PR was calculated. It demonstrated that ChDR is generated only by the face of the dielectric that is parallel to the direction of beam travel. The generation of ChDR does not require the beam to pass through the material but only in close proximity. The radiation produced is a function of various beam parameters, including the beam position. Therefore, this technology is particularly useful for non-invasive beam instrumentation applications such as a BPM based on ChDR.

The PCA theory can be used to better understand the dependence of the ChDR generated by simple target geometries on various geometric parameters of the target and the particle beam parameters. However, using the analytical formalism can be very challenging and time-consuming, and might be impossible for complex target geometries with finite size in all three dimensions. Therefore, the potential of numerical tools, such as CST Studio, to model such geometries and the ChDR generated was investigated in detail.

First, single and double triangular prism targets were modelled in CST for comparison to theory. Although there were discrepancies between simulation and theory on the amount of DR generated from the edges, which is partly due to the finite size of the target in the x direction in the simulation compared to being infinitely long in the PCA theory, the angle and shape of the spectrum of the emitted ChDR using the Wakefield solver agreed very well with theory. A cylindrical target was then computed, and the angle and shape of the ChDR peak remained similar to that of the single and double triangular prism targets provided that all targets had a similar surface area exposed to the beam field. For ease of manufacturing, a cylindrical target was chosen for the design of a ChDR BPM for application at AWAKE.

Numerical simulations were then performed to better understand the propagation of PR inside the dielectric radiators and to aid the design of the ChDR BPM. It was found that, in order to produce a cleaner development of the PR inside the radiator, a shorter radiator length is preferred. The radiator acts as a circular waveguide with high-pass filter characteristic, where the diameter and dielectric permittivity of the material determines the cut-off frequency of the wave propagation. However, going to smaller diameters reduces the radiation output power and the material is more at risk of damage during the manufacturing, metalisation and brazing processes. As a compromise between these factors, a $6\,\mathrm{mm}$ diameter Al_2O_3 ceramic (alumina) radiator was chosen.

The final design was then simulated with varying beam positions to obtain the expected signal output level, the charge normalised position signals and the position sensitivity, which was estimated to be $6\,\%/\mathrm{mm}$. Since the preferred operating frequency of the BPM was $30\,\mathrm{GHz}$, a circuit analysis at $30\,\mathrm{GHz}$ central frequency was performed using the Qucs software with band-pass filters of $300\,\mathrm{MHz}$ and $1\,\mathrm{GHz}$ bandwidth. Following this, an estimation of the theoretically achievable BPM resolution was computed to be $9\,\mu\mathrm{m}$ and $6\,\mu\mathrm{m}$ for $300\,\mathrm{MHz}$ and $1\,\mathrm{GHz}$ BW filters respectively. The signal level and resolution could be improved by adding a dielectric-loaded circular-waveguide to WR28 rectangular-waveguide transition made from fused quartz, where the length was optimised to maximise the power transmission at $30\,\mathrm{GHz}$. Whilst the WR28 waveguide reflects power below $21\,\mathrm{GHz}$, an alternative way of coupling the signal out of the exit of the ChDR alumina radiator was studied, using a dielectric-loaded circular waveguide-to-coaxial adapter designed using CST. This allows the wave transmission from and above the TE11-mode cut-off frequency of the alumina radiator, which is $9.3\,\mathrm{GHz}$.

A laboratory set-up was designed and manufactured for RF measurements and full characterisation of the ChDR radiators in the frequency range of interest, i.e. between $\sim 9\,\mathrm{GHz}$ and $40\,\mathrm{GHz}$. The set-up involved the TEM signal excitation using a so-called slab-line, composed of two ground planes (slabs) and a central conducting tube, via a VNA. The measured spectrum and time-domain signals agreed very well with simulations, showing a cut-off frequency of $21\,\mathrm{GHz}$ when a commercial HP R281A waveguide-to-coaxial adapter was used at the exit of the ChDR alumina rod and $9.3\,\mathrm{GHz}$ when the dielectric-loaded circular waveguide-to-coaxial adapter was used. This laboratory exercise verified the numerical simulations and provided a useful tool for characterising radiators in these high frequency ranges.

Three ChDR BPMs were manufactured. Two of them, which were each equipped with four ChDR alumina radiators, were installed at AWAKE, and the third ChDR BPM, with only two ChDR alumina radiators making up the horizontal plane, was installed at CLEAR. Parasitic measurements were taken at AWAKE, but only in the horizontal plane of one of the two installed ChDR BPMs due to the limited availability of RF components. The radiation was measured using a Ka-Band signal detection chain for a variety of beam configurations: protons only, electrons only, and both simultaneously. It was found that the ChDR BPM is insensitive to proton signals at $16\,\mathrm{nC}$ bunch charge. However, residual proton signals are still sometimes detected if the bunch charge is $48\,\mathrm{nC}$. This indicated that the proton spectrum extends to frequencies higher than the preferred ChDR BPM detection frequency of $30\,\mathrm{GHz}$. Therefore, the series of dedicated electron beam tests at CLEAR also included signal detection setups at higher frequency bands.

The tests at CLEAR showed that for a symmetric set-up in the horizontal plane, with Ka-Band signal detection scheme, the difference-over-sum is linear between approximately $\pm 4\,\mathrm{mm}$, which is what was expected from numerical simulations. The measured sensitivity was $(3.09 \pm 0.03)\,\%/\mathrm{mm}$ when using Ka-Band horn antennas and $(2.88 \pm 0.03)\,\%/\mathrm{mm}$ when the exit of the ChDR radiator was connected directly to the WR28 waveguide. Two other frequency bands were tested on only one of the two ChDR alumina radiators. These frequency ranges were the V-band ($50 - 75$ GHz) and W-Band ($75 - 110$ GHz). By scanning the horizontal beam position, the relationship between the square-root of the peak output signal of the diode detectors and the horizontal beam position was obtained. It followed an exponential decay function which is in agreement with the numerical simulations. By assuming a symmetric system, the position sensitivity was estimated to be $7.7\,\%/\mathrm{mm}$ for detection in the V-Band and $10.0\,\%/\mathrm{mm}$ for detection in the W-Band, showing increasing sensitivity with increasing detection frequency.

The work outlined in the experimental section of this thesis has shed light on various aspects of the ChDR BPM, including its response to bunch charge variations and horizontal beam position at three different frequency ranges. However, the ChDR BPM still requires further systematic beam studies before it can be fully-operational. These future studies may include the testing of the reproducibility of the various detection chains upon dismounting and mounting, and performing beam measurements with a symmetric set-up in the V-Band and W-Band. Whilst these studies can be done at CLEAR, it is important to test the same detection chains at AWAKE to verify that they produce the same results. It is also important to test the higher frequency detection bands with proton bunches to see if any signal is measured from high-charge protons at such high detection frequencies. This will provide valuable information as to what detection frequency should be considered as optimal for the ChDR BPMs at AWAKE. Finally, a direct measurement of the resolution and accuracy with beam would be required to fully understand the core characteristics of the ChDR BPM.

Evidently, this new type of beam position monitor based on Cherenkov diffraction radiation will not replace traditional broadband, electromagnetic BPM pick-ups, like button-style or stripline BPMs, or narrower-band, resonant cavity BPMs, typically used in particle accelerators for beam orbit monitoring. In contrast to these BPMs, which are usually limited to operate at lower frequencies by the RF feedthroughs, the ChDR BPM radiator utilizes the upper end of the e-bunch spectrum, here $f \gtrsim 10\,\mathrm{GHz}$, depending on the selected dimensions and material properties of the radiator. While resonant cavity BPMs may also be attractive for the detection of single bunches at high frequencies, they require $f_{TM110bpm} < f_{TE11pipe}$, and therefore a beam pipe of rather small aperture to keep the TM110 dipole mode trapped in the BPM resonator, which unfortunately is not the case for the $60\,\mathrm{mm}$ diameter vacuum chamber of AWAKE.

This new method, required new technologies and techniques, as well as many practical and also some theoretical details, some of which still need to be addressed. As discussed in Chapter 4, the radiation generated at the dielectric surface area is always a mix of Cherenkov diffraction radiation, plus some diffraction radiation generated by the edge of the radiator. This unwanted edge radiation mixes with the primary Cherenkov diffraction radiation, resulting in a detection signal waveform that is more difficult to analyze. In practice, the signal analysis turned out to be even more challenging as it was not possible to directly analyze the signal of the ChDR radiation and its frequency content, but only that of the detected signal i.e. the rectified signal through several signal processing components. Moreover, several ChDR radiator design options, e.g. the radiator shape, dimensions and material, were limited due to practical considerations, such as the compatibility with the existing BPM housing.

In essence, the ChDR BPM discussed in this work gave promising results as a BPM pick-up operating at very high frequencies, but it requires more theoretical studies and optimization, as well as practical considerations, in particular with respect to the read-out signal processing, before it can be installed and operated as a reliable beam instrument. Whilst the simulated position sensitivity is similar to that of an electromagnetic broadband BPM pick-up operating according to the image current model, surprisingly the measured position sensitivity of the ChDR BPM increases with the read-out frequency, which is a plus for its application as a high frequency BPM. Besides its operation as a BPM, a direct processing of the high frequency signal content of the ChDR radiation may also be of interest for other beam instrumentation applications, such as time-of-flight or similar bunch arrival time diagnostics.

Bibliography

[1] B. R. Martin and G. Shaw. *Particle physics*. Wiley, 2017.

[2] Peter W. Higgs. "Broken Symmetries and the Masses of Gauge Bosons". *Phys. Rev. Lett.* 13 (1964), pp. 508–509. DOI: 10.1103/PhysRevLett.13.508. URL: https://link.aps.org/doi/10.1103/PhysRevLett.13.508.

[3] Thomas Sven Pettersson and P Lefèvre. *The Large Hadron Collider: conceptual design*. 1995. URL: https://cds.cern.ch/record/291782.

[4] Serguei Chatrchyan et al. "Observation of a New Boson at a Mass of 125 GeV with the CMS Experiment at the LHC". *Phys. Lett. B* 716 (2012), pp. 30–61. DOI: 10.1016/j.physletb.2012.08.021.

[5] Georges Aad et al. "Observation of a new particle in the search for the Standard Model Higgs boson with the ATLAS detector at the LHC". *Phys. Lett. B* 716 (2012), pp. 1–29. DOI: 10.1016/j.physletb.2012.08.020.

[6] Helmut Wiedemann. *Particle accelerator physics*. Springer, 2015.

[7] Jeff Holmes, Stuart Henderson, and Yan Zhang. *Magnetic Fields and Magnet Design Lecture 2 USPAS*. URL: https://uspas.fnal.gov/materials/09VU/Lecture2.pdf.

[8] E. Wilson and B. J. Holzer. "Beam Dynamics". *Particle Physics Reference Library: Volume 3: Accelerators and Colliders*. Ed. by Stephen Myers and

Herwig Schopper. 2020, pp. 15–50. DOI: 10.1007/978-3-030-34245-6_2.

[9] Alexander Wu Chao et al. *Handbook of accelerator physics and engineering; 2nd ed.* Singapore: World Scientific, 2013. DOI: 10.1142/8543. URL: https://cds.cern.ch/record/1490001.

[10] O. Aberle et al. *High-Luminosity Large Hadron Collider (HL-LHC): Technical design report*. Tech. rep. 2020. DOI: 10.23731/CYRM-2020-0010. URL: https://cds.cern.ch/record/2749422.

[11] A. Abada et al. "FCC-hh: The Hadron Collider: Future Circular Collider Conceptual Design Report Volume 3". *Eur. Phys. J. ST* 228.4 (2019), pp. 755–1107. DOI: 10.1140/epjst/e2019-900087-0.

[12] *Tunnelling for physics*. 2022. URL: https://cerncourier.com/a/tunnelling-for-physics/.

[13] Andrei Seryi et al. "Overview of design development of FCC-hh Experimental Interaction Regions". *Proc., 8th International Particle Accelerator Conference (IPAC 2017): Copenhagen, Denmark, May 14-19, 2017* (2017). On behalf of EuroCirCol WP3. DOI: 10.18429/JACoW-IPAC2017-TUPVA040. URL: https://cds.cern.ch/record/2281099.

[14] M Aicheler et al. *A Multi-TeV Linear Collider Based on CLIC Technology: CLIC Conceptual Design Report*. 2012. DOI: 10.5170/CERN-2012-007. URL: https://cds.cern.ch/record/1500095.

[15] M J Boland et al. *Updated baseline for a staged Compact Linear Collider*. 2016. DOI: 10.5170/CERN-2016-004. URL: https://cds.cern.ch/record/2210892.

[16] A. Robson et al. "The Compact Linear e^+e^- Collider (CLIC): Accelerator and Detector". *arXiv:1812.07987 [physics.acc-ph]* (2018). DOI: 10.

48550/ARXIV.1812.07987. URL: https://arxiv.org/abs/1812.07987.

[17] Hiroaki Aihara et al. “The International Linear Collider. A Global Project”. *arXiv:1901.09829 [hep-ex]* (2019). URL: https://doi.org/10.48550/arXiv.1901.09829.

[18] Lyn Evans and Shinichiro Michizono. “The International Linear Collider Machine Staging Report 2017”. *arXiv:1711.00568 [physics.acc-ph]* (2017). DOI: 10.48550/ARXIV.1711.00568. URL: https://arxiv.org/abs/1711.00568.

[19] W. D. Kilpatrick. “Criterion for Vacuum Sparking Designed to Include Both rf and dc”. *Review of Scientific Instruments* 28.10 (1957). DOI: 10.1063/1.1715731. URL: https://www.osti.gov/biblio/4330281.

[20] Compact Linear Collider Project CLIC. *CLIC accelerator schematic diagrams*. 2019. URL: https://cds.cern.ch/record/2655160.

[21] Gerald Aarons et al. “ILC Reference Design Report Volume 1 - Executive Summary”. *arXiv:0712.1950 [physics.acc-ph]* (2007). URL: https://doi.org/10.48550/arXiv.0712.1950.

[22] Arghya Mukherjee. “Wave breaking field of relativistically intense electrostatic waves in electronegative plasma with super-thermal electrons”. *Sci. Rep.* 12.1 (2022), p. 12263.

[23] T. Tajima and J. M. Dawson. “Laser Electron Accelerator”. *Phys. Rev. Lett.* 43 (1979), pp. 267–270. DOI: 10.1103/PhysRevLett.43.267. URL: https://link.aps.org/doi/10.1103/PhysRevLett.43.267.

[24] E. Esarey et al. "Overview of plasma-based accelerator concepts". *IEEE Transactions on Plasma Science* 24.2 (1996), pp. 252–288. DOI: 10.1109/27.509991.

[25] E. Esarey, C. B. Schroeder, and W. P. Leemans. "Physics of laser-driven plasma-based electron accelerators". *Rev. Mod. Phys.* 81 (2009), pp. 1229–1285. DOI: 10.1103/RevModPhys.81.1229.

[26] V. Malka. "Plasma Wake Accelerators: Introduction and Historical Overview". *arXiv:1705.09584 [physics.acc-ph]* (2016), pp. 1–28. DOI: 10.5170/CERN-2016-001.1. URL: https://cds.cern.ch/record/2203628.

[27] Donna Strickland and Gerard Mourou. "Compression of amplified chirped optical pulses". *Opt. Commun.* 55.6 (1985), pp. 447–449. DOI: 10.1016/0030-4018(85)90151-8.

[28] P. Maine et al. "Generation of ultrahigh peak power pulses by chirped pulse amplification". *IEEE Journal of Quantum Electronics* 24.2 (1988), pp. 398–403. DOI: 10.1109/3.137.

[29] J. Faure et al. "A laser–plasma accelerator producing monoenergetic electron beams". *Nature* 431.7008 (2004), pp. 541–544. DOI: 10.1038/nature02963.

[30] C G.R. Geddes et al. "High quality electron beams from a plasma channel guided laser wakefield accelerator". *Nature* 431.7008 (2004). DOI: 10.1038/nature02900. URL: https://www.osti.gov/biblio/836978.

[31] S. P. Mangles et al. "Monoenergetic beams of relativistic electrons from intense laser–plasma interactions". *Nature* 431.7008 (2004), pp. 535–538. DOI: 10.1038/nature02939.

[32] B. Cros. "Laser-driven Plasma Wakefield: Propagation Effects". *CERN Yellow Rep.* (2016). Ed. by Bernhard Holzer, pp. 207–230. DOI: 10.5170/CERN-2016-001.207.

[33] Brigitte Cros. "Plasma physics: Compact coupling for a two-stage accelerator". *Nature* 530 (2016), pp. 165–166.

[34] S. Steinke et al. "Multistage coupling of independent laser-plasma accelerators". *Nature* 530.7589 (2016), pp. 190–193. DOI: 10.1038/nature16525.

[35] Pisin Chen et al. "Acceleration of Electrons by the Interaction of a Bunched Electron Beam with a Plasma". *Phys. Rev. Lett.* 54 (1985), pp. 693–696. DOI: 10.1103/PhysRevLett.54.693. URL: https://link.aps.org/doi/10.1103/PhysRevLett.54.693.

[36] Ian Blumenfeld et al. "Energy doubling of 42 GeV electrons in a metre-scale plasma wakefield accelerator". *Nature* 445.7129 (2007), pp. 741–744. ISSN: 0028-0836. DOI: 10.1038/nature05538. URL: https://doi.org/10.1038/nature05538.

[37] E. Gschwendtner et al. "Proton Driven Plasma Wakefield Acceleration in AWAKE". *Philos. Trans. R. Soc. Lond. A* 377 (2019), p. 20180418. DOI: 10.1098/rsta.2018.0418. URL: https://cds.cern.ch/record/2654201.

[38] E. Adli et al. "Acceleration of electrons in the plasma wakefield of a proton bunch". *Nature* (2018). DOI: 10.1038/s41586-018-0485-4. URL: http://cds.cern.ch/record/2637262.

[39] Seong-Yeol Kim et al. "Study of the Electron Beam Transfer Line for the AWAKE RUN II Experiment at CERN". *29th Linear Accelerator Conference-LINAC18, Beijing, 16-19 September 2018* (2018), THPO132. DOI: 10.18429/JACoW-LINAC2018-THPO132. URL: https://cds.cern.ch/record/2668354.

[40] E. Gschwendtner et al. “AWAKE, The Advanced Proton Driven Plasma Wakefield Acceleration Experiment at CERN”. *Nuclear Instruments and Methods in Physics Research Section A: Accelerators, Spectrometers, Detectors and Associated Equipment* 829 (2016). 2nd European Advanced Accelerator Concepts Workshop - EAAC 2015, pp. 76–82. DOI: `https://doi.org/10.1016/j.nima.2016.02.026`. URL: `https://www.sciencedirect.com/science/article/pii/S0168900216001881`.

[41] Patric Muggli. “Progress Toward an Experiment at AWAKE”. *2nd North American Particle Accelerator Conference*. 2017, WEPOA02. DOI: `10.18429/JACoW-NAPAC2016-WEPOA02`.

[42] P. Muggli et al. “AWAKE readiness for the study of the seeded self-modulation of a 400 GeV proton bunch”. *Plasma Phys. Control. Fusion* 60.1 (2017). Ed. by Marta Fajardo and Richard Dendy, p. 014046. DOI: `10.1088/1361-6587/aa941c`.

[43] R Losito et al. “The PHIN photoinjector for the CTF3 Drive beam”. *10th European Particle Accelerator Conference: Edinburgh, UK, 26 - 30 Jun 2006*. 2006. URL: `https://cds.cern.ch/record/972359`.

[44] Janet Schmidt et al. “The AWAKE electron primary beam line”. *6th International Particle Accelerator Conference (IPAC 2015): Richmond, VA, USA, 3 - 8 May 2015*. 2015. DOI: `10.18429/JACoW-IPAC2015-WEPWA03`.

[45] K. Pepitone et al. “The electron accelerators for the AWAKE experiment at CERN - Baseline and future developments”. *Nucl. Instrum. Meth. A* 909 (2018), pp. 102–106. DOI: `10.1016/j.nima.2018.02.044`.

[46] E. Adli et al. “Experimental observation of proton bunch modulation in a plasma, at varying plasma densities”. *Phys. Rev. Lett.* 122.5 (2019), p. 054802. DOI: `10.1103/PhysRevLett.122.054802`.

[47] Patric Muggli. “Physics to plan AWAKE Run 2”. *J. Phys. Conf. Ser.* 1596.1 (2020). Ed. by Alessandro Cianchi et al., p. 012008. DOI: 10.1088/1742-6596/1596/1/012008.

[48] Patric Muggli and Allen Christopher Caldwell. “First Physics Results of AWAKE, a Plasma Wakefield Acceleration Experiment at CERN”. *PoS* EPS-HEP2017 (2018), p. 533. DOI: 10.22323/1.314.0533. URL: https://cds.cern.ch/record/2670655.

[49] M. Turner et al. “Experimental observation of plasma wakefield growth driven by the seeded self-modulation of a proton bunch”. *Phys. Rev. Lett.* 122.5 (2019), p. 054801. DOI: 10.1103/PhysRevLett.122.054801.

[50] Stefano Mazzoni et al. “Beam Instrumentation Developments for the Advanced Proton Driven Plasma Wakefield Acceleration Experiment at CERN”. *Proc., 8th International Particle Accelerator Conference (IPAC 2017): Copenhagen, Denmark, May 14-19, 2017*. 2017, MOPAB119. DOI: 10.18429/JACoW-IPAC2017-MOPAB119. URL: https://cds.cern.ch/record/2287342.

[51] Ishkhan Gorgisyan et al. “Commissioning of beam instrumentation at the CERN AWAKE facility after integration of the electron beam line”. *J. Phys. Conf. Ser.* 1067 (2018), p. 072015.

[52] Shengli Liu et al. “Development of the AWAKE Stripline BPM Electronics”. *Springer Proc. Phys.* 212 (2018), pp. 237–242. DOI: 10.1007/978-981-13-1313-4_46. URL: https://cds.cern.ch/record/2650503.

[53] J Shanks et al. “Accelerator design for the Cornell High Energy Synchrotron Source upgrade”. *Phys. Rev. Accel. Beams* 22.2 (2019).

[54] R. Kieffer et al. “Generation of incoherent Cherenkov diffraction radiation in synchrotrons”. *Phys. Rev. Accel. Beams* 23 (2020). DOI: 10.1103/

PhysRevAccelBeams.23.042803. URL: https://link.aps.org/doi/10.1103/PhysRevAccelBeams.23.042803.

[55] R. Kieffer et al. “Direct Observation of Incoherent Cherenkov Diffraction Radiation in the Visible Range”. *Phys. Rev. Lett.* 121 (2018). DOI: 10.1103/PhysRevLett.121.054802. URL: https://link.aps.org/doi/10.1103/PhysRevLett.121.054802.

[56] Daniel Harryman. “Development of a Non-Invasive Transverse Beam Position Monitor using Incoherent Cherenkov Diffraction Radiation”. Doctoral thesis. Royal Holloway, University of London, 2022.

[57] Gerhard Materlik, Trevor Rayment, and David I Stuart. “Diamond Light Source: status and perspectives”. en. *Philos. Trans. A Math. Phys. Eng. Sci.* 373.2036 (2015).

[58] D Gamba et al. “The CLEAR user facility at CERN”. *Nucl. Instrum. Methods Phys. Res., A* 909 (2018). Submitted to Nuclear Instruments and Methods in Physics Research Section A: Accelerators, Spectrometers, Detectors and Associated Equipment. DOI: 10.1016/j.nima.2017.11.080. URL: https://cds.cern.ch/record/2665487.

[59] Eugenio Senes. “Development of a beam position monitor for co-propagating electron and proton beams”. Doctoral thesis presented 08 Dec 2020. University of Oxford, 2020. URL: https://cds.cern.ch/record/2753708.

[60] John David Jackson. *Classical Electrodynamics*. 3rd ed. John Wiley & Sons, 1998.

[61] Manfred Wendt. “BPM Systems: A brief Introduction to Beam Position Monitoring”. *arXiv:2005.14081 [physics.acc-ph]* (2020). URL: https://api.semanticscholar.org/CorpusID:218971711.

[62] *Lorentz Transformations of the Fields*. URL: https://www.feynmanlectures.caltech.edu/II_26.html.

[63] P Forck, P Kowina, and D Liakin. "Beam position monitors". *CAS - CERN Accelerator School: Beam Diagnostics: Dourdan, France 28 May - 6 Jun 2008*. 2008, p. 187. DOI: 10.5170/CERN-2009-005.187. URL: https://cds.cern.ch/record/1213277.

[64] Yves Renier. "Implementation and validation of the linear collider final focus prototype: ATF2 at KEK (Japan)". Doctoral thesis presented 11 Jun 2010. De l'Université Paris XI Orsay, 2010.

[65] Alexander Petrovich Potylitsyn et al. *Diffraction radiation from relativistic particles*. 2011th ed. Springer tracts in modern physics. Berlin, Germany: Springer, 2010.

[66] V. L. Ginzburg and I. M. Frank. "Radiation of a uniformly moving electron due to its transition from one medium into another". *J. Phys. (USSR)* 9 (1945), pp. 353–362.

[67] K. O. Kruchinin and D. V. Karlovets. "Development of the theory of diffraction radiation from surfaces with finite conductivity". *Russian Physics Journal* 55.1 (2012), pp. 9–16. DOI: 10.1007/s11182-012-9770-0.

[68] P. A. Čerenkov. "Visible Radiation Produced by Electrons Moving in a Medium with Velocities Exceeding that of Light". *Phys. Rev.* 52 (1937), pp. 378–379. DOI: 10.1103/PhysRev.52.378. URL: https://link.aps.org/doi/10.1103/PhysRev.52.378.

[69] M V Shevelev and A S Konkov. "Peculiarities of the generation of Vavilov-Cherenkov radiation induced by a charged particle moving past a dielectric target". *J. Exp. Theor. Phys.* 118.4 (2014), pp. 501–511.

[70] Thibaut Lefèvre et al. "Non-invasive beam diagnostics with Cherenkov Diffraction Radiation". *9th International Particle Accelerator Conference*

(IPAC 2018): Vancouver, BC, Canada, April 29 - May 4, 2018. 2018. DOI: 10.18429/JACoW-IPAC2018-WEPAF074.

[71] Thibaut Lefèvre et al. "Cherenkov Diffraction Radiation as a tool for beam diagnostics". *8th International Beam Instrumentation Conference (IBIC 2019), Malmo, Sweden, 8 - 12 Sep 2019* (2019), THAO01. DOI: 10.18429/JACoW-IBIC2019-THAO01. URL: https://cds.cern.ch/record/2750968.

[72] Michele Bergamaschi et al. "Recent results using incoherent Cherenkov Diffraction Radiation for non-invasive beam diagnostics". *Proceedings, 10th International Particle Accelerator Conference (IPAC2019): Melbourne, Australia, 19-24 May, 2019* (2019), WEPGW077. DOI: 10.18429/JACoW-IPAC2019-WEPGW077. URL: http://cds.cern.ch/record/2693723.

[73] I. M. Frank and I. E. Tamm. "Coherent visible radiation of fast electrons passing through matter". *Compt. Rend. Acad. Sci. URSS* 14.3 (1937), pp. 109–114. DOI: 10.3367/UFNr.0093.196710o.0388.

[74] Elian Bouquerel. *Water Cherenkov detector*. 2018. URL: https://essnusb.eu/glossary/water-cherenkov-detector/.

[75] L Bobb et al. "Feasibility of diffraction radiation for noninvasive beam diagnostics as characterized in a storage ring". *Phys. Rev. Accel. Beams* 21.3 (2018), p. 032801. DOI: 10.1103/PhysRevAccelBeams.21.032801. URL: https://cds.cern.ch/record/2643947.

[76] Kacper Lasocha. "Non-Invasive Beam Diagnostics with Schottky Signals and Cherenkov Diffraction Radiation". Doctoral thesis presented 12 Dec 2022. Jagiellonian University, 2022. URL: https://cds.cern.ch/record/2846538.

[77] A P Potylitsyn and S Yu Gogolev. "Radiation losses of the relativistic charge moving near a dielectric radiator". *Russ. Phys. J.* 62.12 (2020), pp. 2187–2193.

[78] R Kieffer et al. "Optical diffraction radiation for position monitoring of charged particle beams". *Nucl. Instrum. Methods Phys. Res. B* 402 (2017), pp. 88–91.

[79] D. V. Karlovets and A. P. Potylitsyn. "Diffraction radiation from a finite-conductivity screen". *JETP Letters* 90.5 (2009), pp. 326–331. DOI: 10.1134/s0021364009170032. URL: https://doi.org/10.1134%2Fs0021364009170032.

[80] M. Shevelev, A. Konkov, and A. Aryshev. "Soft-x-ray Cherenkov radiation generated by a charged particle moving near a finite-size screen". *Phys. Rev. A* 92 (2015), p. 053851. DOI: 10.1103/PhysRevA.92.053851. URL: https://link.aps.org/doi/10.1103/PhysRevA.92.053851.

[81] Wolfram Research Inc. *Mathematica, Version 13.2*. Champaign, IL, 2022. URL: https://www.wolfram.com/mathematica.

[82] *CST Studio Suite 3D EM Simulation and Analysis Software*. URL: https://www.3ds.com/products-services/simulia/products/cst-studio-suite/?utm_source=cst.com&utm_medium=301&utm_campaign=cst.

[83] Richard G Carter. *The Cambridge RF and microwave engineering series: Microwave and RF vacuum electronic power sources*. The Cambridge RF and microwave engineering series. Cambridge, England: Cambridge University Press, 2018.

[84] Stefan Jahn. *Qucs project: Quite universal circuit simulator*. URL: https://qucs.sourceforge.net/.

[85] Nathan Marcuvitz. *Waveguide Handbook*. Electromagnetics and Radar. Institution of Engineering and Technology, 1986.

[86] Ruey-Beei Wu. "A wideband waveguide transition design with modified dielectric transformer using edge-based tetrahedral finite-element analysis". *IEEE Transactions on Microwave Theory and Techniques* 44.7 (1996), pp. 1024–1031. DOI: 10.1109/22.508634.

[87] R.M. Chisholm. "The Characteristic Impedance of Trough and Slab Lines". *IRE Transactions on Microwave Theory and Techniques* 4.3 (1956), pp. 166–172. DOI: 10.1109/TMTT.1956.1125045.

[88] C. Capelli N. Chritin. URL: https://edms.cern.ch/ui/#!master/navigator/document?D:101122354:101122354:subDocs.

[89] *SMA Female flange mount connector, 4 hole (solder pot)*. URL: https://svmicrowave.com/sma-female-flange-mount-connector-4-hole-solder-pot-2.

[90] N. Chritin. URL: https://edms.cern.ch/document/2631388/1.

[91] Kyrre Sjobak et al. "Status of the CLEAR electron beam user facility at CERN". *Proceedings, 10th International Particle Accelerator Conference (IPAC2019): Melbourne, Australia, 19-24 May, 2019* (2019), MOPTS054. DOI: 10.18429/JACoW-IPAC2019-MOPTS054. URL: https://cds.cern.ch/record/2695092.

[92] *CLEAR layout*. URL: https://gitlab.cern.ch/CLEAR/clearlayout.

[93] *Square Law and Linear Detection*. URL: https://g3ynh.info/circuits/diode_data/AN986.pdf.